Investigation of Heat Transfer using Planar Laser Induced Fluorescence and Design of Cold Plates for Cooling of High Heat Flux Electronics

MSc thesis, spring 2012
Group TEPE4-1000
Board of Studies of Energy

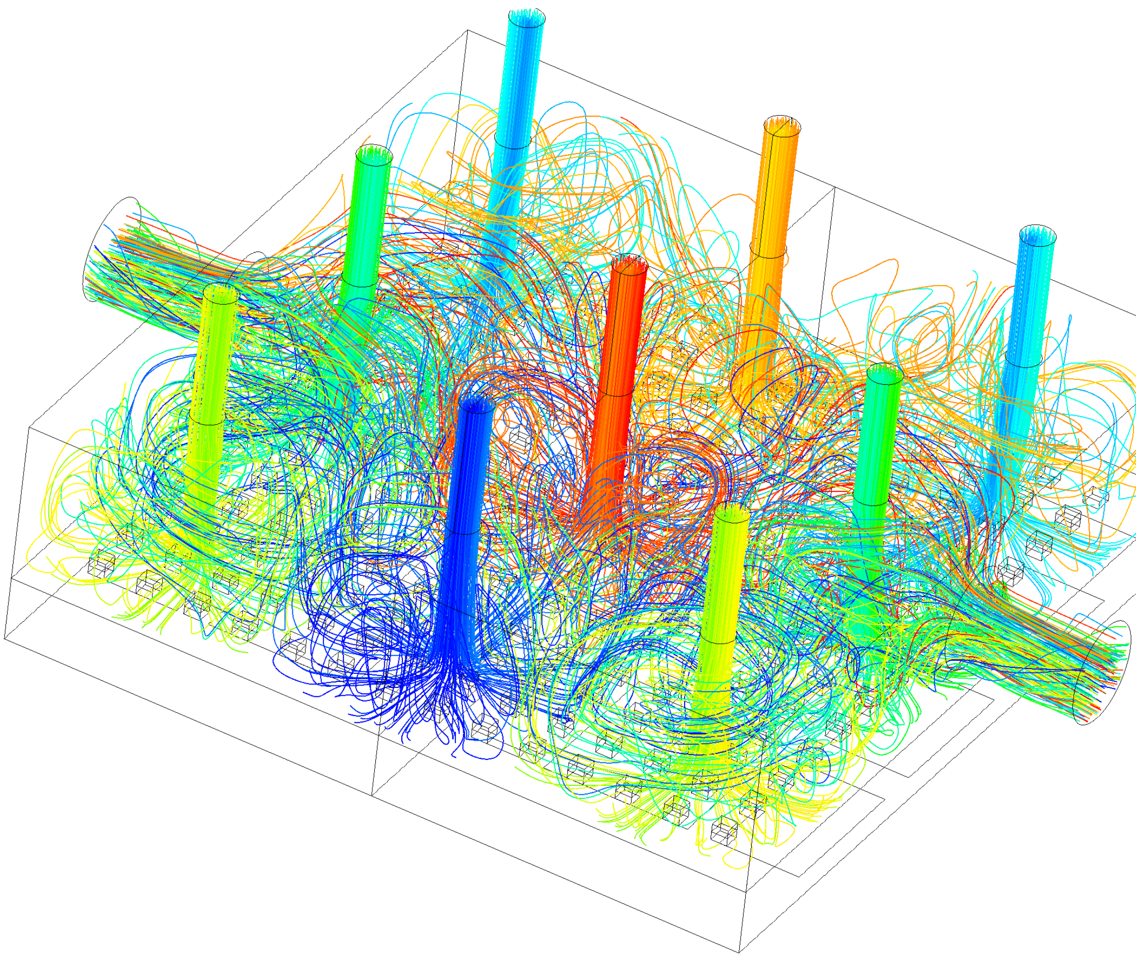

Morten Ryge Bøgild
Jonas Lundsted Poulsen
Emil Zacho Rath

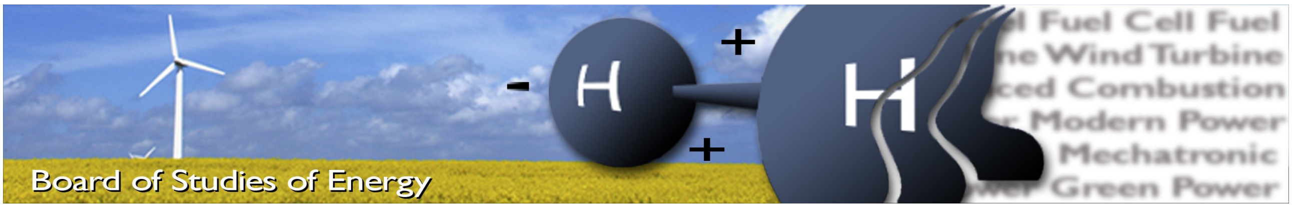

Title:	Investigation of Heat Transfer using Planar Laser Induced Fluorescence and Design of Cold Plates for Cooling of High Heat Flux Electronics
Semester:	10th semester Thermal Energy and Process Engineering
Semester theme:	MSc thesis
Project period:	01.02.12 to 31.05.12
ECTS:	30
Supervisor:	Associate Professor Henrik Sørensen
Project group:	TEPE4-1000

Morten Ryge Bøgild

Jonas Lundsted Poulsen

Emil Zacho Rath

SYNOPSIS:

In this thesis analytical, numerical and experimental studies of high heat flux cooling is conducted. The aim of the project is twofold: 1) To design a high heat flux cooling application in cooperation with Danfoss, and 2) to experimentally investigate mini scale heat transfer in mini channels by using planar laser induced fluorescence (PLIF).

In part I especially CFD simulations are used to evaluate the cooling performance of different designs to cool an IGBT power module. The aim is to have low junction temperature and uniform temperature distribution with low pumping power requirements. Two designs are selected to be manufactured: A multijet design and a hybrid design with both jet impingement and mini channels.

The designs are evaluated against the commercial cooling application "Shower Power", where the convective heat transfer coefficient is shown to be higher than for Shower Power at a higher range of pumping powers.

In part II it is shown that it is possible to resolve the temperature gradient along a mini channel sufficiently accurate by using PLIF. It is also shown that the applicability of PLIF over the whole geometry is not found satisfactory, as optical disturbances are found.

Copies:	5
Pages, total:	141
Appendix:	6
Supplements:	CD

By signing this document, each member of the group confirms that all participated in the project work and thereby all members are collectively liable for the content of the report. Furthermore, all group members confirm that the report does not include plagiarism.

Preface

This report is documentation for the master thesis within Thermal Energy and Process Engineering at the Board of Studies of Energy at Aalborg University. The project documentation consists of two parts. Part I is made in in collaboration with Danfoss Power Electronics A/S, and is titled *"Investigation and Design of Cold Plates for High Heat Flux Electronics"*. The group would like to thank Klaus Olesen (specialist in thermal design, Danfoss Power Electronics A/S) and Jørgen Holst (specialist in thermal systems, Danfoss Power Electronics A/S) for being good sparring partners and providing IGBT power modules.

Part II consists of an article titled *"Investigation of Heat Transfer in Mini Channels using Planar Laser Induced Fluorescence"*. This article is prepared for the 6th European Thermal Sciences Conference, Eurotherm 2012. Along with this article appendix F is attached for further documentation. The purpose of part II is to further investigate the heat transfer in mini channels using an experimental method. This is not a part of the collaboration with Danfoss, but it represents an interesting alternative way of finding the heat transfer in mini channels.

Along with this project documentation a CD is included. The content on the CD is twofold by a part I and a part II. The files for part I includes EES, MATLAB, and SolidWorks models made in this project. Two ANSYS case files used in the CFD simulation are also included. Furthermore, the LabVIEW files used in the experiment in part I are found on the CD. For part II the data processing scripts made in MATLAB are included, along with calibration and experiment TIFF-images. A PDF version of this report is also found of the CD.

Reading Instructions

The references appear throughout the report, and a bibliography appears in the back of the report. The references are used according to the Harvard method, i.e. the references in the text is given in the following way; [surname, year], or surname [year]. If the reference is put after the dot, the reference applies to the whole paragraph, and if the reference is put before the dot the reference only applies to the concerned sentence. Furthermore, figures, tables and equations are numbered according to the chapter, i.e. the first figure in, for instance, chapter 2, will be numbered as 2.1, the next figure as 2.2, and so on. Explanatory text in attachment to figures and tables is written below.

In the various contour plots from the CFD simulations an explanatory figure is provided in the top right corner of the plot.

Nomenclature

Symbol	Specification	Unit	Symbol	Specification	Unit
A	Area	$[m^2]$	Re	Reynolds number	$[-]$
A	Fraction of collected light	$[-]$	S	Jet-to-jet spacing	$[m]$
B	Thermistor B-value	$[K]$	S	Skewness	$[-]$
C	Concentration	$\left[\frac{mol}{m^3}\right]$	T	Temperature	$[K]$
C_f	Friction coefficient	$[-]$	t	Thickness	$[m]$
c_p	Specific heat capacity, constant pressure	$\left[\frac{J}{kg\,K}\right]$	$\dot{V}$	Volume flow	$\left[\frac{m^3}{s}\right]$
c_v	Specific heat capacity, constant volume	$\left[\frac{J}{kg\,K}\right]$	v	Velocity	$\left[\frac{m}{s}\right]$
D	Diameter	$[m]$	U	Voltage	$[V]$
D_h	Hydraulic diameter	$[m]$	u_τ	Friction velocity	$\left[\frac{m}{s}\right]$
F	Nusselt number coefficient	$[-]$	W	Width	$[m]$
f	Friction factor	$[-]$	W	Work	$[J]$
G	Nusselt number coefficient	$[-]$	x	Distance	$[m]$
H	Nozzle-to-plate spacing	$[m]$	$\bar{x}$	Sample mean	$[-]$
h	Convection heat transfer coefficient	$\left[\frac{W}{m^2\,K}\right]$	y^+	Dimensionless wall distance	$[-]$
I	Fluorescence intensity	$[cd]$	z	Nozzle-to-plate spacing	$[m]$
I	Turbulence intensity	$[-]$	z	Upper critical value	$[-]$
I_0	Excitation intensity	$[cd]$	α	Scaling factor	$[-]$
i	Specific internal energy	$\left[\frac{J}{kg}\right]$	ΔT	Temperature difference	$[K]$
K	Nusselt number coefficient	$[-]$	Δp	Pressure loss	$[Pa]$
K_L	Fluid loss coefficient	$[-]$	Δy_p	Distance to first cell	$[m]$
k	Thermal conductivity	$\left[\frac{W}{m\,K}\right]$	δ	Boundary layer thickness	$[m]$
k	Turbulent kinetic energy	$\left[\frac{m^2}{s^2}\right]$	ε	Roughness	$[m]$
L	Length	$[m]$	ε	Molar absorptivity	$\left[\frac{m^2}{mol}\right]$
m	Mass	$[kg]$	ε	Turbulent dissipation rate	$\left[\frac{m^2}{s^3}\right]$
$\dot{m}$	Mass flow rate	$\left[\frac{kg}{s}\right]$	θ	Angle	$[^\circ]$
Nu	Nusselt number	$[-]$	λ	Wave length	$[m]$
n	Number of samples	$[-]$	μ	Dynamic viscosity	$\left[\frac{kg}{m\,s}\right]$
P	Power	$[W]$	μ	Population mean	$[-]$
Pr	Prandtl number	$[-]$	ν	Kinematic viscosity	$\left[\frac{m^2}{s}\right]$
Q	Heat transfer rate	$[W]$	ρ	Density	$\left[\frac{kg}{m^3}\right]$
$\dot{q}$	Heat flux	$\left[\frac{W}{m^2}\right]$	σ	Standard deviation	$[-]$
R	Electrical resistance	$[\Omega]$	τ	Shear stress	$[Pa]$
R	Specific gas constant	$\left[\frac{J}{kg\,K}\right]$	ϕ	Quantum yield	$[-]$
R	Thermal resistance	$\left[\frac{K}{W}\right]$	ω	Frequency of large eddies	$[1/s]$

Subscripts

Subscript	Specification	Subscript	Specification
app	Application	o	Outlet
$coll$	Collector	max	Maximum
$cond$	Conduction	$mean$	Mean
$conv$	Convection	min	Minimum
$cooling$	Cooling	r	Ratio
e	Equiangular	$pump$	Pump
e	Excitation	s	Surface
$electrical$	Electrical	sec	Section
f	Fluorescence	$thermal$	Thermal
fin	Fin	$thermistor$	Thermistor
$fluid$	Fluid	$wall$	Wall
GE	Gate-to-emitter	$water$	Water
i	Inlet	0	Ambient
j	Junction	∞	Infinity
ln	Logarithmic		

Summary

This project is divided into two parts. Part I is made in collaboration with Danfoss Power Electronics A/S, where the focus is to design a cold plate using single phase cooling to give an effective cooling performance of a Danfoss IGBT power module, with low pumping power requirements. Effective cooling performance is here defined as a cold plate ensuring low junction temperature, and uniform temperature distribution in the IGBT power module. This is due to higher risk of failure with increasing junction temperature and uneven temperature distribution. A low junction temperature is also found to increase the efficiency of the IGBT power module. The IGBT power module has its purpose in automotive applications, and thus the pumping power requirements should be low.

Four cold plate designs are considered, as shown in figure 1, where the naming of the designs are shown. All designs are investigated using CFD simulations, whereas only the multijet and hybrid designs are tested experimentally.

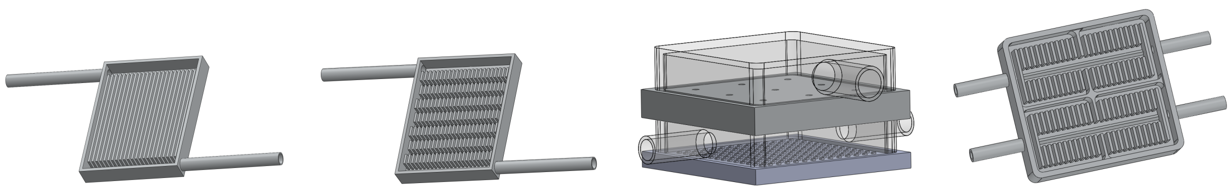

(a) *Mini channels.* (b) *Staggered fins.* (c) *Multijet.* (d) *Hybrid.*

Figure 1: *Different cold plate designs.*

The CFD simulations show, that the multijet and hybrid designs are superior to the mini channel and staggered fins designs. This is shown in figure 2 (a) and (b), where a low standard deviation in figure 2 (a) represents a good temperature uniformity, and figure 2 (b) shows maximum temperature.

The multijet and hybrid designs are compared to the commercial cooling device ”Shower Power”, where the convective heat transfer coefficient is shown to be higher for the multijet and hybrid designs at higher pumping powers, see figure 3.

The cooling performance experiments of the multijet and hybrid designs show good cooling performance, where the pressure loss and temperature difference between inlet and junction is shown to match the CFD simulated pressure loss and temperatures.

Part II consists of an article prepared for the 6th European Thermal Sciences Conference, Eurotherm 2012. The purpose of this part is to investigate the heat transfer in mini channels using the technique planar laser induced fluorescence (PLIF). This technique uses the principle of laser excitation of rhodamine B in water. The goal of the study is to validate the applicability of PLIF to determine the convective heat transfer coefficient in mini

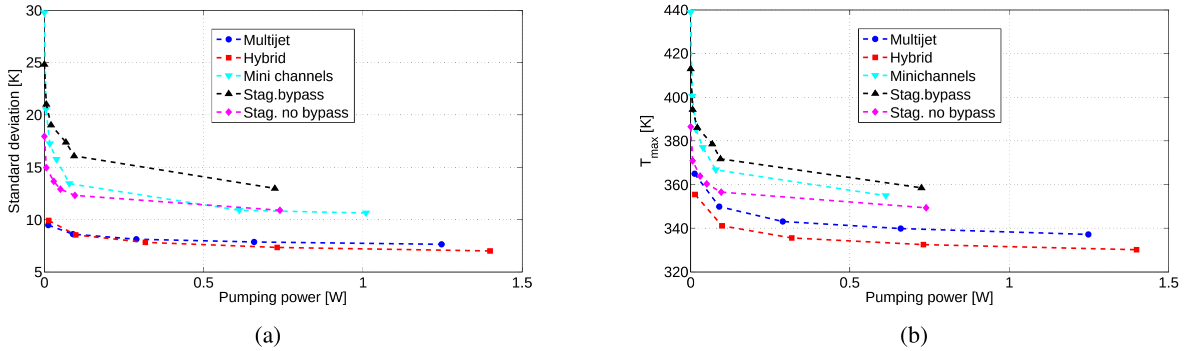

Figure 2: *(a) Standard deviation of temperatures on back side of cold plate and (b) maximum temperature on back side of cold plate.*

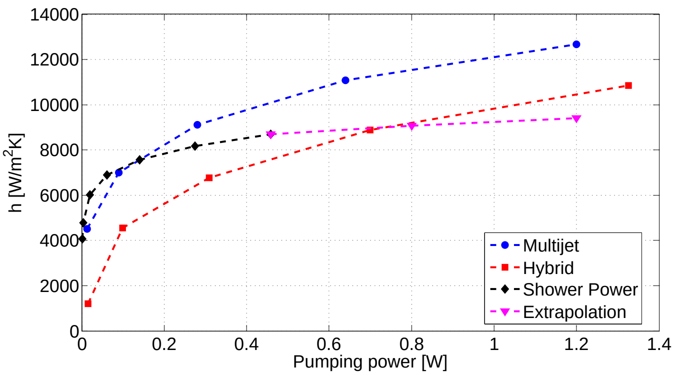

Figure 3: *h-value versus pumping power for Shower Power, hybrid and multijet design.*

channels against conventional correlations.

The experiment shows good agreement to the conventional correlation, and the resolution of the temperature gradient at the wall is found sufficiently accurate to determine the average convective heat transfer coefficient, see figure 4 (a). PLIF is however not found satisfactory over the whole domain, and it is found that it cannot be used for determination of the convective heat transfer coefficient in a single point, see figure 4 (b).

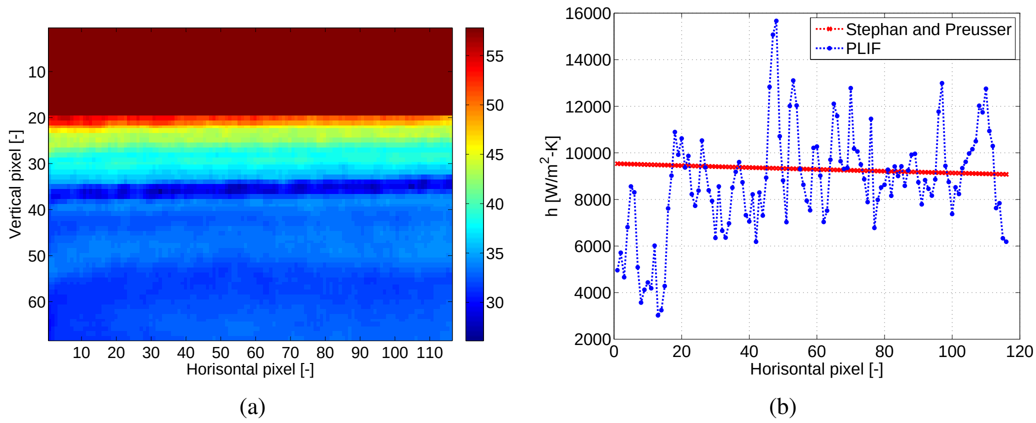

Figure 4: *(a) Contour plot of temperatures in mini channel and (b) h-values in the same domain compared to conventional correlation.*

Contents

Investigation and Design of Cold Plates for High Heat Flux Electronics

I

1 Introduction

The removal of heat from high heat flux electronics is gaining critical importance in many systems as the power densities today continue to increase. Heat fluxes in the order of 250 W/cm^2 have already been realized [Parida et al., 2012]. In future years the heat flux could reach as high as 10,000 W/cm^2 due to the ever-increasing packing density of electronics. It is especially in applications such as active radars, light emitting diodes, laser systems, and hybrid electric vehicles the heat dissipation will become the bottleneck towards higher performance with regards to the life-time and product reliability. [Zhou et al., 2010] This continuous development of high power electronics creates a demand for advanced liquid cooling solutions, as conventional air cooling is not able to meet these demands [Kandlikar and Hayner, 2009]. The state of art cooling schemes shows convective heat transfer coefficients in the range of 40 $kW/m^2\,K$ for single phase cooling [Parida et al., 2012].

The higher power density is a consequence of Moore's law which states that the number of transistors that can be placed on a integrated circuit doubles every second year, and at the same time small and light-weight products are getting more and more common, hence the thermal management of such devices becomes a bigger challenge, even though the devices at the same time also gets more energy efficient [Zorian and Gizopoulos, 2005].

Cooling is important because of several reasons. Without proper cooling the electronics can be damaged, and hence the performance, lifetime and reliability of the electronic devices are all reduced. To much excess heat in the device can also increase the movement of free electrons which can cause signal noise [Remsburg, 2001]. Figure 1.1 shows that the failure time increases with higher junction temperature for different transistors. The junction temperature is the highest temperature of a semiconductor in an electronic device.

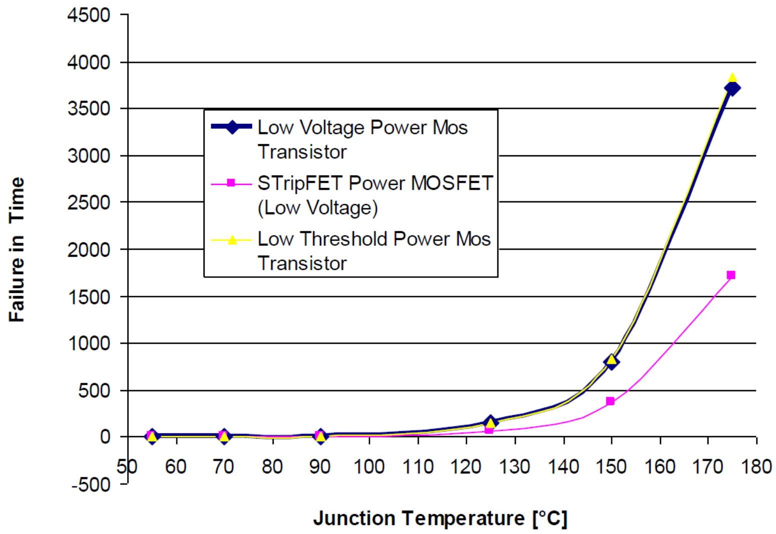

Figure 1.1: *Failure time as a function of junction temperature for different transistors [ST Microelectronics, 2002].*

The higher the operating temperature, the risk of power transients, electrical noise, and local heating effects becomes higher. As a good rule of thumb the failure rate doubles when the temperature is increased with 10-15 $°C$, when the operating temperature is above 50 $°C$ [Kandlikar and Hayner, 2009]. A common maximum temperature for silicon devices are 125 $°C$, as the failure rate increases significantly above this point. In the case of insulated-gate bipolar transistors (IGBT) a leakage current leads to heating in the device, and this leakage current increases when the temperature increases. This leads to a significant dissipation of power inside the IGBT, and it is not uncommon that 10 % of the total load is lost because of this [Kandlikar and Hayner, 2009].

In general a device within power applications performs better at lower temperatures. This tendency is shown in figure 1.2 where a junction temperature of 125 $°C$ gives a higher output than a junction temperature of 150 $°C$ for an IGBT power module.

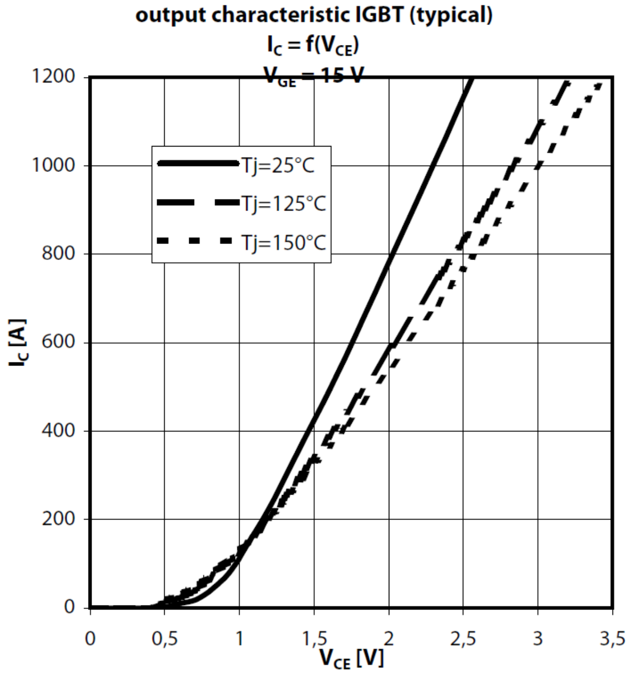

Figure 1.2: *Output characteristics for IGBT at various junction temperatures [Stroebel, 2012].*

It is important to have a uniform temperature distribution in the given device because of the difference in thermal coefficient of expansion for each of the different materials the device consist of. The material interaction in the interfaces becomes a major concern for the lifetime, as internal stresses can get too high if the temperature difference over the cooling device is large [Kandlikar and Hayner, 2009]. In chapter 4 the different thermal coefficients of expansion for the materials of an IGBT, to which cooling solutions are designed, are stated.

When designing a cooling device the above considerations must be taken into account to make a reliable solution, but at the same time the pressure loss over the device must be taken into account. Having a high flow rate, and thereby a high Reynolds number, enhances the cooling ability, but this will at the same time increase the demand for pumping power, and may require a heavier pump. A thing to notice is that a high Reynolds number could induce a shorter lifetime. However another important thing to notice is, that the switching losses are lower at lower temperature, and hence the increased pump power may be worth spend.

Colgan et al. [2007] have made several micro channel coolers, and from their studies it clearly seen how the thermal resistance are lower with a higher mass flow rate, which gives a lower junction temperature. This is shown in figure 1.3 where the pressure loss at an increasing flow rate also is shown.

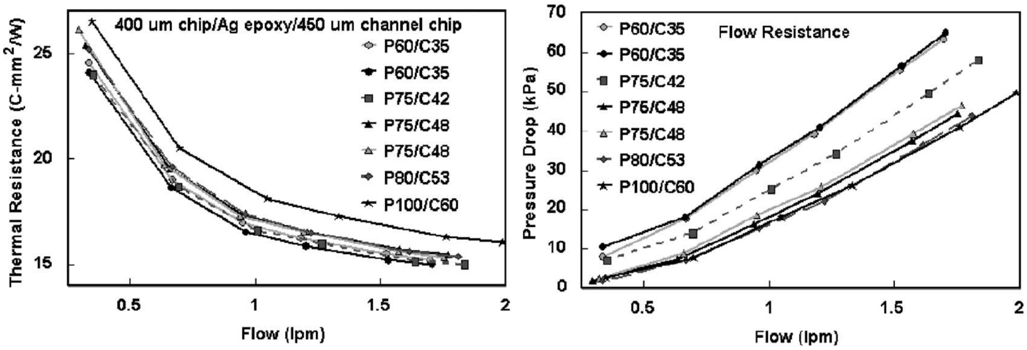

Figure 1.3: *Lower thermal resistance and higher pressure loss at a higher flow rate [Colgan et al., 2007].*

2 Problem Statement

It is evident that thermal cooling solutions need to be improved in order to maintain the reliability of electronic devices in the future. The basis for this project is to develop a liquid based cold plate which gives a sufficient cooling of an IGBT power module from Danfoss Power Electronics A/S. Sufficient cooling meaning low junction temperature and good temperature distribution. The IGBT power module is described in chapter 4. It is also a goal to have as high a convective heat transfer for the cold plate as possible, while keeping the pumping power at a minimum.

Based on the above, the problem statement for this project is:

How can a cold plate, based on single phased cooling, be designed to give an effective cooling performance, with a low pumping power requirement, of a Danfoss DP 200B6600T-103800 IGBT power module?

The scope of the project is to make different cold plate designs based on ideas from the literature. The designs are then evaluated by means of CFD analysis, and the manufactured designs are also evaluated experimentally.

The designs are constrained with what is possible to manufacture in the departments workshop. This becomes an issue when micro-scale fin, bends, etc. is to be milled out in the cold plate. Because of a high work load in the workshop the number of designs manufactured is constrained to two.

The designs made in this project are prototypes. To make these designs commercial available, certain adaptions must be made. In the long run it would be an economically advantage if these designs could be made by casting. This is elaborated in chapter 10.

Heat Transfer 3

This chapter describes the theory and principles of heat transfer used throughout this report. The concepts of micro channels and jet impingement are discussed in this chapter. This chapter consists of the following sections:

3.1 Conservation of Energy

The first law of thermodynamics states that "energy can neither be created nor destroyed; it can only change forms" [Cengel, 2006]. Hence, energy is always conserved. When modeling the different thermal systems in this project, the following equation is used to calculate how the energy is conserved:

$$\dot{Q} = \dot{m} \cdot c_p \cdot (T_o - T_i) \qquad [W] \tag{3.1}$$

When a constant surface temperature is assumed the heat transfer is calculated by [Cengel, 2006]:

$$\dot{Q} = h \cdot A_s \cdot \Delta T_{ln} \qquad [W] \tag{3.2}$$

where

$$\Delta T_{ln} = \frac{\Delta T_o - \Delta T_i}{(\Delta T_o / \Delta T_i)} \qquad [K] \tag{3.3}$$

and

$$\Delta T_o = T_s - T_o \quad [K] \tag{3.4}$$

$$\Delta T_i = T_s - T_i \quad [K] \tag{3.5}$$

3.2 Heat Transfer Theory

Figure 3.1 shows the principle of heat transfer involving three basic mechanisms [Cengel, 2006]:

- Conduction: Result of interaction between particles with different energy levels.
- Convection: Heat transfer between solid and adjacent moving fluid.
- Radiation: Energy emitted by matter in the form of photons.

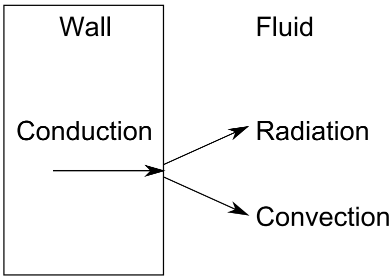

Figure 3.1: *Heat transfer mechanisms [Cengel, 2006].*

Fourier's law of heat conduction states [Cengel, 2006]:

$$\dot{Q}_{cond} = -k \cdot A \cdot \frac{dT}{dx} \qquad [W] \tag{3.6}$$

This concludes, that the rate of heat transfer through a material is proportional to: The thermal conductivity, the area normal to the direction of heat transfer and the temperature difference. It is inversely proportional to the thickness of the material. A high thermal conductivity is preferred for effective heat transfer and is dependent on the material. The thermal conductivity for various materials is listed in table 3.1 and figure 3.2. Unfortunately, the better the thermal conductivity in the material, the more expensive it often is. For instance the price of aluminium is 2 $^{\$}/_{kg}$ while the price of copper is 8 $^{\$}/_{kg}$ [Metalprices, 2012].

	Material	$\boldsymbol{k}$ $[^{W}/_{m\,K}]$
Solids	Diamond	2300
	Copper	401
	Aluminium	237
Fluids	Water	0.607
	Air	0.026

Table 3.1: *Thermal conductivities for various materials at room temperature [Cengel, 2006].*

Newton's law of cooling states [Cengel, 2006]:

$$\dot{Q}_{conv} = h \cdot A_s \cdot (T_s - T_\infty) \qquad [W] \tag{3.7}$$

This concludes, that the heat transfer from a solid to a moving fluid is proportional to: The heat transfer coefficient, surface area between solid and moving fluid, and the temperature difference between the surface and the free stream fluid. The convective heat transfer is often the bottleneck problem, and much effort is made

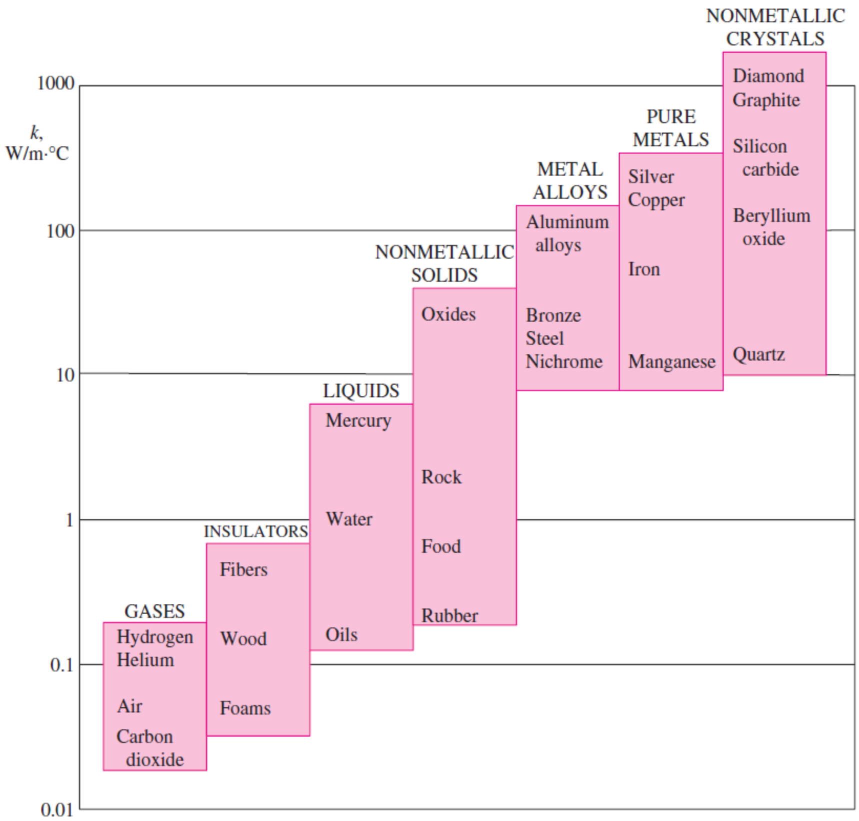

Figure 3.2: *Thermal conductivities for various materials at room temperature [Cengel, 2006].*

to increase the convective heat transfer. One solution is to increase the surface area by various means, but the fluid mechanical interesting solution is to increase the convective heat transfer coefficient, because this is highly affected by the fluid motion. Besides the velocity, the convective heat transfer also depends on the fluid properties such as the dynamic viscosity, conductivity, density, specific heat, and also the surface roughness. The convective heat transfer coefficient for various cases is listed in table 3.2. Liquid cooling has big potential, and two-phase cooling has an even bigger potential. It is seen, that the motion of the fluid greatly influences the convective heat transfer coefficient.

h $[W/m^2\,K]$	**Gas**	**Liquid**
Free convection	2-25	10-1000
Forced convection	25-250	50-20,000
Boiling and condensation	2500-100,000	

Table 3.2: *The convective heat transfer coefficient for various cases [Cengel, 2006].*

The size of both the hydrodynamic and thermal boundary layer is important with regards to the heat transfer. The boundary layer thickness, δ, is defined as the distance y normal to the surface where the velocity is equal the 0.99 times the free stream velocity. This is shown on the left side in figure 3.3.

On the right side in figure 3.3 the thermal boundary layer is shown. The thickness of the thermal boundary layer, δ_t, is defined as the distance away from the surface where the temperature difference $T - T_s$ equals

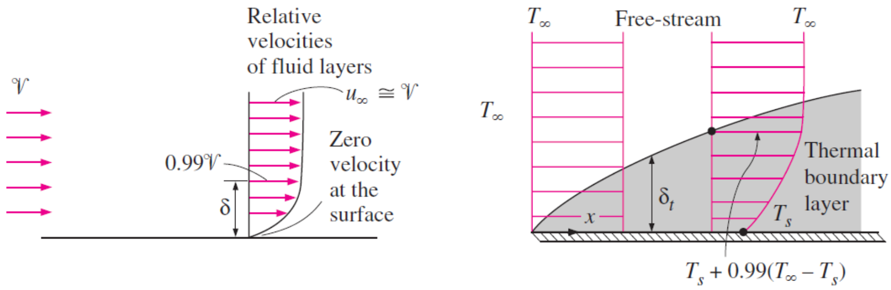

Figure 3.3: *Size of boundary layers [Cengel, 2006].*

$0.99(T_\infty - T_s)$.

The type of forced flow greatly influences the convective heat transfer coefficient. The flow may either be laminar, transitional or turbulent. The flow type is often determined by evaluating the Reynolds number. This is defined as [Cengel, 2006]:

$$Re = \frac{\rho \cdot v \cdot x}{\mu} \qquad [-] \tag{3.8}$$

ρ and μ are fluid properties, while v is the velocity. The characteristic length x may be the hydraulic diameter of e.g. a pipe, or the length of a flat plate. For the case of forced convection over a flat plate, the convective heat transfer coefficient and friction factor vary depending on the Reynolds number. This is shown in figure 3.4 for isothermal surfaces. The boundary layer thickness grows as the flow increase in Reynolds number. The local convective heat transfer coefficient decreases in the laminar zone towards the transitional zone, as a result of smooth and streamlined flow, and with an increase in boundary layer thickness. The h-value increase in the transitional zone as the flow is disturbed and better heat and mass transfer occur. The maximum h-value is reached when the flow is fully turbulent, which is characterized by a highly disordered motion.

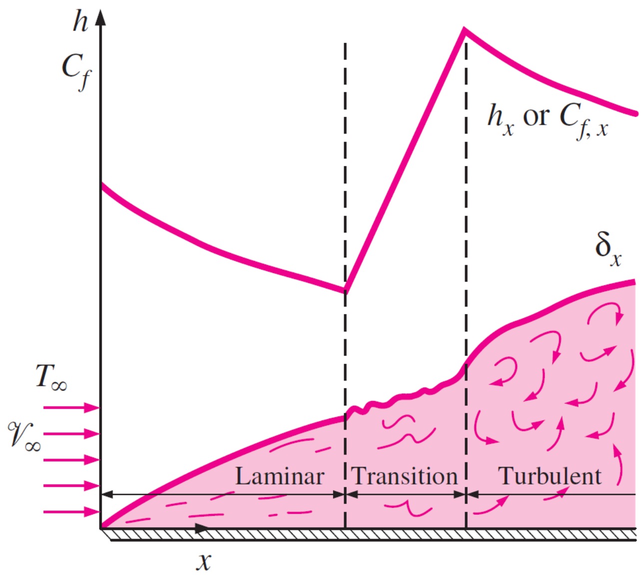

Figure 3.4: *Variation of friction factor and convective heat transfer coefficient for external flow over a flat plate [Cengel, 2006].*

Looking at the friction factor in figure 3.4, the friction factor has the same tendency as the convective heat transfer coefficient. This is because of the analogy between fluid dynamic viscosity and fluid thermal conductivity. The convective heat flux is defined as [Cengel, 2006]:

$$\dot{q}_{conv} = h \cdot \Delta T \qquad \left[\frac{W}{m^2}\right] \tag{3.9}$$

The conductive heat flux is defined as [Cengel, 2006]:

$$\dot{q}_{cond} = k_{fluid} \cdot \frac{\partial T}{\partial y} \qquad \left[\frac{W}{m^2}\right] \tag{3.10}$$

Due to the no-slip condition at the wall, the following equation is valid [Cengel, 2006]:

$$\dot{q}_{cond} = \dot{q}_{conv} = k_{fluid} \cdot \left.\frac{\partial T}{\partial y}\right|_{y=0} \qquad \left[\frac{W}{m^2}\right] \tag{3.11}$$

The wall shear stress is defined as [Cengel, 2006]:

$$\tau_w = \mu \cdot \left.\frac{\partial u}{\partial y}\right|_{y=0} \qquad [Pa] \tag{3.12}$$

The ratio between the conductivity and viscosity is described by the Prandtl number:

$$Pr = \frac{\mu\, c_p}{k_{fluid}} = \frac{\text{Molecular diffusivity of momentum}}{\text{Molecular diffusivity of heat}} \qquad [-] \tag{3.13}$$

The Prandtl number is an expression of the relative thickness between the velocity and the thermal boundary layer. Water has a Prandtl number of 7 at room temperature, which indicates, that the shear stress is high compared to the ability to transfer heat within the water. Or with other words that the development of the thermal boundary layer is slower than the development of the velocity boundary layer.

By isolating k_{fluid} in equation (3.11), and μ in equation (3.12) the following expression for the Prandtl number is derived:

$$Pr = \frac{\frac{\tau_w}{\left.\frac{\partial u}{\partial y}\right|_{y=0}} \cdot c_p}{\frac{\dot{q}_{conv}}{\left.\frac{\partial T}{\partial y}\right|_{y=0}}} \qquad [-] \tag{3.14}$$

Due to this derivation the convective heat flux is dependent on the wall shear stress:

$$\dot{q}_{conv} = f(\tau_w) \tag{3.15}$$

The friction coefficient is a function of the wall shear stress, and is defined as [Cengel, 2006]:

$$C_f = \frac{\mu \cdot \left.\frac{\partial u}{\partial y}\right|_{y=0}}{\rho u_\infty^2/2} \qquad [-] \tag{3.16}$$

The pressure loss is a function of the friction coefficient:

$$\Delta p = C_f \cdot \frac{L}{D} \cdot \frac{\rho \cdot V^2}{2} \qquad [Pa] \tag{3.17}$$

Because the pressure loss and the convective heat fluxes are a function of the wall shear stress, there is a correlation between the pressure loss and the heat transfer:

$$\dot{Q} = f(\Delta P) \tag{3.18}$$

Equation (3.18) shows that the cooling ability of a design is a function of the pressure loss in the design, and thereby it may be worthwhile to increase the pressure loss. Hence, a turbulent flow yields a higher heat transfer than a laminar flow.

The temperature gradient at the wall is directly related to the value of the convective heat transfer coefficient. A larger gradient results in a higher h-value by equation (3.11). The boundary layer thickness influences the gradient at the wall, and the larger the gradient, the smaller the boundary layer thickness. Thus a thin boundary layer is preferred along with a developing flow.

3.3 Heat Transfer Enhancement Methods

In general breaking down or disturbing the hydrodynamical boundary layer increases mixing and thereby the heat transfer is enhanced. A consequence of this is often an increased pressure loss. Increased mixing is a way to replace hot fluid with colder fluid, which is a mass transfer mechanism. Methods to enhance heat transfer are:

- **Blunt objects and surface roughness**. This category is also called displayed enhancement devices. Examples hereof is mesh, rings, disks or balls, as proposed by Rohsenow et al. [1998]. The best technique is the one that combines maximum heat transfer enhancement with as little increase in friction factor, and thereby pressure loss, as possible. The enhanced heat transfer is often combined with the increased surface area, and thus the direct effect of the flow mechanism may be difficult to analyze. Kakac et al. [1987] suggests surface roughness in the form of pyramids and ribs to provoke flow separation and mixing. This is shown in figure 3.5.
- **Flow benders**. This promotes separation in the flow, and with a wide bend the pressure loss is not compromised [Danfoss, 2012]. Separation of the flow promotes mixing and turbulence.
- **Jet impingement**. By directing a jet towards a heat source, the local Nusselt number is usually very high, but quickly dies out in the surroundings of the jet. Due to the simple geometry, the pressure loss is relative low according to Mudawar [2005].
- **Extended surface area**. This may be in the form of fins as this leads to distortion of the flow field. Elliptic fins are preferable compared to round or square fins according to Remsburg [2007].
- **Pulsating flow**. Generally a pulsating flow enhances the heat transfer because the hydrodynamical boundary layer is destroyed, and thus the thermal resistance is reduced because the thermal boundary layer is also disturbed [Jun et al., 2004].
- **Swirl flow**. This leads to better mixing as velocity fluctuations are inherent in swirl flows, hence giving higher heat transfer.

- **Additatives in fluid**. Particles in the fluid increase the turbulence, and thereby mixing and heat transfer.
- **Increasing flow velocity**. A higher Reynolds number results in a higher Nusselt number by theory, but also results in a higher pressure loss.
- **2-phase cooling**. The phase change results in an increase in heat transfer coefficient of 3-4 times as shown in table 3.2. The problem lies in the demanding pressure levels and manufacturing complexity, which increase the cost.

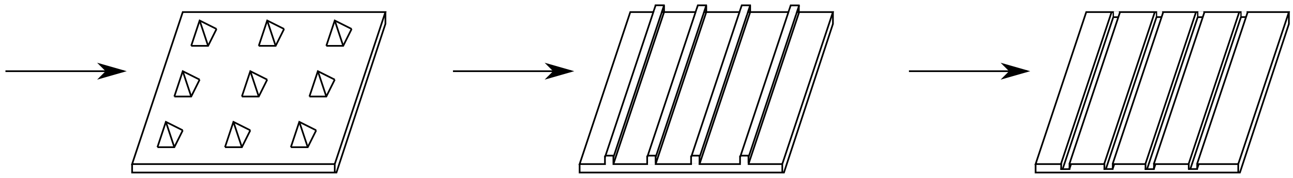

Figure 3.5: *Flow over various surface roughnesses proposed by Kakac et al. [1987].*

3.4 Micro Channels

In this section an investigation of heat transfer in micro channels is made. Firstly, theory about micro scale heat transfer is presented and secondly an analytical model is developed which is also validated by a numerical analysis.

Channel prefixes are shown in table 3.3, which is defined by Kandlikar and Grande [2002].

Conventional channels	$D_h > 3\ mm$
Mini channels	$3\ mm \geqslant D_h > 200\ \mu m$
Micro channels	$200\ \mu m \geqslant D_h > 10\ \mu m$
Transitional channels	$10\ \mu m \geqslant D_h > 0.1\ \mu m$
Molecular Nano channels	$0.1\ \mu m \geqslant D_h$

Table 3.3: *Channel prefixes defined by Kandlikar and Grande [2002].*

Micro channels are defined to be channels with a hydraulic diameter in the range of 10-200 μm [Kandlikar and Bapat, 2007], where as mini channels are defined to be channels with a hydraulic diameter in the range of 200 μm - 3 mm. When looking at micro channels the main advantage is the high heat transfer area pr. unit volume. Also the hydraulic diameter is important, due to the relation of the convective heat transfer coefficient [Cengel, 2006]:

$$h = \frac{k_{fluid} \cdot Nu_\infty}{D_h} \tag{3.19}$$

For a given fluid, the way to significantly increase h in micro channels is to reduce the hydraulic diameter D_h to micro scale levels, and channels of micro scale width. The only lower limit on D_h is the pump power available and the coolant viscosity, due to the increasing shear stresses for increasing surface area.

Following Tuckerman and Pease [1981] a collection of n parallel channels of length L is integrated in a plate of length L and width W. A coolant flows in the channels absorbing $\dot{Q}/n{\cdot}L$ heat pr. unit length. Using channels in stead of a flat plate, the surface area may be scale by a factor α, which is defined as:

$$\alpha = \frac{\text{Total surface area of channel in contact with coolant}}{\text{Area of plate}} \tag{3.20}$$

It is here assumed that the channel walls are infinitely conductive, so the temperature is uniform around the channel perimeter. The heat transfer is defined as Newton's law of cooling, which is rewritten in this case:

$$\dot{Q} = h \cdot A_s \cdot \Delta T = h \cdot \alpha \cdot L \cdot W \cdot \Delta T \qquad [W] \tag{3.21}$$

For a given area $L \cdot W$, the way of making $\dot{Q}$ larger is by decreasing the hydraulic diameter as seen in equation (3.19), and increase α, by increasing the number of channels, as seen in equation (3.21).

3.4.1 Discretized Analytical Model

A 3D generic discretized mini channel model is made in MATLAB to understand the heat transfer in these channels. The model is generic, because all physical parameters may be scaled to a specific problem. A representation of the model is shown in figure 3.6. Each discretization point of the mini channel is set up in four blocks: fin, water, left, and right base. Due to symmetry only half of the water channel and half of the fin is modeled.

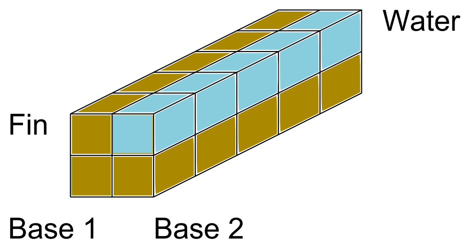

Figure 3.6: *3D discretization sketch.*

The geometric parameters in the model is shown in table 3.4. The fin is assumed to be made of aluminium with a thermal conductivity of 236.1 $W/m\,K$.

Parameter	**Length [mm]**
Channel width	0.5
Fin width	0.5
Fin height	6
Channel length	7.5
Height of base plate	2

Table 3.4: *Geometric inputs to mini channel model.*

In figure 3.7 a representation of the heat transfer in each individual interior block is shown. For the two base blocks there is a heat addition ($\dot{Q}$) in the bottom. Besides this, there is only conductive heat transfer (k) for the left base, while there is added convective heat (h) to the water transfer for the right base. For the water block (h) and an energy balance are considered ($\dot{Q} = \dot{m} \cdot c_p \cdot \Delta T$). For the fin both ($h$) and ($k$) are considered.

In figure 3.8 the boundary conditions for the heat transfer in the blocks is shown.

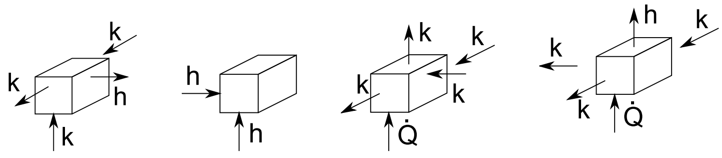

(a) *Fin.* (b) *Water.* (c) *Left base.* (d) *Right base.*

Figure 3.7: *Heat transfer in the control volume interior discretization.*

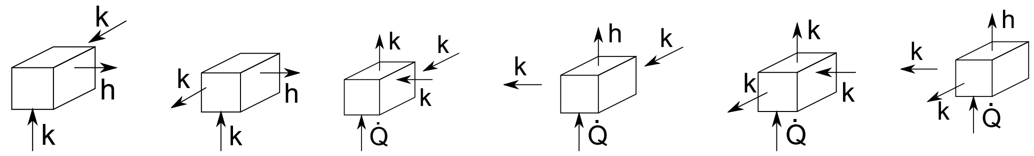

(a) *Fin inlet.* (b) *Fin outlet.* (c) *Left base inlet.* (d) *Right base inlet.* (e) *Left base outlet.* (f) *Right base outlet.*

Figure 3.8: *Heat transfer in the control volume BC discretization.*

The equation used for calculating the convective heat transfer is [Cengel, 2006]:

$$\dot{Q}_{conv} = h \cdot A \cdot (T_{fin} - T_{water}) \qquad [W] \tag{3.22}$$

The equation for calculating the conductive heat transfer is [Cengel, 2006]:

$$\dot{Q}_{cond} = k \cdot A \cdot \frac{\Delta T}{\Delta x} \qquad [W] \tag{3.23}$$

The Nusselt number in each discretization step is found by using the correlation by Stephan and Preusser [1979] when the flow is simultaneously developing the hydrodynamical and thermal boundary layer:

$$Nu = 4.364 + \frac{0.086 \cdot \left(Re \cdot Pr \cdot \frac{D_h}{L}\right)^{1.33}}{1 + 0.1 \cdot Pr \cdot \left(Re \cdot \frac{D_h}{L}\right)^{0.83}} \qquad [-] \tag{3.24}$$

This correlation assumes a circular tube and a constant wall heat flux. Even though the approximation is for a circular tube, the correlation is still valid as the hydraulic diameter is changed correspondingly [Lee et al., 2005]. The hydrodynamical entry length is calculated, and when the flow is developed hydrodynamically the following correlation by Shah and London [1978] is used instead to find the local Nusselt number, which is also valid for constant wall heat flux:

$$Nu_{x,H} = \begin{cases} 1.490(x^*)^{-1/3} & \text{for } x^* \leq 0.0002 \\ 1.490(x^*)^{-1/3} - 0.4 & \text{for } 0.0002 \leq x^* \leq 0.001 \\ 8.235 + 8.68(10^3 x^*)^{-0.506} e^{-164x^*} & \text{for } x > 0.001 \end{cases} \tag{3.25}$$

where x^* is the term denoting:

$$x^* = \frac{x/D_h}{RePr} \qquad [-] \tag{3.26}$$

The convective heat transfer coefficient in each point is then found by equation (3.19). In figure 3.9 the calculated h-values for the given inputs are shown. Only the correlation by Stephan and Preusser [1979] is in use in this case. Figure 3.9 shows that the h-value is largest in the beginning of the channel, where the boundary layer is smallest.

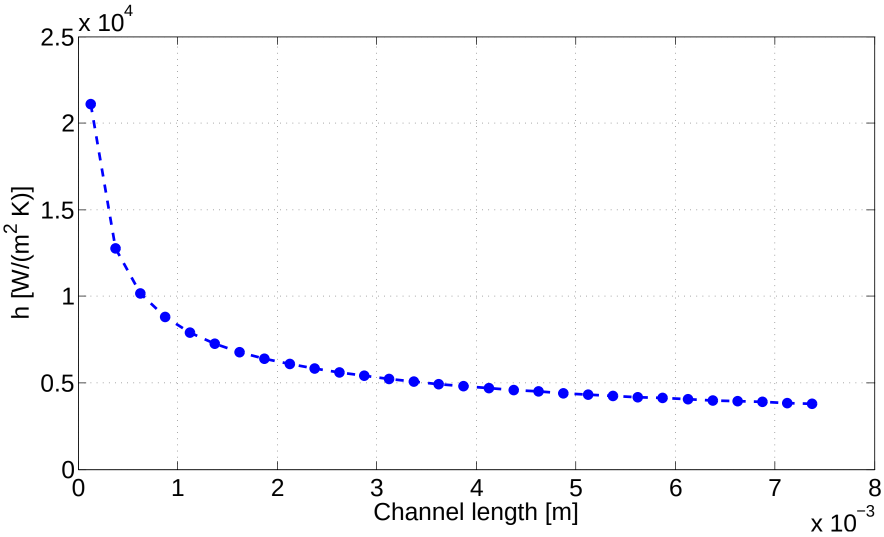

Figure 3.9: *Convective heat transfer coefficient through mini channel.*

The equations for each control volume is set up in a sparse matrix and solved in MATLAB using the backslash operator. The number of discretization points can be changed, which will increase the accuracy.

The inputs to the model is shown in table 3.5. The different thermodynamical properties at a water temperature corresponding to the inlet temperature are also inputs to the model.

Parameter	**Value**
Mass flow $[g/s]$	0.14
Water inlet temperature $[K]$	303.15
Heat flux $[W/m^2]$	240,000
Number of discretisations points [-]	30

Table 3.5: *Inputs to analytical model.*

The temperature distribution in the water, fin and base is shown in figure 3.10 with the given inputs in table 3.5. The heat input corresponds to 1.8 W. Only one of the base temperatures is shown, since they are alike. As expected, the hottest block is the base, followed by the fin and the water. In the start of the channel the temperature gradient is large due to a relatively high Nusselt number, and further downstream in the channel the temperature gradient flattens out.

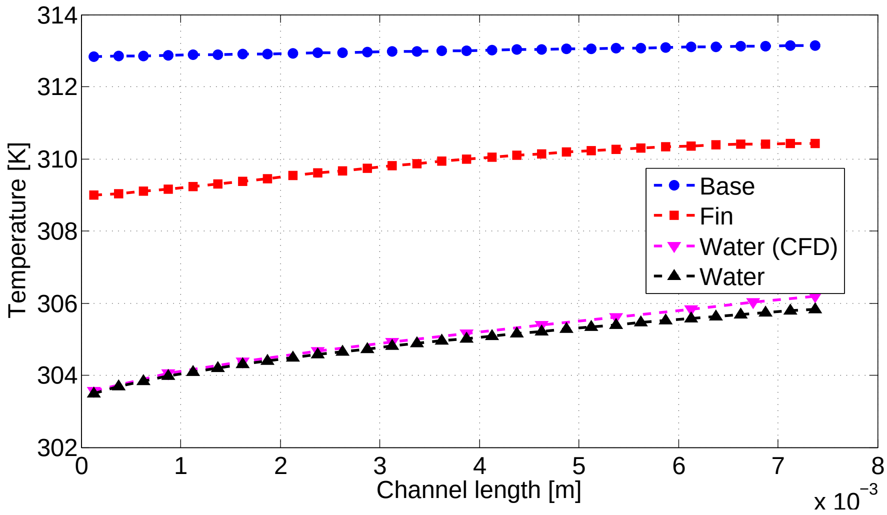

Figure 3.10: *Temperature distribution in fin, water and base along the mini channel. The h-values are based on Stephan and Preusser [1979].*

3.4.2 Validation of Analytical Model by CFD Analysis

A numerical model for the heat transfer in the mini channels is also made to verify the analytic model. The mesh for the simulation is made in ANSYS GAMBIT, and ANSYS FLUENT is used for the simulation. A mesh independency study of the mesh used in the simulation is carried out to ensure grid independency. The mesh is made up of 35,360 tetrahedral cells, where the mesh is refined close to the wall.

The simulation is made in 3D, and laminar flow is assumed, as the Reynolds number is equal to 101. The discretization order used is second order upwind. The boundary conditions consist of a uniform heat input in the bottom, and a mass flow of water into the domain. The simulation domain is shown in figure 3.11. Symmetry is also assumed for this numerical model, hence only half the width of both the mini channel and the fin is included in the simulation, and the boundary conditions is corrected to these dimensions. The geometry is the same as in table 3.4, and the boundary conditions is also the same as in table 3.5.

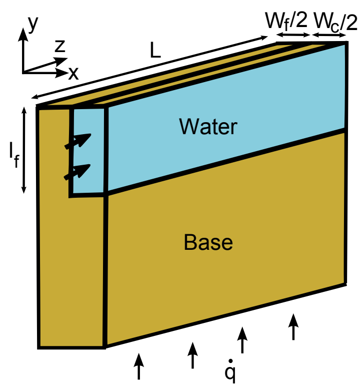

Figure 3.11: *Computational domain for CFD analysis.*

The distribution of the water temperature in the mini channel is shown in figure 3.10. The water temperature from the CFD analysis is in general seen to match the tendency from the analytic model, but there is however a slightly higher outlet temperature for water. To see if the base and fin temperature corresponds to the calculated temperature in the analytical model a contour plot of the fin and base temperature from the CFD analysis is shown in figure 3.12. The contour plot in this figure is a plane in the middle of the fin and the base, and it is seen that the temperatures in general are higher compared to the analytical model. The water enters the domain from the left side, and leaves the domain on the right side. It is seen that the temperatures are lower on the left side, and higher on the right side. This is due to water being heated downstream in the channel, and the build up of both the hydrodynamic and thermal boundary layer down through the channel.

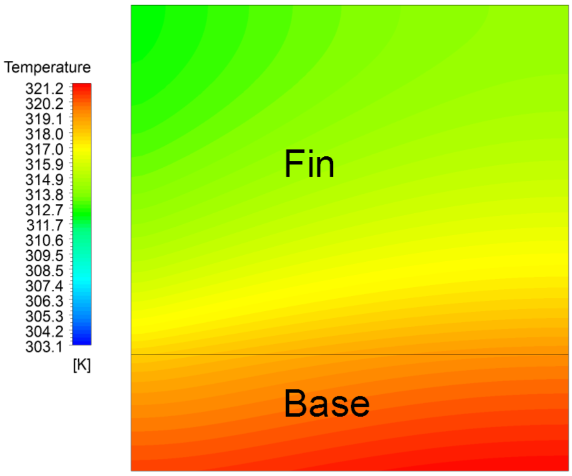

Figure 3.12: *Fin and base temperature in the middle of a fin.*

The build up of the thermal boundary layer in the channel is shown in figure 3.13, where the water close to the wall becomes warmer downstream.

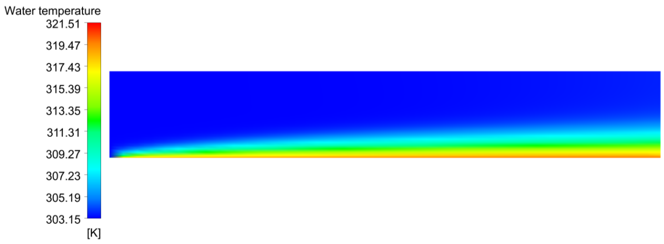

Figure 3.13: *Water temperature at the symmetry boundary.*

From the simulation it is concluded that neither a constant heat flux, or a constant wall temperature can be assumed on the boundary from the fin to the water. Hence, it is indeed necessary to vary the heat distribution in 3 dimensions in the analytical model of the mini channels to get an accurate model. It must be concluded that the analytical model cannot be fully validated, even though the water temperatures are similar.

To improve the analytical model, the geometry could be discretized in more than one direction for each block, which would give the possibility of resolving the temperature distribution better. A very important part of the model is the Nusselt number approximations. If the Nusselt number is wrong, so is the temperature distribution. The correlation used is for a circular geometry which could induce errors. The choice of which Nusselt correlation to use is the most important assumption is the analytical model. The correlation in use assumes simultaneously developing flow which gives relative high h-values, while if the correlation by Shah and London [1978] is used only thermally developing flow is assumed in parallel plates, yielding a higher fin and base temperatures due to the lower h-values, which is shown in figure 3.14.

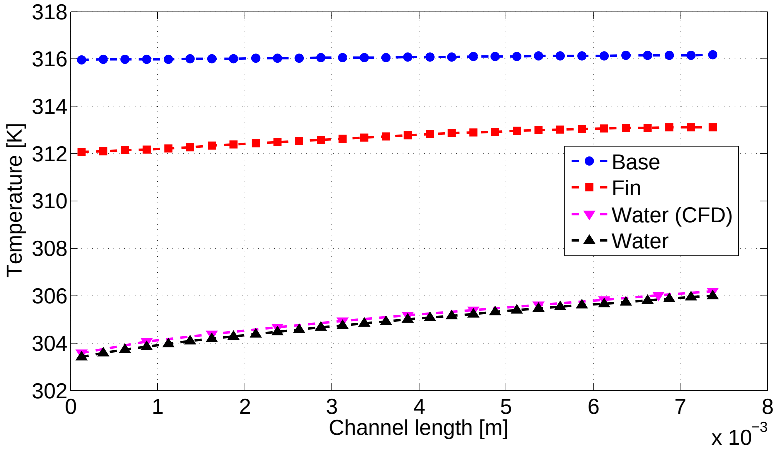

Figure 3.14: *Temperature distribution in fin, water and base along the mini channel where only a thermally developing boundary layer in the analytical model is assumed. The h-values are based on Shah and London [1978].*

From this it is concluded, that it is crucial to provide a realistic convective heat transfer coefficient to find the right temperature distribution in the fin. When determining which Nusselt number approximation to use it is also a choice between assuming a constant wall temperature, or by assuming a constant heat flux. Neither of these assumptions are perfectly valid when the heat addition is on a base under the fin. Assuming a constant heat flux therefore also constitutes a problem when validating the analytical model with the CFD analysis.

3.5 Jet Impingement

Liquid jet impingement cooling is characterized as a high convective cooling application. The h-value can reach 100 $^{kW}/_{m^2\,K}$ [Rohsenow et al., 1998]. The jet is discharged into an ambient fluid from a round nozzle (axisymmetric jet) or a slot nozzle (planar jet). The liquid jet is directed towards a target that requires cooling, that being e.g. a solid plate. The direction can be varied by an angle, if required. A sketch of an axisymmetric jet is shown on figure 3.15. The region of the jet where it is not affected by the surface is defined as the free jet. Within the impingement zone the flow is affected by the surface, and is decelerated. Due to momentum conservation, a wall jet is formed along the surface. The wall jet boundary layer will grow in thickness along the wall, but due to the overlaying fluid, the boundary layer can remain relatively thin.

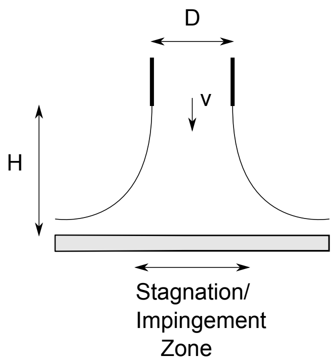

Figure 3.15: *Axisymmetric jet impingement configuration.*

For submerged jets a region called the potential core is formed when the jet exits the nozzle. The potential core is where the jet velocity remains largely unaffected by the ambient fluid. The potential core is typically four to eight nozzle diameters long, and high turbulence exists at its end. After this point the velocity of the jet decreases. [Webb, 1995] It is important to have the right nozzle-to-plate spacing. Especially for submerged jets because of the shear layer between the preimpinged jet and the ambient fluid.

3.5.1 Optimum Jet Height and Spacing

For cooling a large area, an array of jets is beneficial due to low heat transfer in the region away form the impingement region of a single jet. Martin [1977] investigated the heat transfer of an array of jets, see figure 3.16.

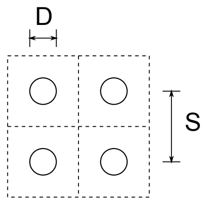

Figure 3.16: *Inline array of round jets.*

The average Nusselt number for an array of round jets is suggested by Martin [1977] to be

$$\overline{Nu} = K \cdot G \cdot F \cdot Pr^{0.42} \qquad [-] \tag{3.27}$$

where

$$K = \left[1 + \left(\frac{H/D}{0.6/A_r^{1/2}}\right)^6\right]^{-0.05} \tag{3.28}$$

$$G = 2 \cdot A_r^{1/2} \cdot \frac{1 - 2.2 \cdot A_r^{1/2}}{1 + 0.2 \cdot (H/D - 6) \cdot A_r^{1/2}} \tag{3.29}$$

$$F = 0.5 \cdot Re^{2/3} \tag{3.30}$$

For inline jets, the ratio of the nozzle exit cross-sectional area to the surface area of the cell, A_r, is

$$A_r = \frac{\pi \cdot D^2}{4 \cdot S^2} \tag{3.31}$$

The correlation is valid over the ranges

$$\begin{bmatrix} 2000 \leq Re \leq 100,000 \\ 2 \leq \frac{H}{D} \leq 12 \\ 0.004 \leq A_r \leq 0.04 \end{bmatrix} \tag{3.32}$$

Optimizing $\overline{Nu}$ with respect to S and H yields

$$H = 5 \cdot D \tag{3.33}$$

$$S = 1.6 \cdot H = 8 \cdot D \tag{3.34}$$

This optimum nozzle-to-plate spacing of $5 \cdot D$ is also seen in figure 3.17, where the stagnation Nusselt number for submerged water jets at various Reynolds numbers is shown. In the following, the optimal values of $H = 5 \cdot D$ and $S = 8 \cdot D$ is used.

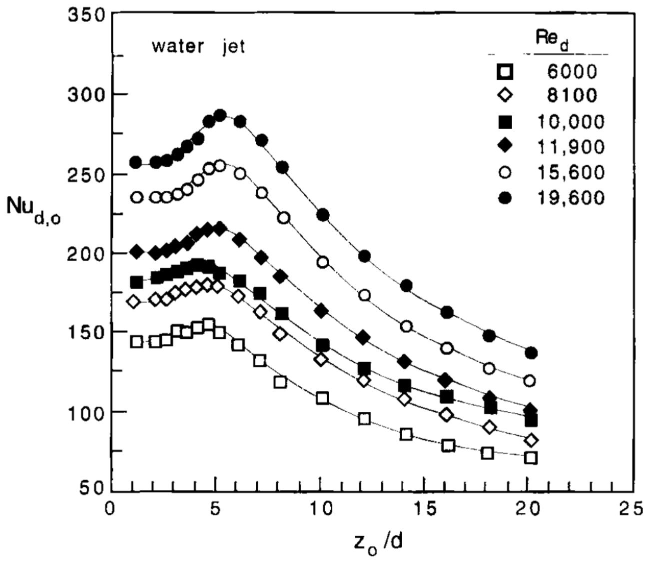

Figure 3.17: *Variation of Nusselt number at various Reynolds numbers for submerged water jets [Webb, 1995].*

Danfoss IGBT Power Module 4

In this chapter a Danfoss IBGT power module is subject for investigation. The IGBT power module is a power inverter and consists of insulated gate bipolar transistors (IGBTs) and diodes. The IBGT power module is the subject for cooling in this project. The following sections are included:

4.1 Applications of IGBT Power Module

The IGBT power module is a half bridge module, and is used in electric and hybrid automobiles, e.g. a Toyota Prius. Three IGBT power modules are combined to form one inverter for a hybrid automobile, where it is necessary to convert DC from the battery to 3-phased AC used in the electric motors, and visa versa. In the Toyota Prius the electric motor is a 650 V (maximum) permanent magnet AC synchronous motor with a maximum power output of 60 kW [Toyota Motor Sales]. The IGBT power module is shown in figure 4.1.

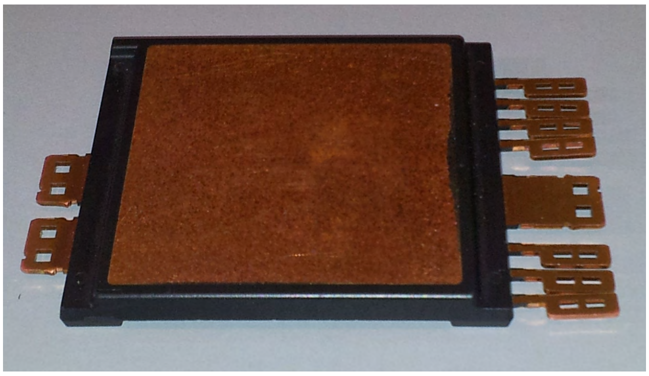

Figure 4.1: *Danfoss IGBT Half bridge Module.*

4.2 Characteristics of IGBT Power Module

The IGBT power module consists of six IGBTs and six diodes, as seen in figure 4.2 (a). Various operation parameters of the IGBT power module are listed in table 4.1.

Parameter	Value
Junction temperature, max.	175°C
Collector-to-emitter voltage, max.	650 V
Collector-to-emitter on-stage voltage, max.	2.2 V
Gate-to-emitter voltage, max.	$\pm$ 20 V
Gate-to-emitter threshold voltage, max.	6.5 V
Nominal IGBT and diode current	600 A
Total power dissipation, max.	2155 W
Weight	55 g

Table 4.1: *IGBT power module parameters [Stroebel, 2012].*

During normal operation the IGBTs dissipates in the vicinity of 100 W heat each, and the diodes around 50 W. This adds up to around 900 W which needs to be removed from the IGBT power module in order to extend the lifetime of the IGBT power module [Olesen, 2012]. The combined area of the diodes and IGBTs is 8.1 cm^2, and with an assumed heat dissipation of 900 W this gives a heat flux of 111.1 $^{W}/_{cm^2}$. The actual heat loss under operation depends on the voltage drop over the switch, and the current, which is determined by the phase and the engine load. To this the switching loss also needs to be added. As a general rule of thumb the heat loss from the inverter is 5 % of the engine power [Holst, 2012]. The electric motor in a Toyota Prius has a power output of 60 kW, and with three IGBT power modules, this general rule gives a heat loss of 1 kW for each IGBT power module.

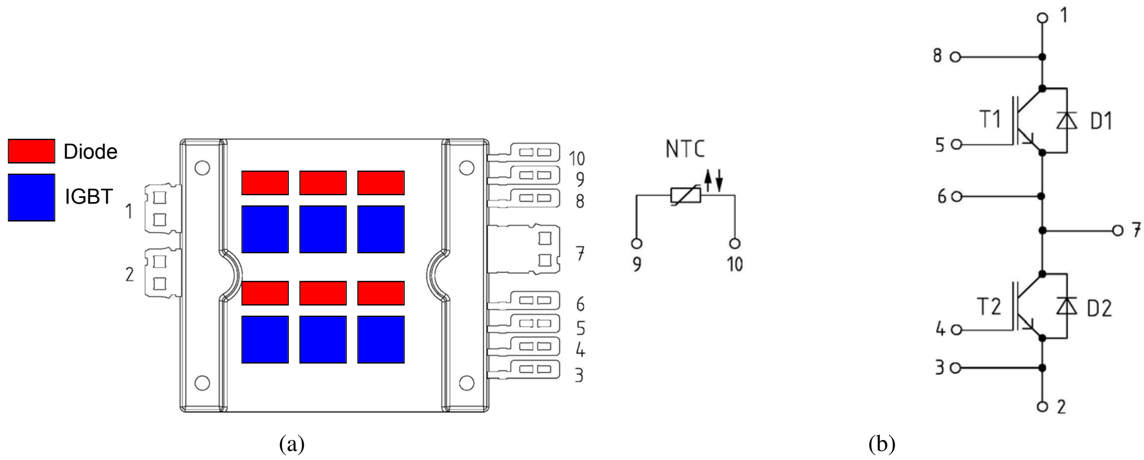

Figure 4.2: *Figure (a) showing schematic of the the IGBT power module and (b) the connections to transistor and diode [Stroebel, 2012].*

The IGBT power module area is 85x57 mm^2 and approximately 6 mm high. The area to be cooled is 50 x 50 mm. In figure 4.2 (b) an electric diagram is shown, corresponding to the pin number in figure 4.2 (a). Pin 9 and 10 connects a NTC thermistor for temperature measurements. Figure 4.2 (b) only shows two transistors and diodes, but this is due to parallel operation of three transistors and diodes.

Normal operation is not simulated due to high currents. Normally the gate receives a PWM signal with a certain duty cycle. The convenient way to dissipate power in the IGBT power module is to apply DC voltage to the collectors, which is from pin 1-2, while also applying the threshold voltage between the gate and emitter, which is pin 5-6 and 3-4. Applying the threshold voltage between the gate and emitter in this way, the power is only dissipated in the transistor, as it then acts as a variable resistor, and not the diode.

Cooling of the IGBT power module is important since a higher junction temperature gives an increase in failure time. This is due to the thermal expansion of the materials used in the IGBT power module. This leads to a restriction in temperature difference between inlet and outlet water in the cooling device.

In figure 4.3 a picture of an open IGBT power module is shown, before epoxy is applied, and the final cutting is made. The aluminium bond wire connecting the chips to the copper board is here visible.

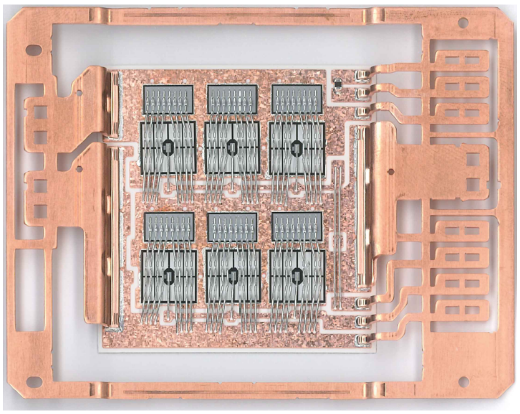

Figure 4.3: *Visualization of IGBTs and diodes [Olesen, 2012].*

In figure 4.4 the thermal coefficients of expansion for the different materials in the IGBT power module are shown. A non-uniform temperature distribution can cause problems. For instance, the thermal coefficient of expansion for the aluminium wire and chip are 24 ppm/K and 3 ppm/K, respectively [Danfoss, 2012]. A non-uniform temperature distribution with large local temperature gradients therefore increases the risk of various crack formation in the materials, or having a lifted bond wire. This results in failure.

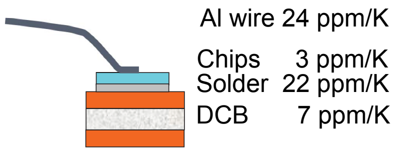

Figure 4.4: *Mismatch of thermal expansion coefficient in IGBT power module [Danfoss, 2012].*

As stated in the introduction, an IGBT power module performs better at lower temperature. In figure 1.2 on page 2 the output characteristics of the IGBT power module is shown for different junction temperatures. The figure shows that lower junction temperature yields better performance. In the introduction it is stated, that the failure rate increase with increasing temperature, so low junction temperature is preferred from two sides.

The discussion in this chapter leads to some desired design considerations of the cooling application:

1. Uniform temperature distribution in IGBT power module for uniform thermal expansion.
2. Low junction temperature in order to enhance performance and lifetime.
3. Low system operation cost of cooling design due to automotive applications.

Design of Cold Plates 5

Various design proposals are presented in this chapter together with various considerations about manifold and specific design features. The chapter consists of the following sections:

In figure 5.1 the various designs presented and discussed in this chapter are shown. Due to manufacturing constrains only two designs are manufactured. The staggered fin design requires a high work load for the department's workshop due the complex milling. The mini channel design is simple, but also known to have high temperature gradient in the flow direction. The multijet design and hybrid design are expected to have a good temperature uniformity and high h-values, and are thus chosen to be manufactured.

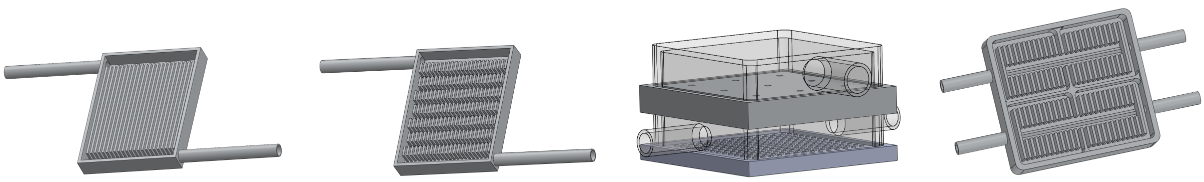

(a) *Mini channels.* (b) *Staggered fins.* (c) *Multijet.* (d) *Hybrid.*

Figure 5.1: *Names of the different designs presented.*

5.1 Design Criteria

Below are the design criteria listed in order to accomplish the problem statement of cooling the Danfoss IGBT power module. The criteria are listed by ranking of importance:

1. Cooling on hot spots in order to ensure uniform temperature distribution.
2. Low thermal resistance in the cold plate in order to have low junction temperature.
3. Low pressure loss and low flow rate for low system operation cost.

In order to accomplish these criteria a material with low thermal resistance is preferred as a high thermal resistance leads to a high junction temperature (discussed in appendix B). Aluminium, which has a relative high conductivity of 236.1 $W/m\,K$, is chosen as the material the cold plates are made of. This is also due to the fact that it is easier for the workshop to manufacture the designs in aluminium, than for instance copper. It is also taken into consideration that the material cost for aluminium is lower than for copper.

Stagnating flow in areas of local hot spots are not preferred, as this contributes to a local low h-value, and thus non uniformity. If a jet is directed towards a local hot spot the stagnation point must therefore be destroyed by a geometric feature. A high surface area is also preferred in order to enhance the heat transfer, as stated in equation (3.2).

A relative low turbulence in the flow is preferred due to preferably long lifetime and thus low erosion rate. However, high turbulence also gives a higher heat transfer and it thus becomes a trade-off between long life time of the cold plate, or high heat transfer abilities.

The cooling design is, due to the departments workshop, manufactured by milling, and thus the design consists of multiple pieces. For convenience water is used as coolant.

From these design considerations mini channels could yield good results due to high surface area. In section 3.4 mini channels are investigated, and a temperature increase in the direction of the flow occur. This may be minimized using a high flow rate, and hence a low temperature increase could be avoided. An advantage using mini channels is the large applicability to any high heat transfer problem, and thus production cost is likely to be minimized. A disadvantage of the high surface area is a relatively large pressure loss.

Jet impingement is investigated in section 3.5, and good local heat transfer is possible. Thus jet impingement is applicable to a customized design towards a specific heat transfer problem. Due to the good local heat transfer, multiple jets are advantageous for more uniform temperature distribution. An advantage is a relatively low pressure loss.

From the above discussion a combination of mini channels and jet impingement seems advantageous, if the disadvantages could be minimized.

5.2 Mini Channel Design

The first design presented is a mini channel design. To ensure an even flow distribution to the mini channels a manifold has to be designed. Two manifold designs are under consideration, a U-shape and a Z-shape. Schematics of these manifold types are shown in figure 5.2.

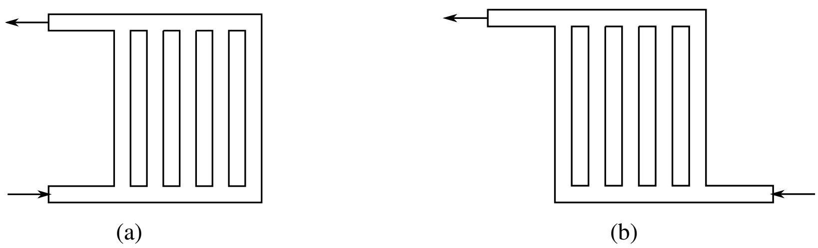

Figure 5.2: *Schematic showing (a) the U-shaped design and (b) the Z-shaped design.*

Based on Idelchik [1996] it is in general recommended to have a U-shaped manifold if the pressure drop over the manifold is small compared to the pressure drop over the channels. If the pressure drop over the manifold are large compared to the pressure drop over the channels, a Z-shape is recommended. The advantage of having a U-shaped manifold is that it is more practical with regards to fitting the tubes in the system.

The mini channel design idea includes 24 channels spanning a total of 47 *mm*, which gives a channel width of 1 *mm*, a length of 50 *mm*, and a height of 6 *mm*. The wetted surface area is 0.01672 m^2. The width and height of the channels are constrained by the department's workshop, otherwise smaller dimensions are interesting due to higher surface area and potentially higher convective heat transfer coefficient.

The design is drawn in SolidWorks and shown in figure 5.3, where additional dimensions are shown.

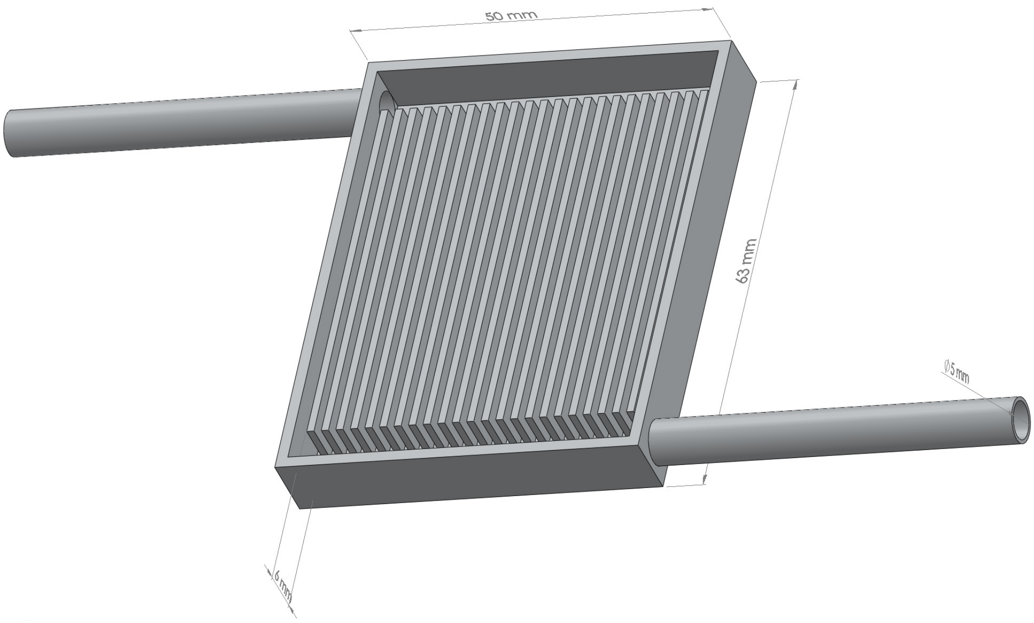

Figure 5.3: *Mini channel design.*

It is chosen to a have a bypass of 2 *mm* above the fins, as a bypass should improve the heat transfer, while also giving a lower pressure loss over the cold plate [Danfoss, 2012]. The bypass is shown in figure 5.4.

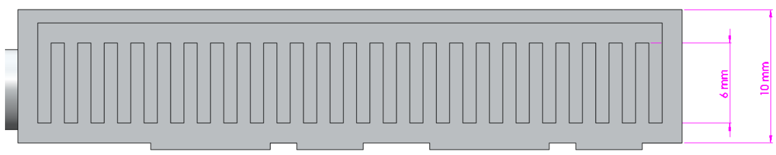

Figure 5.4: *Close up on mini channel design which shows the bypass.*

This design is relatively easy to manufacture, but due to the expected lack of temperature uniformity over the cold plate, this design is not chosen to be manufactured.

5.3 Staggered Fin Design

An altered version of the mini channel design is here considered. In order to enhance mixing and thereby heat transfer, the boundary layer in the channels needs to be disturbed. From section 3.2 it is known that the convective heat transfer coefficient is higher in developing flow than in developed flow. Ensuring more areas of developing flow may therefore enhance the heat transfer. This is here done by reducing the length of the channels, and then to stagger the next set of channels. Figure 5.5 shows the development of the boundary layer and wake region for the flow along a fin, seen from above. It is seen that there is a repeated growth and wake destruction of the boundary layer. As this principle applies to all the fins in the design, there is a good potential for high heat transfer with this design. It is in this design chosen to have rectangular fins, however for further work a parametric study of the optimum shape of the fins could be interesting.

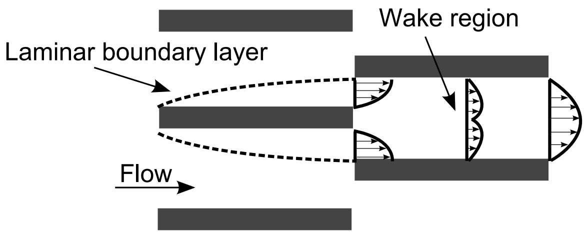

Figure 5.5: *Boundary layer and wake region for a offset fin, based on Kakac et al. [1987].*

The channel height and width are not altered from the design shown in section 5.2 due to manufacturing constrains, and the manifold design is not altered. In figure 5.6 the staggered fin design is shown. This design is from a manufacturing point of view difficult to produce by milling. Thus it is chosen not to be manufactured, but CFD is applied in chapter 6 to evaluate the cooling performance. In the simulation both a design with and without a 2 mm bypass is investigated. The surface area for the geometry with bypass is 0.01574 m^2, whereas it without bypass is 0.01711 m^2.

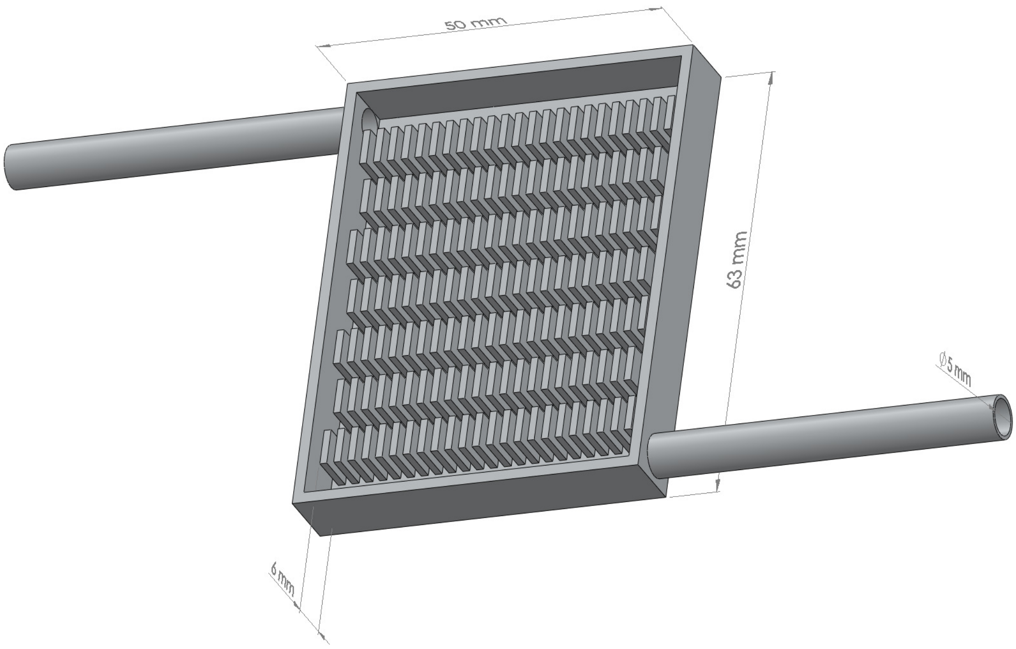

Figure 5.6: *Staggered fin design.*

5.4 Multijet Impingement Design

With reference to section 3.5 multijet impingement on a plate is interesting due to local high convective heat transfer. With multiple jets the high heat transfer is directed towards the areas of the IGBTs and diodes. Based on Barrau [2011] a jet velocity of 4 m/s is reasonable, hence this design is developed to have a velocity of approximately 4 m/s in the nine inlets. With a maximum Reynolds number of 10,000 at a water temperature of 30 $°C$ an inlet diameter of 2 mm is reasonable due to the following calculation:

$$D = \frac{Re \cdot \mu}{\rho \cdot v} = \frac{10,000 \cdot 0.0007977}{995.1 \cdot 4} = 0.002\ m \tag{5.1}$$

This gives a mass flow rate of:

$$\dot{m} = v \cdot A \cdot \rho = 4\ \frac{m}{s} \cdot 9 \cdot \pi \cdot (0.001\ m)^2 \cdot 995.1\ \frac{kg}{m^3} = 0.1125\ \frac{kg}{s} \tag{5.2}$$

In section 3.5 a nozzle-to-target spacing of five times the inlet diameter is found beneficial, which yields a 10 mm jet height, see figure 5.7 (a). In section 3.5 a jet-to-jet spacing of 8 times the inlet diameter was found beneficial, which yields a jet-to-jet spacing of 16 mm for this design, see figure 5.7 (b).

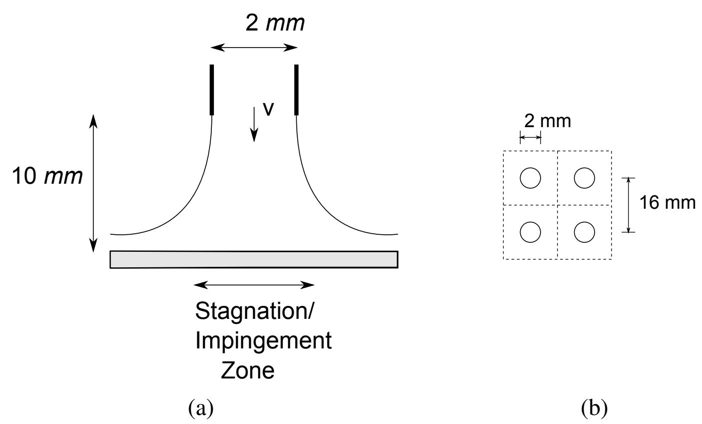

Figure 5.7: *(a) Jet diameter and height (b) jet-to-jet spacing.*

Due to the problem of stagnation points in the jet impinging zones, disturbed flow on the target plate is advantageous. Thus a target plate with 1x1 mm squares with a height of 0.5 mm is made, based on the discussion in chapter 3.3. These squares are shown in figure 5.8. This gives a surface area of heat transfer of 0.0025080 m^2. For further work, the target plate geometry could be studied by e.g. optimization algorithms.

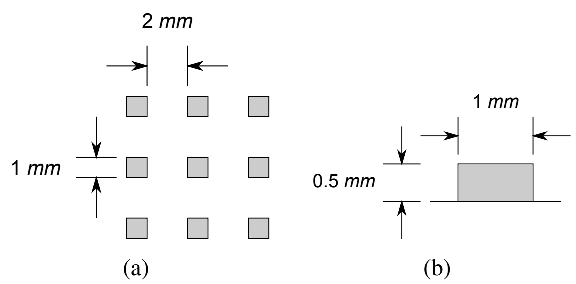

Figure 5.8: *(a) Target plate squares seen from above and (b) square seen from the side.*

For practical reasons a manifold design with one inlet is considered. Liu et al. [2008] investigates a manifold for jet impingement where the main concept is a distributer box on top of the perforated plate where there is one inlet in the distributer box. The velocity distribution for this is shown in figure 5.9. This concept is also used in this design to help give an even flow distribution to the nine jet inlets. In figure 5.9 the inlet is located in a corner, but this is for practical reasons not easy to implement.

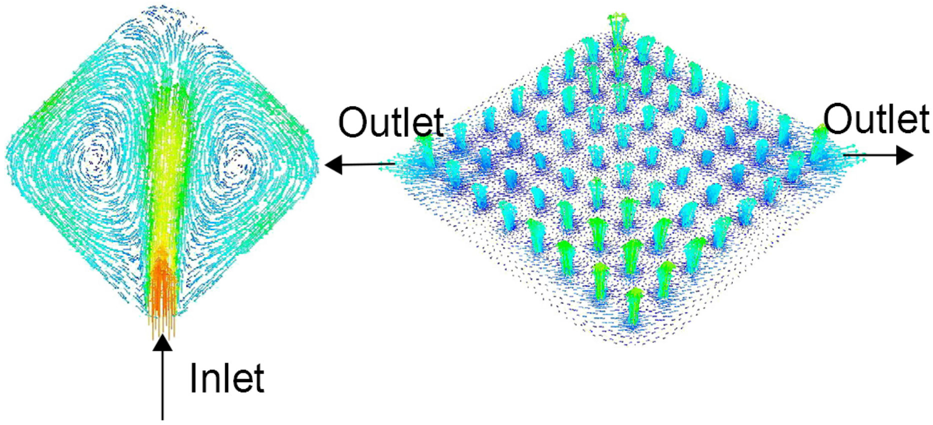

Figure 5.9: *Inlet manifold suggested by Liu et al. [2008] with outlets perpendicular to the inlet.*

In figure 5.10 the multijet design is shown together with its dimensions. The two outlets are placed normal to the inlet, which is found beneficial by Liu et al. [2008]. It is ensured that the combined outlet area is larger than the inlet area to avoid unnecessary pressure losses. This multijet design is chosen to be manufactured due to expectations on high h-values and good temperature uniformity.

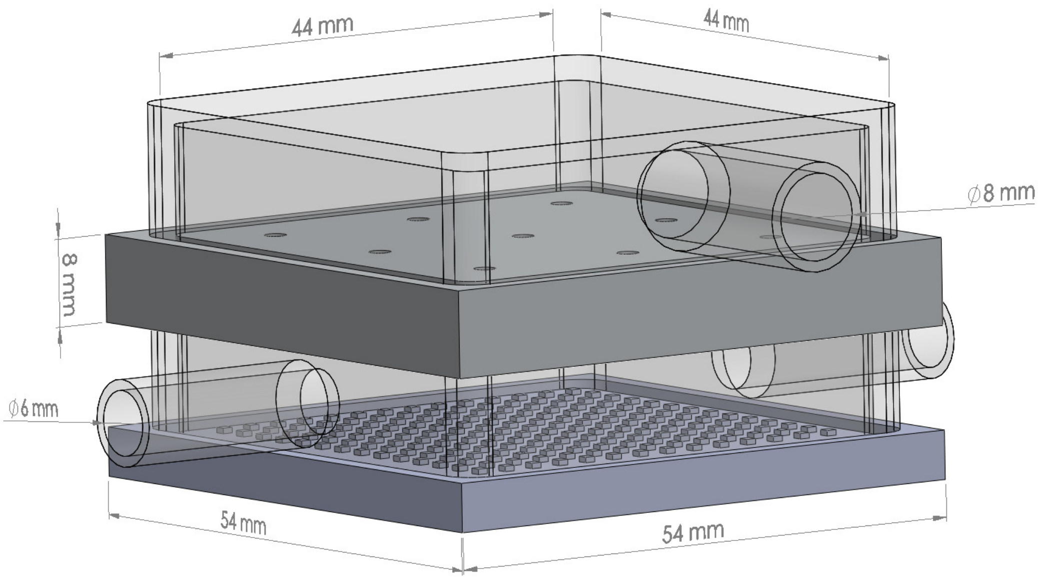

Figure 5.10: *Design with multiple jets and rough target plate.*

5.5 Hybrid between Jet Impingement and Mini Channels

A hybrid solution of mini channels combined with jet impingement shows good results, as stated by Sung and Mudawar [2008] and Barrau [2011]. A sketch of this design is shown in figure 5.11. One of the key findings is a high degree of surface temperature uniformity, as the temperature gradient along the flow in the micro channels are small. Besides the high temperature uniformity the hybrid design also gives a low surface temperature with a relative low jet velocity and channel height [Sung and Mudawar, 2008].

In addition to the features seen in this sketch, a triangular prism is added in the bottom of the the design where the target zones of the jets are located. This is discussed in section 5.5.1.

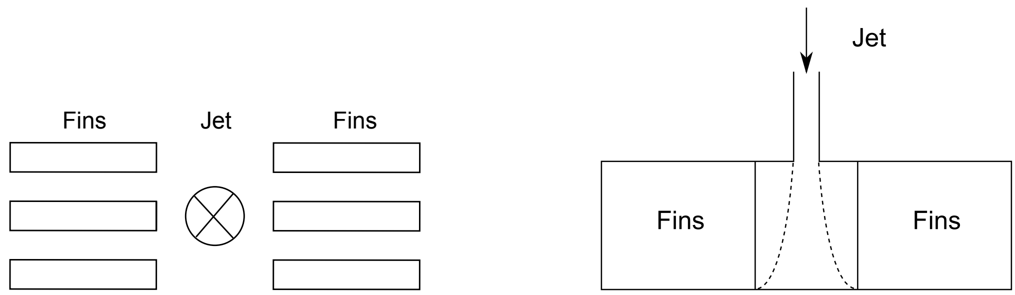

(a) *Hybrid cooling scheme seen from the top.* (b) *Hybrid cooling scheme seen from the side.*

Figure 5.11: *Sketch of hybrid cooling scheme based on Sung and Mudawar [2008].*

The inlet manifold from the multijet design is also used in this design. Based on section 3.5, the optimum nozzle-to-target ratio is five. The fin height is constrained to 6 mm, which is the manufacturing constrain from the department's workshop, when milling 1 mm channels. The height of the fins corresponds to the jet height, and thus the jet diameter is 1.2 mm. The total wetted surface area of the geometry is 0.01246 m^2. Due to the location of the IGBTs and diodes in the Danfoss IGBT power module, one jet on each of the six IGBTs is chosen. Designing for a jet velocity of 4 m/s as in section 5.4, the Reynolds number in each of the six inlets is:

$$Re = \frac{D_h \cdot v \cdot \rho}{\mu} \approx 6000 \tag{5.3}$$

In figure 5.12 the bottom chamber of the hybrid design is shown along with dimensions.

In the impinging zone of the jet, a stagnation point of the jet may occur with resulting low heat transfer. In order to try to avoid this, the design is developed with a triangular prism in the jet impinging zone. The design has four outlets, one for each division of the bottom chamber. The division is made to give an even flow distribution inside the chamber, and the division between the left and right side of the chamber in figure 5.12 is made to avoid the outlet water from the mini channels to interact with each other, as this would induce stagnation zones.

In figure 5.13 the inlet manifold for the hybrid design is shown. This part fits on top of the part shown in figure 5.12. The perforated inlet plate is made transparent to show the six inlets. There is cut a groove on the top and bottom of the perforated plate to make space for O-rings, which ensures a tight seal so the water does not leak during testing.

It is chosen to manufacture this design because of high expectations to the convective heat transfer coefficients, and a good temperature distribution.

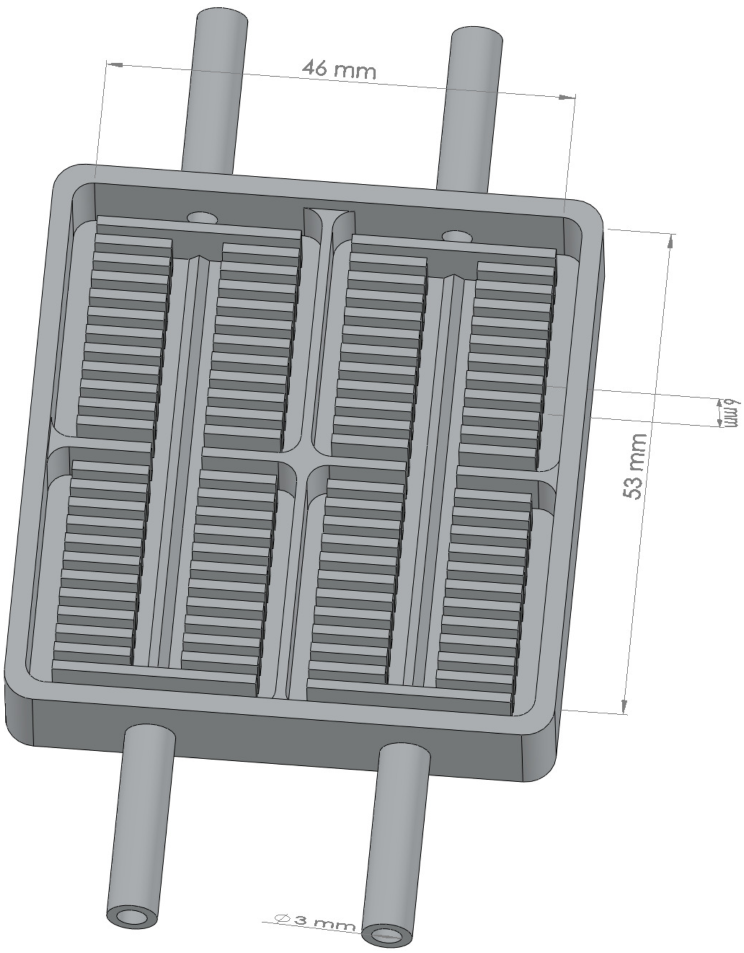

Figure 5.12: *Hybrid design with both jet impingement and mini channels.*

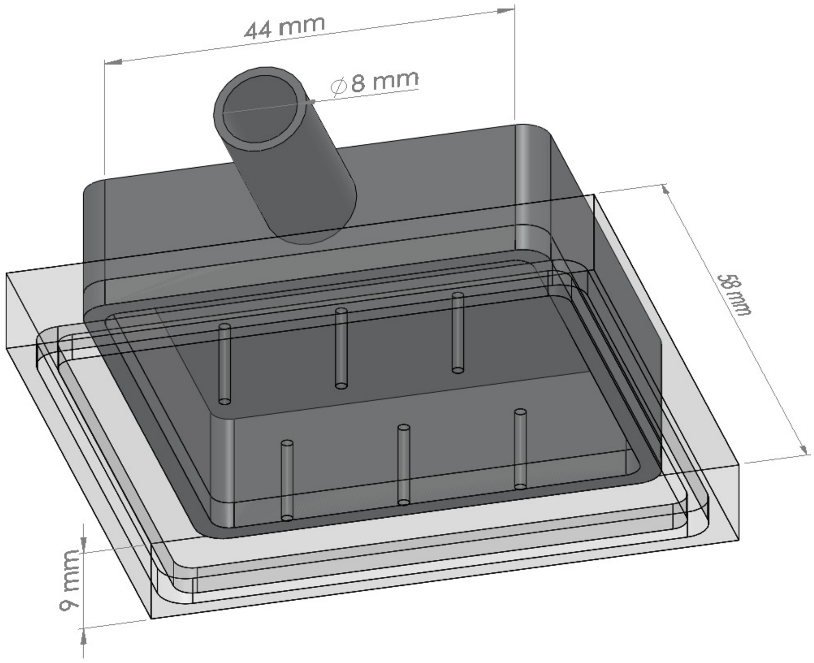

Figure 5.13: *Inlet manifold for hybrid design.*

5.5.1 Discussion of Triangular Prism

To make a concept study of the effect of having a triangular prism in the jet impingement zone, 2D CFD simulations are made. The domain is shown in figure 5.14.

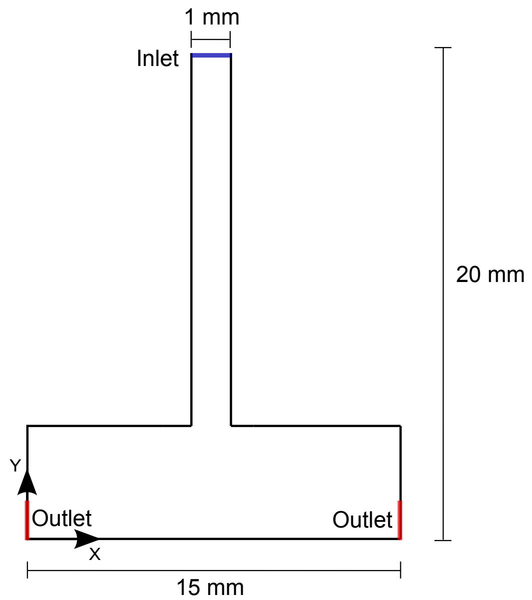

Figure 5.14: *Domain used for concept study.*

The height of the triangular prism is varied with a height of 0.5 *mm* and 1 *mm* in the impingement zone. In addition to this, the impingement zone is also investigated without a triangular prism. The velocity at the inlet is 1.4 m/s. The combined results from the CFD simulations is shown in figure 5.15.

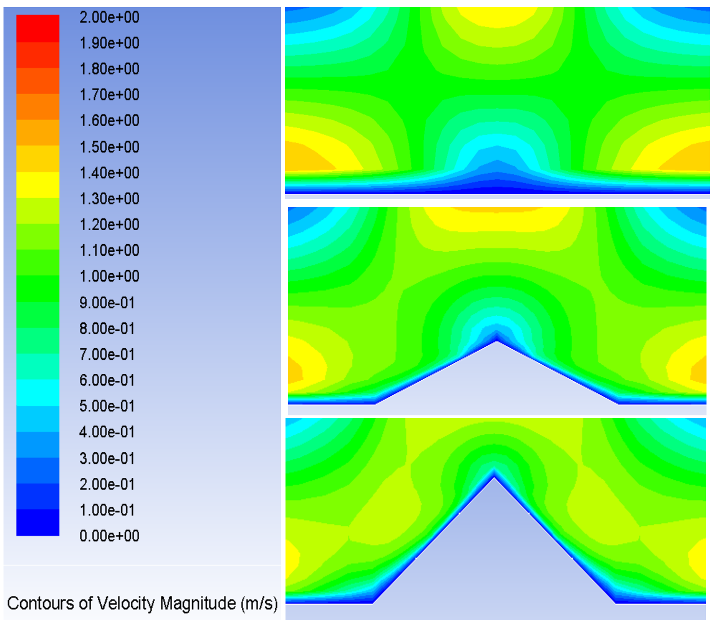

Figure 5.15: *Zoom on velocity distribution around triangular prism in impingement zone in 2D CFD simulations. The top picture does not have a triangular prism, while the two bottom pictures has a height of the 0.5 mm and 1 mm for the triangular prism, respectively.*

In the top picture in this figure the stagnation zone is largest compared to the two other pictures, hence it is seen that having a triangular prism gives a smaller stagnation zone. This is an advantage when high heat transfer is desired. From figure 5.15 it is seen that different effects occur when the height of the triangular prism is varied. In the bottom picture in figure 5.15 the height of the triangular prism is 1 *mm*, which effectively removes the stagnation zone directly under the jet. However, at the side of the triangular prism larger stagnation zones occurs compared to the triangular prism with a height of 0.5 *mm*. In the middle picture a smaller stagnation zone occur on the side of the triangular prism, but then a bigger stagnation zone occurs on top of the triangular prism.

From the simulations with the triangular prism it is concluded, that it is most advantageous to have a triangular prism with a height of 1 *mm* to minimize the stagnation zone. However, it is assumed that the jet hits the triangular prism directly at its top. Another thing to consider is that a larger height of the triangular prism adds to the material and manufacturing costs, and that this material adds to the thermal resistance from the junction of the IGBTs and up through the base of the cold plate.

To investigate the influence of more material on the heat transfer, a contour plot of the temperature distribution around the same two triangular prism heights is shown in figure 5.16. With a depth of 1 *mm* for the 2D simulation and a heat flux of $3 \cdot 10^6\ W/m^2$ the heat input is 3 W for these simulations. The water temperature in these simulations is 300 K.

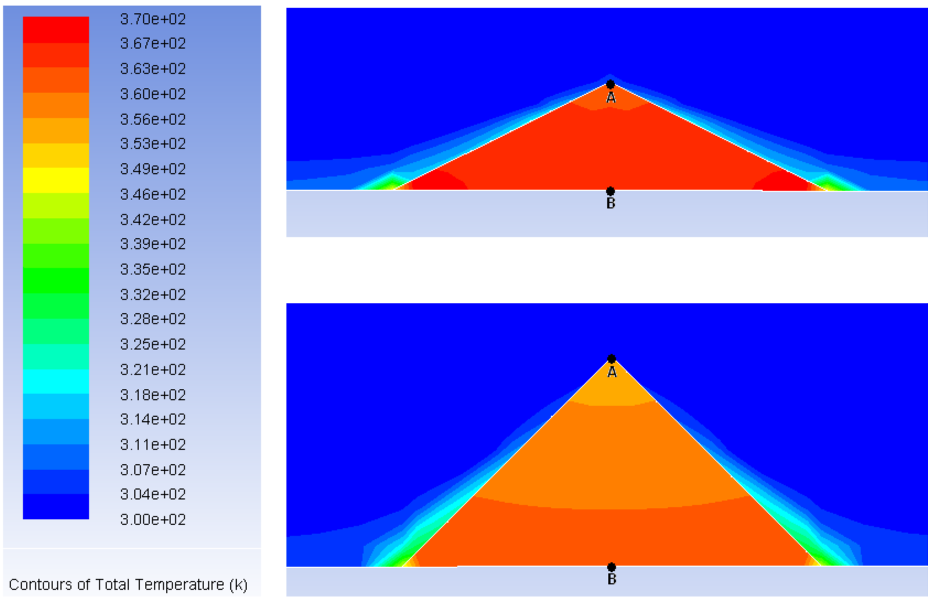

Figure 5.16: *Temperature distribution around triangular prism at two different heights.*

The temperatures in point B is 361.7 K for the 1 *mm* prism, while the temperature in point B for the 0.5 *mm* prism is 365.3 K. From this it is concluded that the smaller stagnation zone yields a better heat transfer, even though the thermal resistance for the prism itself is higher. This might also be due to an increase in the heat transfer area. The temperature in the water directly above the prism (point A in figure 5.16) is 301.3 K for the 1 *mm* prism, while the temperature in point A for the 0.5 *mm* prism is 305.4 K. Without a prism the same temperature is 307.4 K for this point. Again this shows that a smaller stagnation zone gives a higher heat transfer. This concept study shows that it is advantageous to use a triangular prism on the hybrid design, even though more material is added to the design.

CFD Simulations of Cold Plate Designs

6

In this chapter CFD simulations of the different designs are documented, and the results are presented and compared. All the simulations are made in ANSYS FLUENT. The procedure for making a flow simulation follows the method outlined in appendix C. The chapter consists of the following sections:

6.1 Convergence Criteria and Input Conditions

The following criteria for convergence check are made for all designs, based on ERCOFTAC [2000] and Versteeg and Malalasekera [2007]:

- Grid independency.
- Mass flow balance < 0.1 % of mass flow.
- Energy balance < 0.5 % of input.
- Check maximum and minimum parameters in whole domain to be meaningful, e.g. no temperature lower than input temperature.
- Output temperature should be as expected from equation (3.1).
- Residuals are asymptotic.
- The pressure loss increase should be a second order function of the fluid velocity, based on equation (3.17).

The chosen level of accuracy for the energy and mass balances is set to a reasonable level compared to the level of energy balance in an experiment.

The input conditions for all simulations are shown in table 6.1. The k-ω SST turbulence model is used due to good predictions of the impinging jet heat transfer coefficient, based on Zuckerman and Lior [2006]. Water at 30 $^{\circ}C$ is used for all simulations unless otherwise is stated. The heat flux specified corresponds to a heat input of 300 W for half the geometry, and 600 W for the full geometry. The heat flux is only specified on the IGBTs, as this corresponds to the experimental conditions. At normal operation conditions, the heat input would be from both IGBTs and diodes. The solution method used for the pressure-velocity coupling is SIMPLE, and a second or third order spatial discretization schemes are used, according to ERCOFTAC [2000]. The use of the SIMPLE algorithm is based on the assumption of steady state in the simulations.

Models	Energy and k-ω SST turbulence
Materials and properties	Water @ 30 $°C$
	Aluminium @ 30 $°C$
Boundary conditions	Specified for individual designs
Heat flux	1,111,111.11 W/m^2
Solution method	SIMPLE with second or third order spatial discretization scheme

Table 6.1: *Boundary conditions for CFD.*

As inlet boundary a mass-flow-inlet is used. The turbulence intensity and the hydraulic diameter of the inlet is specified here. For the outlet boundary a pressure-outlet is used. Here the backflow turbulence intensity and the hydraulic diameter are specified. The gauge pressure for the outlet is set to be 0. All simulations are chosen to have comparable Reynolds numbers ranging from 2000-10,000, and in the inlet tubes. For the mini channel and staggered fins designs it is chosen to also do a simulation at a Reynolds number of 20,000.

6.2 Mini Channel Design

In this section the CFD simulations of the mini channel design are presented. Also a study comparing hexahedral and tetrahedral cells for the same domain is carried out.

6.2.1 Mesh

The mesh for this design is made in ANSYS GAMBIT and consists of hexahedral cells. The domain is based on the geometry in figure 5.3, and the size of the mesh, after mesh independency, is approximately 1,300,000 cells. In figure 6.1 (a) it is shown how the the boundary layer is resolved by a refined mesh close to the fins inside a water channel. This is done to ensure a reasonable y^+ value when resolving the boundary layer. From the discussion in appendix C a y^+ under 5 is needed, when using the enhanced wall treatment. y^+ is calculated by [ANSYS, Inc, 2009]:

$$y^+ = \frac{\Delta y_P}{\mu} \cdot \sqrt{\frac{\tau_w}{\rho}} \qquad [-] \tag{6.1}$$

The wall shear stress is calculated by [ANSYS, Inc, 2009]:

$$\tau_w = f \cdot \rho \frac{v^2}{2} \qquad [Pa] \tag{6.2}$$

The inlet and outlet tubes are also made with a boundary layer mesh, and this is shown as the black ring in the figure 6.1 (b), as the cells are very small here. The outlet tube is made in a similar way.

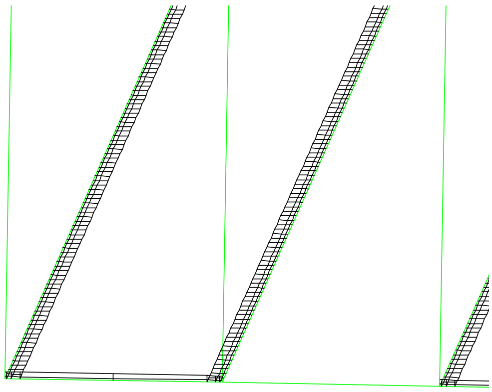

(a)

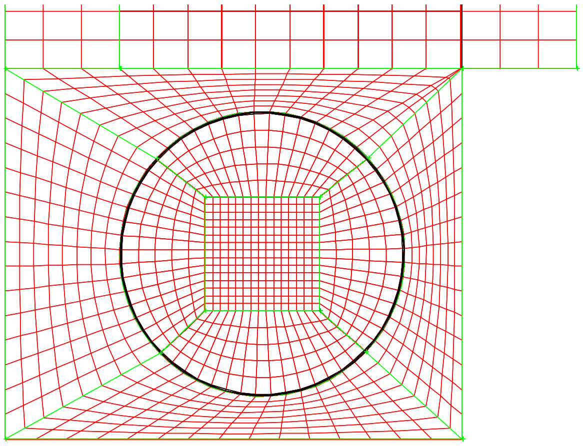

(b)

Figure 6.1: *3D picture of boundary layer in a mini channel (left), and 2D picture of mesh in inlet tube (right).*

Under the mini channels there is an additional thickness of the base plate of 2 mm. On the base plate the IGBTs are modeled as a separate wall to be used for the boundary condition for the heat input. A key assumption for this simulation is the use of thin surfaces around the domain, except for the base plate.

A mesh independency check is carried out to examine whether the mesh is sufficiently discretized. The original mesh is refined using the mesh adaption option in ANSYS FLUENT, where the velocity gradient is the parameter used for refinement. For the grid independency simulations the second order spatial discretization scheme is used. The results of the refinement are presented in table 6.2, where the overall mass and energy balances are checked, along with h-value, surface temperature, and pressure difference from the inlet to the outlet.

Mesh size	**Coarse (1,077,060)**	**Medium (1,282,405)**	**Fine (2,014,192)**
Pressure difference [Pa]	2335	2528	2509
h-value [$W/m^2\,K$]	1,567	1,533	1,587
T_s [K]	328.4	328.9	328.1
Overall mass rate balance [kg/s] (%)	-2.52e-5 (0.08)	1.5e-5 (0.05)	8.9e-6 (0.03)
Overall energy balance [W] (%)	-3.9 (0.65)	0.2 (0.03)	0.3 (0.05)

Table 6.2: *h-value, surface temperature, and pressure difference for mesh independency check for the mini channel design.*

Table 6.2 shows fluctuations in the pressure difference, h-values, and the surface temperature. This might be due to the convergence of the residuals, which is shown in figure 6.2 (b). There seems to be a problem with the overall energy balance for the coarse mesh. Due to the fact that the changes in the results are quite small, and the mass and energy balances from medium to fine mesh are comparable, the medium mesh size is chosen as the grid independent mesh. Different contour plots have been examined in order to see if the results are meaningful.

Six different mass flows are simulated. For the outlet boundary a pressure outlet is used, and in table 6.3 the boundary conditions for the six different setups are shown.

In figure 6.2 (a) the y^+ along a mini channel is shown in a height of 2 mm. This is for the simulation with a Reynolds number of 8000 in the inlet tube. The values are considered as being in a reasonable range, as the

Reynolds number [-]	**2000**	**4000**	**6000**	**8000**	**10,000**	**20,000**
Inlet mass flow rate [kg/s]	0.006	0.013	0.019	0.025	0.031	0.063
Inlet turbulence intensity [%]	6.2	5.7	5.4	5.2	5.1	4.6
Outlet turbulence intensity [%]	6.2	5.7	5.4	5.2	5.1	4.6

Table 6.3: *Mass flow rate and turbulence intensities for boundary conditions in mini channel design.*

maximum value for y^+ is 1.5. The low values of y^+ are as expected from the design considerations for the mesh. Figure 6.2 (b) shows the scaled residuals for the simulation, which shows an asymptotic tendency. The residuals do not settle at a specific value, and small fluctuations occur. It is however still assumed that the simulation is converged.

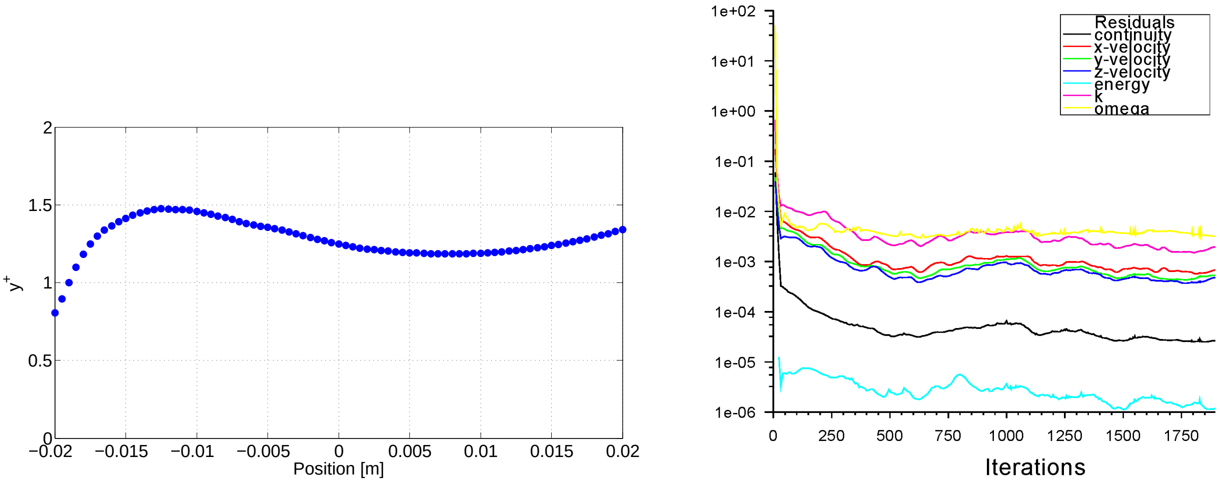

(a) (b)

Figure 6.2: *y^+ values along the fin wall in a height of 2 mm (a), and scaled residuals (b).*

6.2.2 Results

In table 6.4 the results from the simulations are shown. The Reynolds number is based on the flow in the inlet tube. It is seen that a higher Reynolds number yields a lower junction temperature. At the highest Reynolds number the pressure loss is relatively high, as expected due to equation (3.17).

Reynolds number	**2000**	**4000**	**6000**	**8000**	**10,000**	**20,000**
T_{max} $[K]$	438.8	400.5	384.9	377.0	366.7	354.9
T_o $[K]$	326.6	314.6	310.8	308.9	307.7	305.5
$T_{surface}$ $[K]$	378.4	351.0	339.7	334.8	328.9	320.5
h-value $[W/m^2\,K]$	561	859	1103	1249	1533	2218
ΔP $[Pa]$	130	452	954	1556	2528	9745
P_{pump} $[W]$	0.0008	0.006	0.018	0.039	0.079	0.613

Table 6.4: *Results from CFD simulation of mini channel design.*

The flow distribution to the different channels is not very uniform. This is shown in top of figure 6.3 where a contour plot of the velocity magnitude is shown. The inlet is in the bottom right corner, while the outlet is in the upper left corner. The velocity is highest in the last channels. The effect of having the bypass is shown in the bottom of figure 6.3 where the velocity magnitude at a cross section through all the fins in the middle of the cold plate is shown. The velocity of the flow is highest in the left hand side and above the fins. This maldistribution could indicate a too big bypass.

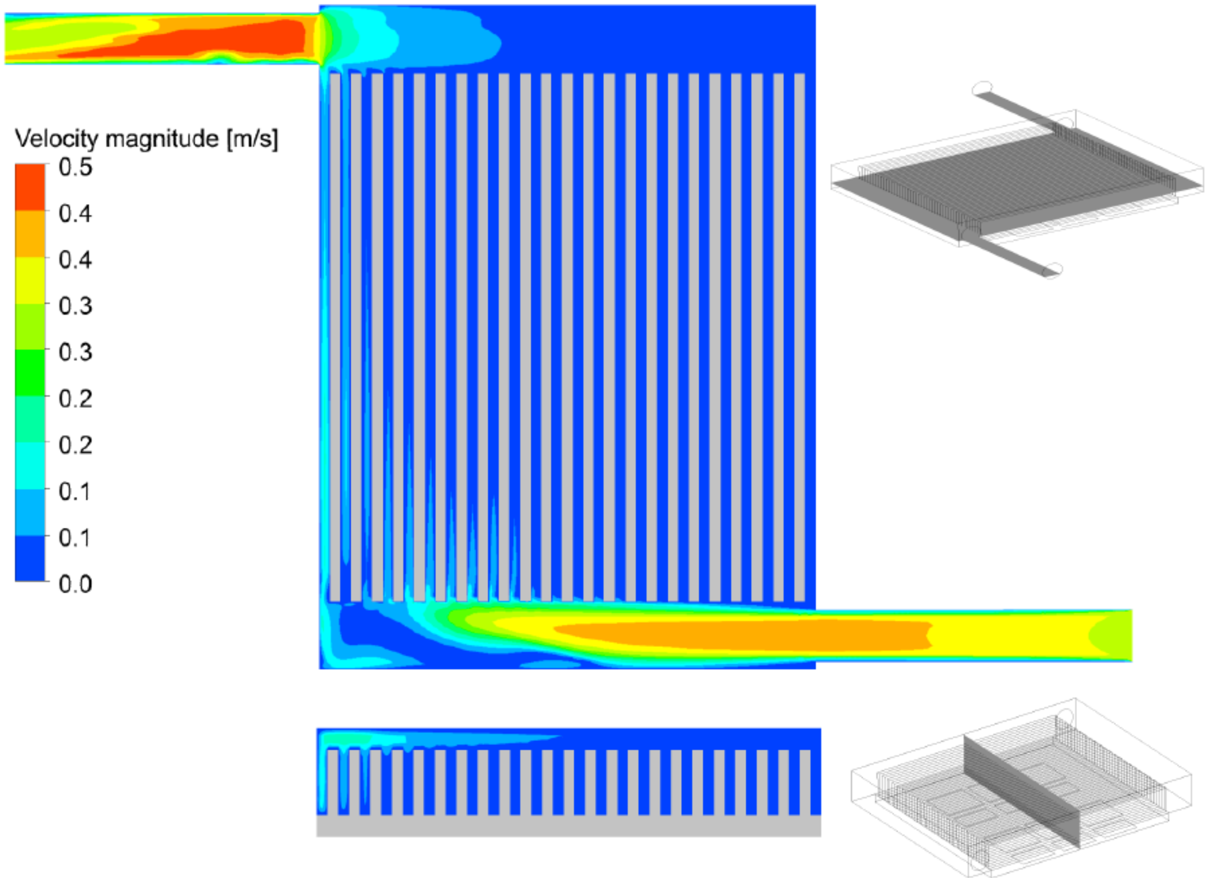

Figure 6.3: *Velocity magnitude in mini channels at a fin height of 2 mm, and in the middle of the cold plate.*

The maldistribution gives a quite non-uniform cooling, which is shown in figure 6.4. The temperature distribution becomes more uniform at higher Reynolds numbers, and the maximum temperature also gets lower.

The temperature uniformity is described as the ratio between the maximum temperature and the average temperature on the backside of the cold plate. This is shown in table 6.5. A low standard deviation indicates in this case a good uniformity, which is seen to be the case at higher Reynolds numbers. The sample standard deviation is defined as:

$$\sigma = \sqrt{\frac{1}{n-1}\sum_{i=1}^{n}(X_i - \bar{X})^2} \tag{6.3}$$

σ represents the averaged deviation from the mean. The standard deviation of the temperature on the backside of the cold plate is shown in table 6.5.

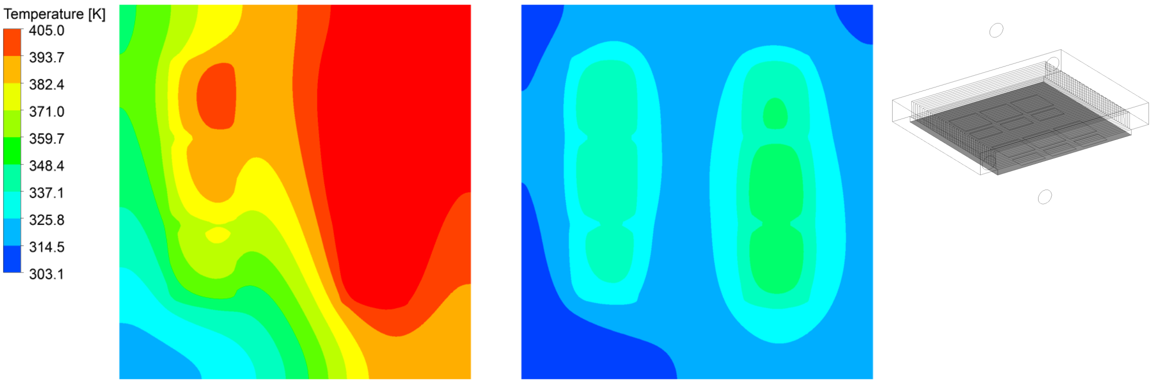

Figure 6.4: *Temperature distribution on backside of cold plate for Re=2000 (left) and for Re=20,000 (right).*

Reynolds number [-]	**2000**	**4000**	**6000**	**8000**	**10,000**	**20,000**
T_{mean} $[K]$	385.6	357.9	346.5	341.4	335.8	323.2
T_{max}/T_{mean} [-]	1.138	1.119	1.111	1.104	1.092	1.085
σ_{T_s} $[K]$	29.75	20.54	17.23	15.74	13.43	10.87

Table 6.5: *Ratio between max temperature and mean temperature on backside of cold plate.*

6.2.3 Case Study of Structured versus Unstructured Mesh

In this section a similar CFD simulation of the mini channel design is presented, but with the difference that the mesh is made with the ANSYS Meshing tool available in the ANSYS Workbench. This is made to determine if it is reasonable to make a mesh made of unstructured tetrahedral cells compared to the mesh made in ANSYS GAMBIT which consists of structured hexahedral cells. The advantage by doing this is, that the time spend on generating the mesh with the ANSYS Meshing tool is considerable smaller than the time spend on making the mesh in ANSYS GAMBIT. The geometry used in ANSYS Meshing is made using SolidWorks, seen in figure 5.3 on page 29. The original mesh generated in ANSYS Meshing is shown in figure 6.5. After the mesh independency check the size of this mesh is approximately 2.2 million cells. The mesh is made with an inflation layer consisting of four layers on all of the walls which are in contact with the water, and the height of the first cells corresponds to the height for the first cell in the boundary layer mesh in the ANSYS GAMBIT mesh. In figure 6.5 the gray mesh domain is the fins and the outer walls, and the dark green domain is the fluid zone.

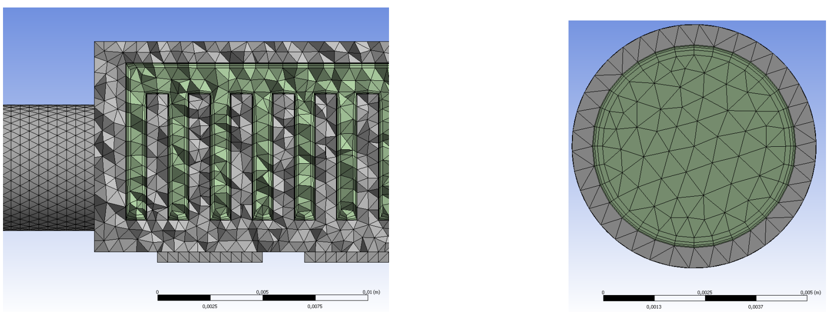

(a) (b)

Figure 6.5: *Mesh made in ANSYS Meshing. Cross sectional view through the fins (left), and mesh in inlet tube (right).*

The simulations is made with a third order discretization scheme, which is preferable for a tetrahedral mesh according to ERCOFTAC [2000]. The boundary conditions are a heat flux which is equivalent to 600 W, and a Reynolds number of 10,000 for the inlet tube. The difference between the simulations for the two kind of mesh types are seen in table 6.6.

Type of mesh	**ANSYS GAMBIT (hexahedral)**	**ANSYS Meshing (tetrahedral)**
Mass flow [kg/s]	0.03133	0.03133
h [$W/m^2\,K$]	1533	1782
T_o [K]	307.7	307.7
$T_{surface}$ [K]	328.9	325.7
Mass balance [kg/s] (%)	1.5e-5 (0.048)	4.3e-7 (0.0014)
Energy balance [W] (%)	0.22 (0.037)	-0.02 (0.003)
Pressure difference [Pa]	2528	3032
T_{max} [K]	366.7	371.6

Table 6.6: *Comparison of results between mesh made in ANSYS GAMBIT and mesh made with ANSYS Meshing tool.*

Table 6.6 shows that the results diverge from each other. The difference between the average surface temperature of the fins is for example 3.2 K. The reason for this deviation could for one be the difference between the geometry used, as the mesh in ANSYS GAMBIT is made with thin surfaces around the domain. This results in no heat transfer in the walls. In the unstructured tetrahedral mesh all of the walls have a thickness of 1 mm, while the 2 mm base plate is under the entire cold plate for this mesh, while the base plate is omitted under the manifold areas for the structured hexahedral mesh. ERCOFTAC [2000] states that a lack of precision is generally compromised when dealing with tetrahedral mesh. This geometric difference is bound to have an effect, but the main reason for the difference is considered to be the lack of precision.

The deviation between the results is a setback for the accuracy when using the tetrahedral mesh, but making the CFD simulations still give an idea of how the cold plate performs when the boundary conditions are changed. Also, this type of approach, when making the mesh, gives a relative quick way of comparing the different cold plates with each other, and especially a good opportunity in determining whether a bypass is an advantage or a disadvantage for the staggered fins design.

6.3 Staggered Fins Design

The mesh for this simulation is based on the SolidWorks drawing shown in figure 5.6 on page 30. The tetrahedral mesh is made with the ANSYS Meshing tool, and the size of the mesh is in the vicinity of 1.6 million cells. Again the boundary layer is made as an inflation with several layers very close to all the walls upon which the fluid is in contact with. The mesh is shown in figure 6.6. On the left hand side in this figure a cut is made from above and hence through all the fins. On the right hand side in this figure the mesh is seen as a sideways cut through the cold plate. Again the green domain is the fluid while the gray domain is the solid.

The discretization scheme used is third order (MUSCL), and the turbulence model used is $k-\omega$ SST. The results from the mesh independency check are shown in table 6.7. The results changes minimally when the two refinements are made, hence the coarse mesh is chosen to save computational time. The mesh is refined by using the ANSYS FLUENT mesh adaption, with the velocity gradient as parameter. The inputs for these

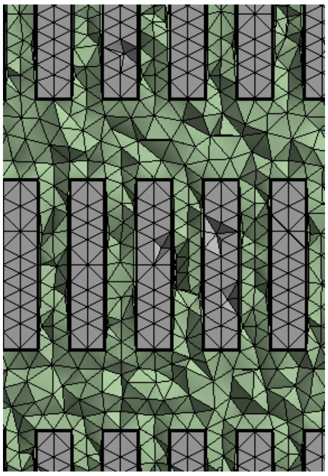

(a)

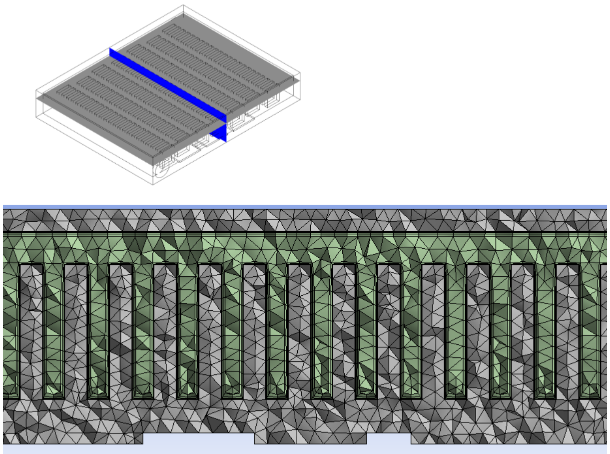

(b)

Figure 6.6: *Mesh of staggered fins design seen from above (left), and the mesh seen in a sideways cut (right).*

results are a heat input of 600 W, and a Reynolds number of 10,000 in the inlet tube.

Mesh size	**Coarse (1,557,372)**	**Medium (1,945,900)**	**Fine (2,391,716)**
h-value [$W/m^2\,K$]	2390	2394	2399
Pressure difference [Pa]	2984	3025	3027
T_s [K]	321.5	321.5	321.4
T_{max} [K]	371.8	372.0	371.7
Overall mass rate balance [kg/s] (%)	-4e-06 (0.013)	-2e-6 (0.006)	-5e-6 (0.016)
Overall energy balance [W] (%)	-0.47 (0.08)	0.46 (0.08)	-0.31 (0.05)

Table 6.7: *h-value, surface temperature, maximum temperature and pressure difference for mesh independency check for the staggered fins design.*

The different mass flows and turbulence intensities for these simulations with this design are shown in table 6.8.

Reynolds number [-]	**2000**	**4000**	**6000**	**8000**	**10,000**	**20,000**
Inlet mass flow rate [kg/s]	0.006	0.013	0.019	0.025	0.031	0.063
Inlet turbulence intensity [%]	6.2	5.7	5.4	5.2	5.1	4.6
Outlet turbulence intensity [%]	6.2	5.7	5.4	5.2	5.1	4.6

Table 6.8: *Mass flow rate and turbulence intensities for boundary conditions in staggered fins design.*

Figure 6.7 shows the scaled residuals for the simulation with the staggered fins with bypass (a) and without bypass (b). The figures show an asymptotic tendency. The residuals for figure 6.7 (b) do not settle at a specific value, and some fluctuations occur. However, both simulations are considered converged.

In table 6.9 the results from the simulations with this design are shown. All the simulations are made with a heat input of 600 W. At increasing mass flow the junction temperature drops, and the lowest junction temperature is 358.4 K. For this Reynolds number the pressure drop starts to be significant with a value of 11,513 Pa, as

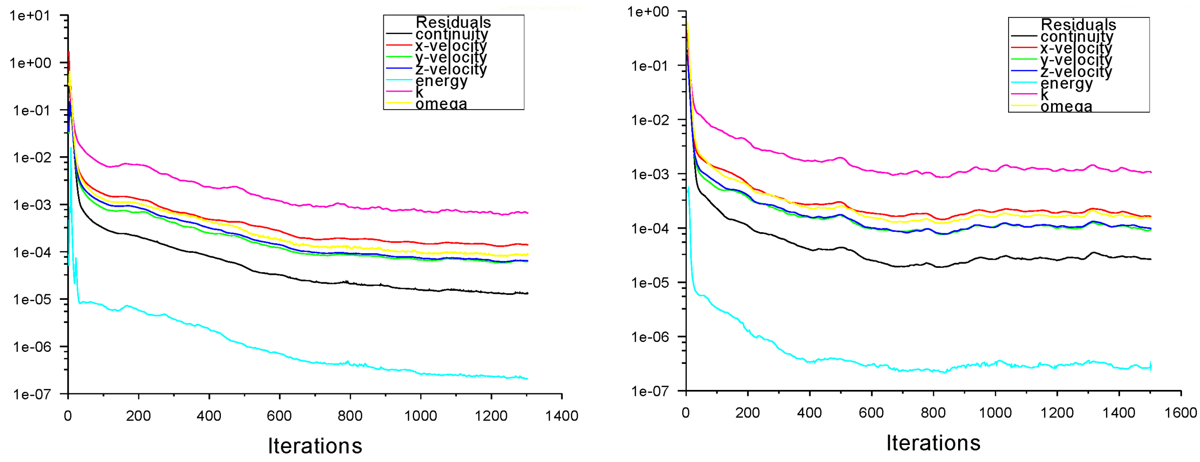

(a) (b)

Figure 6.7: *Scaled residuals for staggered fins (a) with bypass and (b) without bypass.*

expected with the corresponding higher velocity. The surface temperature is based on an area weighted average of the combined wetted surface area.

Reynolds number	**2000**	**4000**	**6000**	**8000**	**10,000**	**20,000**
T_{max} $[K]$	413.0	394.3	386.1	378.6	371.8	358.4
T_o $[K]$	326.1	314.6	310.8	308.9	307.7	305.4
$T_{surface}$ $[K]$	350.6	336.4	329.8	325.2	321.5	314.5
h-value $[W/m^2\,K]$	1094	1405	1683	1939	2390	3743
ΔP $[Pa]$	159	534	1137	1949	2984	11,513
P_{pump} $[Pa]$	0.001	0.007	0.021	0.068	0.094	0.724

Table 6.9: *Results from CFD simulation of staggered fins design.*

The uniformity is seen to increase at a higher Reynolds number which is shown in figure 6.8. On the left hand side in this figure the temperature distribution on the base of the cold plate is shown for a mass flow rate based on a Reynolds number of 2000. On the right hand side the temperatures are seen to be significantly lower.

These tendencies for the uniformity are also shown in table 6.10. The standard deviation for the values on the backside of the cold plate is seen to get lower as the mass flow rate becomes higher.

Reynolds number	**2000**	**4000**	**6000**	**8000**	**10,000**	**20,000**
T_{mean} $[K]$	353.6	339.3	332.9	329.2	325.6	318.9
T_{max}/T_{mean} [-]	1.168	1.162	1.160	1.15	1.142	1.124
σ_{T_s} $[K]$	24.84	21.03	19.03	17.37	16.08	12.97

Table 6.10: *The standard deviation and the ratio between the max. temperature and mean temperature on the backside of the cold plate for the different Reynolds numbers.*

In figure 6.8 it is seen that one side of IGBTs is warmer than the other side. This is due to a poor distribution of the fluid flow in the manifold. To visualize this an image of the streamlines through the design is shown in figure 6.9. The inlet is in the lower right corner of this figure. The velocities are larger in the last rows of fins

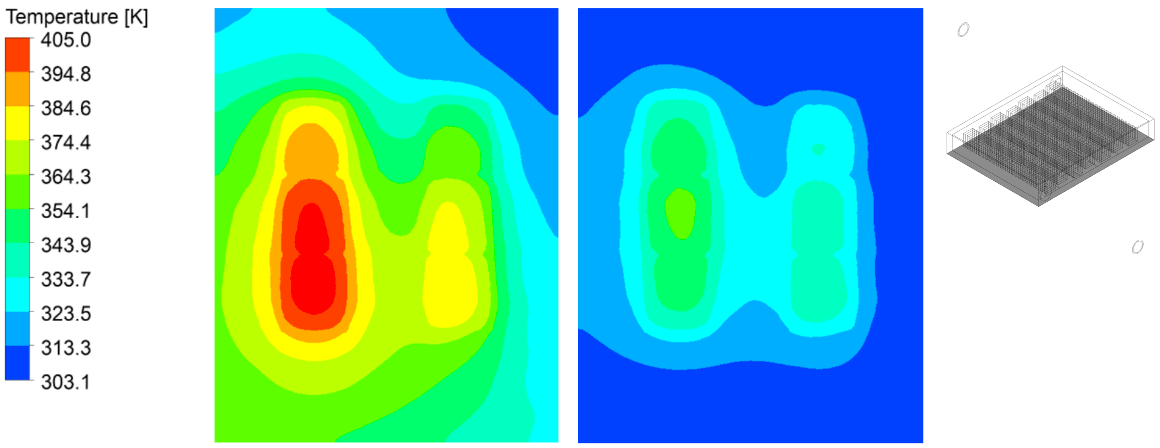

Figure 6.8: *Temperature distribution on backside of cold plate for Re=2000 (left) and for Re=20,000 (right). Both figures are for the staggered fins design.*

form the point of view of the inlet, hence causing the maldistribution of the flow. From this it is concluded, that the manifold is not designed properly to distribute the flow evenly. This is elaborated in appendix E.

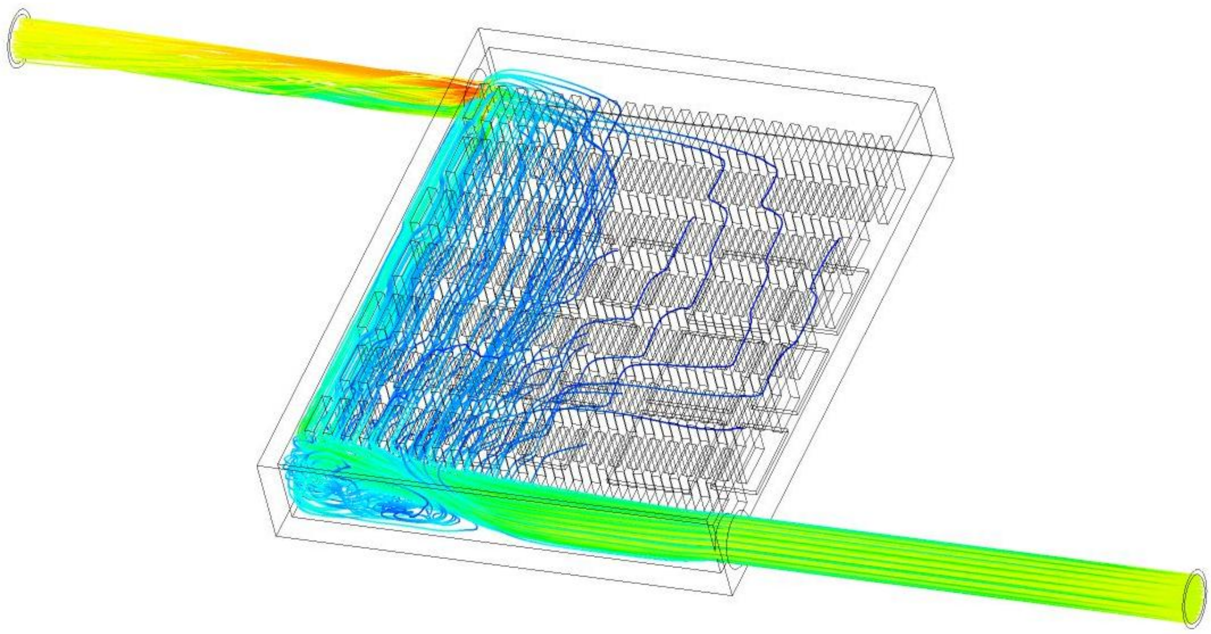

Figure 6.9: *Streamlines through staggered fins design.*

6.3.1 Staggered Fins Design Without Bypass

The staggered fins design is also made without bypass to compare if it is advantageous with this feature in the design. The mesh is made in a similar way as in the previous section, and the mesh is shown in figure 6.10. In figure 6.10 (a) the mesh for the fluid domain is seen, and in figure 6.10 (b) the mesh is shown with a cut through one of the rows of the fins. From the figure it is clear how the the fluid (blue domain) is enclosed in the short channels with no bypass possible.

The results from the mesh independency study are shown in table 6.11. It is concluded that the mesh of 2.0

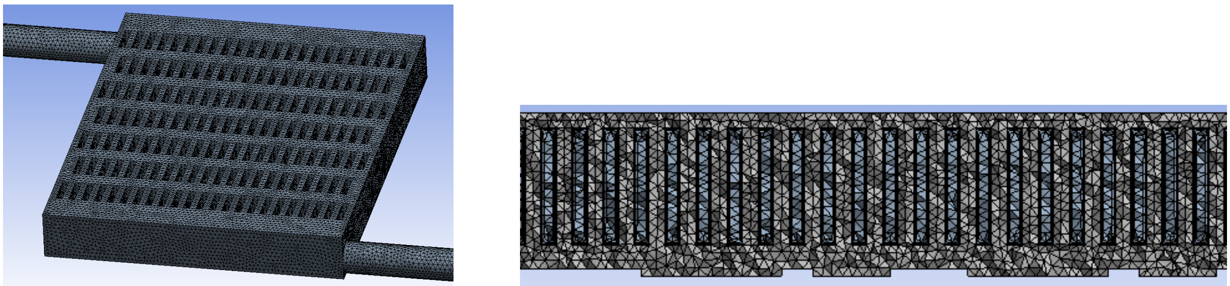

(a) (b)

Figure 6.10: Mesh in fluid domain in staggered fins design without bypass (left), and the mesh seen in a sideways cut (right).

million cells is sufficiently the give a mesh independent result, because the change from coarse to medium is negligible.

Mesh size	**Coarse (1,561,298)**	**Medium (2,016,851)**
h-value $[W/m^2\,K]$	3929	3946
Pressure difference $[Pa]$	3103	3118
T_s $[K]$	315.3	315.3
T_{max} $[K]$	356.4	356.5
Overall mass rate balance $[kg/s]$ (%)	-3e-06 (0.01)	1e-6 (0.003)
Overall energy balance $[W]$ (%)	-0.48 (0.08)	0.04 (0.007)

Table 6.11: h-value, surface temperature, maximum temperature and pressure difference for mesh independency check for the staggered fins without bypass design.

The turbulence intensities and mass flows are similar to the ones listed in table 6.8 as the inlet tube is identical to the one on the design with a bypass. The results from these simulations are shown in table 6.12. The tendencies for the results are similar to the design with a bypass, but the values for the design without bypass is seen to be superior compared to the design with a bypass, as the h-value increase by approximately 33 %, and the pumping power does not change significantly.

Reynolds number	**2000**	**4000**	**6000**	**8000**	**10,000**	**20,000**
T_{max} $[K]$	386.4	370.9	363.8	360.3	356.4	349.4
T_o $[K]$	326.0	314.6	310.8	308.9	307.7	305.4
T_s $[K]$	334.8	324.2	319.7	317.6	315.3	311.4
h-value $[W/m^2\,K]$	1152	1761	2843	3093	3615	4979
ΔP $[Pa]$	168	562	1196	2058	3103	11,743
P_{pump} $[W]$	0.001	0.007	0.03	0.05	0.10	0.74

Table 6.12: Results from CFD simulation of the staggered fins without bypass design.

The temperature distribution on the backside of the cold plate is seen in figure 6.11. The uniformity is better with a higher Reynolds number. The uniformity is also expressed in table 6.13. The values for the uniformity is better without bypass than with a 2 mm bypass.

From the results presented in this section is is seen that it is not an advantage to have a 2 mm bypass. The

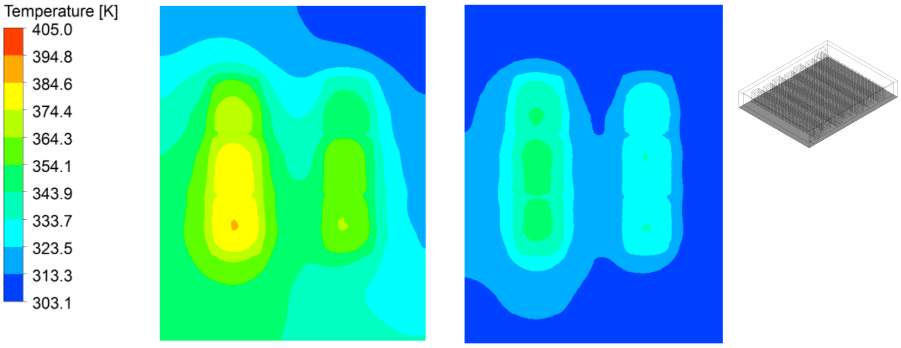

Figure 6.11: *Temperature distribution on backside of cold plate for Re=2000 (left) and for Re=20,000 (right). Both figures are for the staggered fins without bypass design.*

Reynolds number [-]	**2000**	**4000**	**6000**	**8000**	**10,000**	**20,000**
T_{mean} $[K]$	338.9	329.8	324.8	323.1	321.1	317.6
T_{max}/T_{mean} [-]	1.140	1.1248	1.120	1.115	1.110	1.100
σ_{T_s} $[K]$	17.94	14.97	13.64	12.91	12.30	10.90

Table 6.13: *The standard deviation and the ratio between the max. temperature and mean temperature on the backside of the cold plate for the different Reynolds numbers.*

primary advantage of having the bypass is that the pressure is lower, and the heat transfer is supposed to be better when there is a bypass [Danfoss, 2012]. The difference in pressure loss is however rather small with only a value of 230 *Pa* for the flow with Reynolds number of 20,000, and the heat transfer coefficient is actually decreased. The higher heat transfer without bypass might also be due to a higher fin area as all the fins now are 2 *mm* higher.

In figure 6.12 the velocity magnitude in a sideways cut trough the domain is shown for both the design with and without a bypass. The peak values are higher for the design with a bypass, and in general high above the fins. For the design without bypass it is seen that velocities are higher inside the water channels, which also is an advantage for the heat transfer.

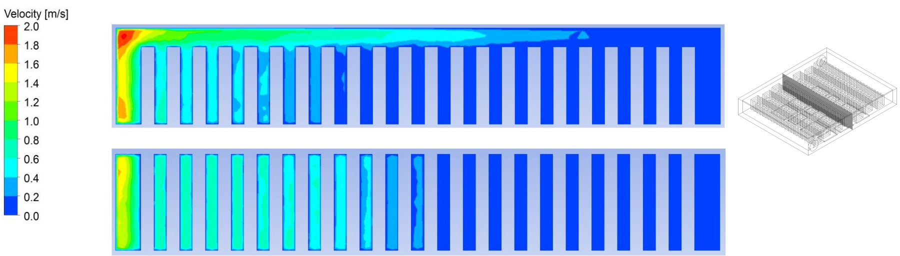

Figure 6.12: *Velocity magnitude across fins. Above: Staggered fins with a bypass, and below staggered fins design without bypass.*

From this study it is concluded that a 2 *mm* bypass is not preferable. A bypass is perhaps still advantageous, but then the bypass has to be significantly smaller.

6.4 Multijet Design

For pre-processing ANSYS GAMBIT is used, where the geometry is defined and the mesh is generated. The meshed geometry is simplified compared to the manufactured design:

- Only half of the geometry is considered due to the assumed nature of symmetry in the design.
- Some rounded corners in the manufactured design are considered as sharp corners in the meshed geometry.
- The inlet manifold is not considered, and thus inlet tubes are considered instead.

In figure 6.13 the computational domain is shown. The blue color indicates inlet boundary, the red color indicates outlet boundary, and the yellow color indicates a symmetry boundary. The IGBTs and diodes are shown in purple and cyan, respectively.

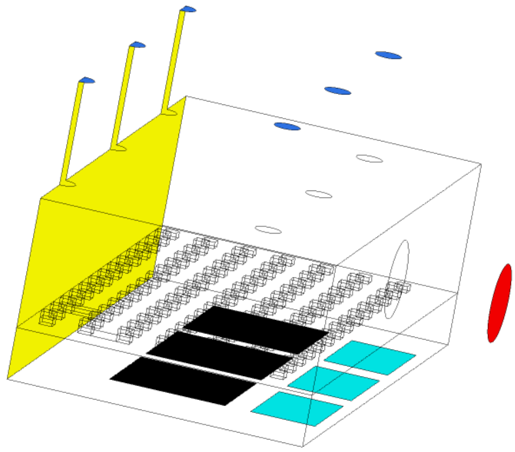

Figure 6.13: *CFD domain for multijet design.*

6.4.1 Mesh

The find a good resolution of the boundary layer the y^+ is calculated from equation (6.1). With a Reynolds number of 10,000 and an inlet diameter of 0.002 m, the distance from the wall to the center of the first adjacent cell, Δy_p, is equal to 4 μm. This results in an expected y^+ of 2.53.

The boundary layer mesh is shown in figure 6.14 (a). Zone 1 corresponds to the solid, and zone 2 corresponds to the fluid. The brown colored mesh indicates fluid mesh, the blue colored mesh indicates a solid square mesh, and the red colored mesh indicates the solid bottom mesh. In order to ensure a low value of y^+, the mesh in the top of the squares and the bottom mesh has a spacing to the first point of 8 μm with 10 elements for the first 0.5 mm away from the wall. Further away from the wall and in the solid bottom the spacing is 0.33 mm.

In figure 6.14 (b) the mesh in the circular inlets is shown. In order to have hexahedral cells a square is drawn in the center, and thus the circle is transformed to five squares. A low y^+ is ensured by a boundary layer refinement similar to with the above discussion. Where the jet exits the tube, a box consisting of a hybrid mesh with tetrahedral and hexahedral cells is made. The total number of cells in the meshed geometry is 520,944.

A mesh independency check is carried out by refining the mesh by mesh adaption in ANSYS FLUENT. Changing the refinement threshold, two meshes are produced: A medium mesh with 751,687 cells and a fine mesh

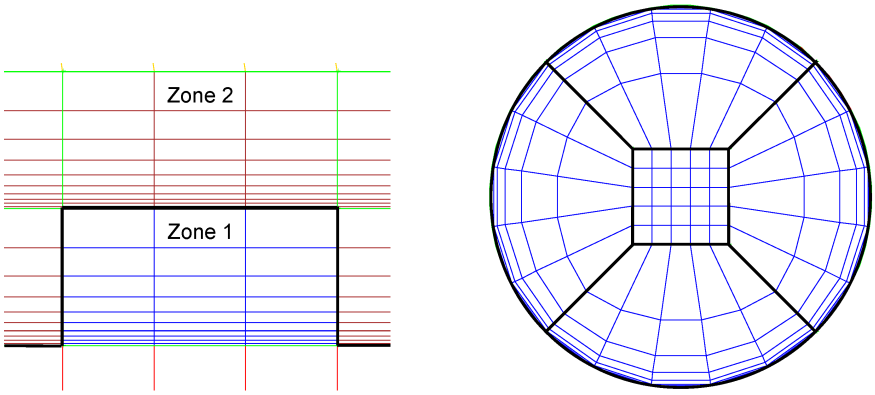

(a) (b)

Figure 6.14: *Zoom on boundary layer mesh (a), and mesh in circular inlets (b).*

with 905,475 cells. For all simulations the second order spatial discretization scheme is used. Three overall parameters are checked: Maximum temperature, maximum velocity and overall h-value. The results are shown in table 6.14. The difference of the parameters between the mesh sizes is not large, and the temperature is the same for the medium and fine mesh.

Parameter	**Coarse (520,944)**	**Medium (751,687)**	**Fine (905,475)**
T_{max} $[K]$	337.3	337.2	337.2
v_{max} $[m/s]$	4.58	4.60	4.59
h-value $[W/m^2\,K]$	20,746	20,674	20,948
Overall mass rate balance $[kg/s]$ (%)	-1.61e-05 (0.03)	-5.74e-06 (0.01)	3.74e-05 (0.07)
Overall energy balance $[W]$ (%)	-0.38 (0.13)	-0.39 (0.13)	1.12 (0.37)

Table 6.14: *Maximum temperature, maximum velocity and overall h-value for mesh independency check.*

Figure 6.15 shows a contour plot of the difference in velocity magnitude from the coarse mesh and medium mesh. By using CFD-post it is possible to compare two contour plots from the same case. Some differences are found, but they are of low velocity magnitude. The difference lies in the areas of the jet penetration from the inlet and on the target plate. Especially the jet-to-jet interaction may cause problems for the simulation, because this phenomena most likely is transient, and not steady state. This could explain the maximum difference of 2.04 m/s, shown by the label in figure 6.15.

From the above considerations and results the medium mesh is chosen as the mesh independent simulation. The boundary conditions to the CFD simulation are shown in table 6.15.

Reynolds number [-]	**2000**	**4000**	**6000**	**8000**	**10,000**
Inlet mass flow rate $[kg/s]$	0.011	0.023	0.034	0.045	0.056
Inlet turbulence intensity (%)	6.2	5.7	5.4	5.2	5.0
Outlet turbulence intensity (%)	5.9	5.4	5.1	4.95	4.94

Table 6.15: *Mass flow rate and turbulence intensities for boundary conditions.*

Figure 6.16 (a) shows y^+ along a line in the jet array for a Reynolds number of 10,000, where the velocity and

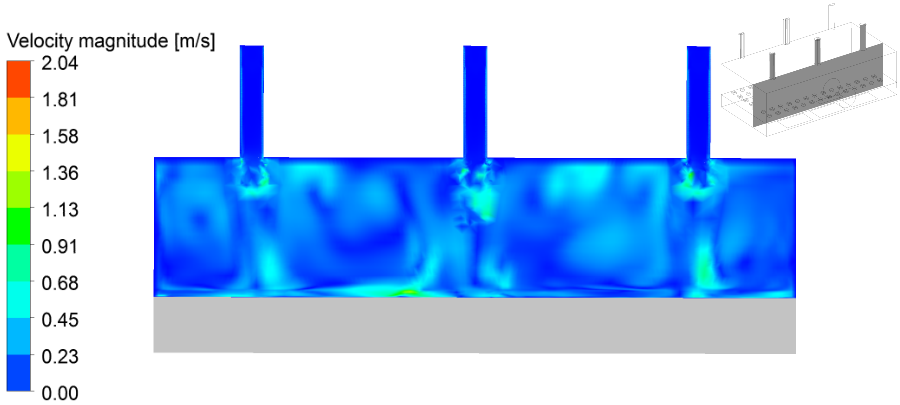

Figure 6.15: *Contour plot of difference in velocity magnitude in jets for coarse to medium mesh.*

thus the y^+ is expected to be the highest. Generally the y^+ is low and does not exceed 0.5, but at the end points the y^+ reaches a value of more than 2. The three zones where the y^+ reaches 0.5 indicate the impingement zones of the jets. Figure 6.16 (b) shows residuals for the simulation with an asymptotic tendency. The residuals do not settle at a specific value, but the fluctuations are not considered a problem for the convergence.

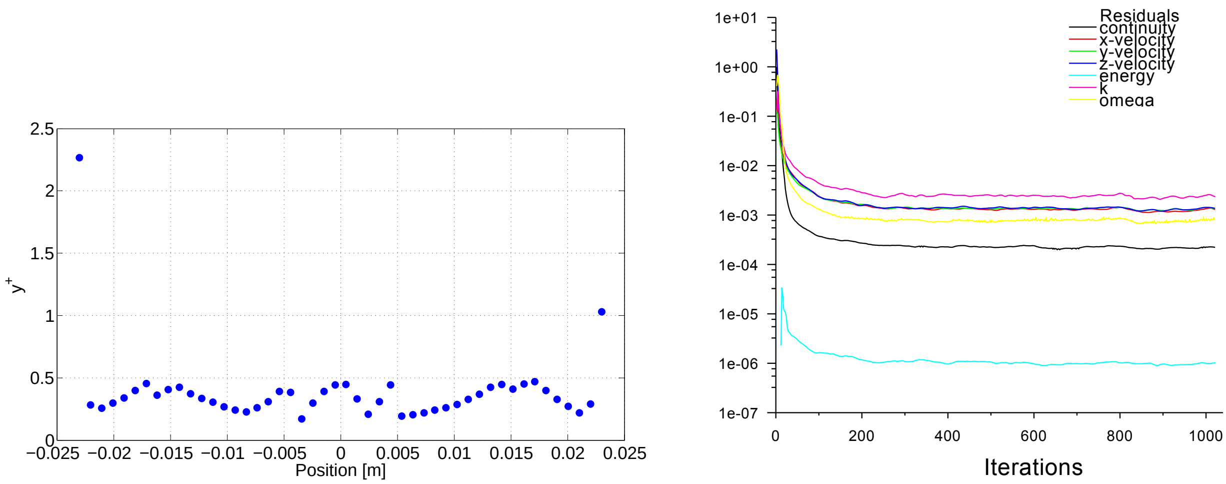

(a) (b)

Figure 6.16: *y^+ along surface in jet array (a), and scaled residuals (b).*

6.4.2 Results

Table 6.16 shows various results from the simulations. The maximum velocity is 4.60 $^m/_s$, which is more than the expected 4 $^m/_s$, because flow is developing through the inlet tube. The maximum temperature decreases as the mass flow rate is increased, which is expected and shown by an increase in h-value reaching more than 20,000 $^W/_{m^2\,K}$. The pressure loss shows good coherence with theory, as the pressure loss increases with the velocity squared. Notice that the pumping power is shown for half the geometry, and thus is doubled for the full geometry.

In figure 6.17 the temperature distribution on the backside of the cold plate is shown for Reynolds number

Reynolds number	**2000**	**4000**	**6000**	**8000**	**10,000**
T_{max} $[K]$	364.9	349.9	343.1	339.9	337.2
T_o $[K]$	309.5	306.3	305.3	304.7	304.4
$T_{surface}[K]$	338.9	325.7	320.3	317.4	315.3
v_{max} $[^m/_s]$	1.02	1.93	2.84	3.75	4.60
h-value $[^W/_{m^2\,K}]$	7361	11,453	14,894	17,755	20,746
Δp $[Pa]$	569	2003	4260	7279	11,012
P_{pump} $[W]$	0.0065	0.045	0.145	0.330	0.624

Table 6.16: *Results from the CFD simulation.*

of 2000 and 10,000. The temperature is lowest in the case of higher Reynolds number, as expected. The ratio between the maximum temperature and the area averaged temperature is evaluated for all cases. The ratio should be unity for a perfect temperature distribution. In table 6.17 the ratios are shown. The ratios are relatively similar in magnitude, and are close to being unity, but the tendency is that a higher Reynolds number yields a more uniform temperature distribution. In table 6.17 the standard deviation for the temperature distribution on the backside of the cold plate is also shown.

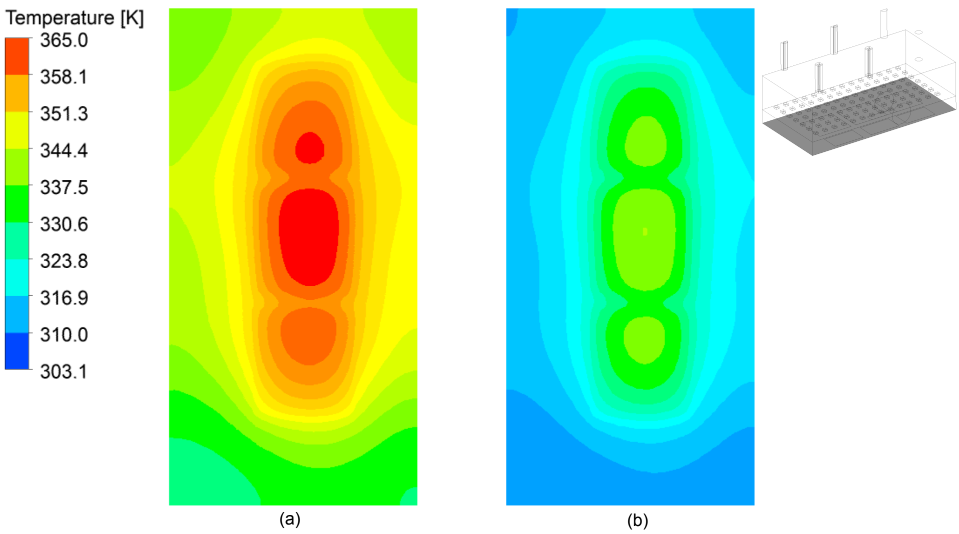

Figure 6.17: *Temperature distribution on backside of cold plate for (a) Re = 2000 and (b) Re = 10,000.*

Reynolds number	**2000**	**4000**	**6000**	**8000**	**10,000**
T_{mean} $[K]$	345.2	331.3	325.8	322.8	320.5
$^{T_{max}}/_{T_{mean}}$ [-]	1.057	1.056	1.053	1.053	1.052
σ_{T_s} $[K]$	9.47	8.62	8.11	7.85	7.62

Table 6.17: *Ratio between max temperature and mean temperature, and the standard deviation of the surface temperature on backside of cold plate.*

In figure 6.18 a contour plot of the velocity magnitude in yz-plane and xz-plane is shown. It shows that the middle jet in figure 6.18 (a) is affected by the outlet and the surrounding jets, and thereby is deflected. The cooling is thus not directly at the target of the IGBT, and the maximum h-value is not achieved in the middle of the IGBT.

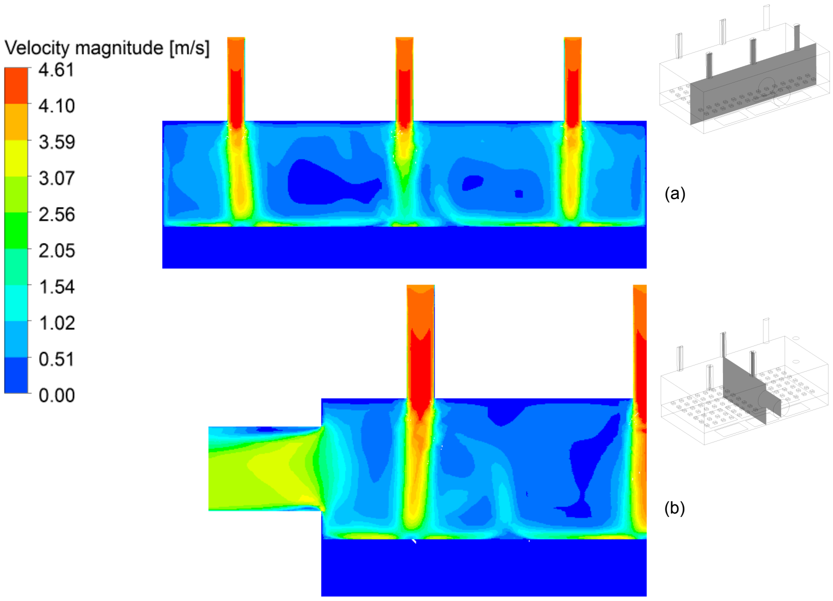

Figure 6.18: *Contour plot of velocity magnitude in a) yz-plane and b) xz-plane.*

Figure 6.19 shows a contour plot of the velocity magnitude between the bottom plate squared fins. It shows, that the flow is disturbed by the squared fins, as expected. In the areas of the IGBTs the velocity is high, which gives good cooling performance. In the areas of where the flow from the jets meets each, jet-to-jet interaction occurs, and results in low velocity. Some areas show a tendency of rather low velocity, which may be because of blocking by the squared boxes, as a consequence of the chosen design.

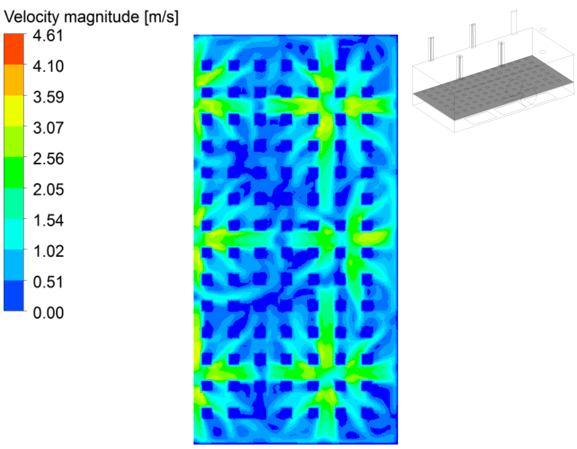

Figure 6.19: *Contour plot of velocity magnitude in xy-plane between squares.*

6.5 Hybrid Design

The hybrid geometry is drawn in ANSYS GAMBIT. The meshed geometry is simplified compared to the manufactured design by:

- Half of the geometry is considered due to symmetry.
- The rounded corners in the manufactured design are considered as sharp corners in the meshed geometry.
- The inlet manifold is not considered, and thus inlet tubes are considered.

6.5.1 Mesh

In order to get a good prediction of the flow field and heat transfer the mesh is created with a y^+ value in the range of 1-5 in the first cell adjacent to the wall. With a Reynolds number of approximately 170 in the mini channels, the length of the first cell is found to be 80 μm if y^+ is equal to one. With a cell length of 150 μm, the y^+ value is 3.7, which results in a total of eight cells across the channel width. It is chosen to have six cells across the fin width. The meshed channel is shown in figure 6.20 (a). The red mesh, zone 1, indicates the fins and the blue mesh, zone 2, indicates the channel. Figure 6.20 (b) shows the mesh in and around the prism. Due to a desired y^+ value in the range of 1-5 in the first cell adjacent to the wall, the mesh around the prism is refined to a spacing of 20 μm.

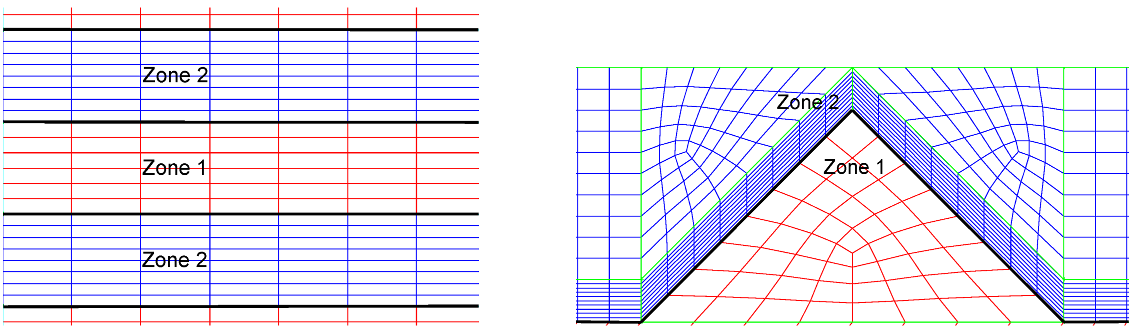

(a) (b)

Figure 6.20: Mesh in the channel and in the fins (blue and red, respectively) (a). Mesh in and around prism (red and blue, respectively) (b).

The mesh for the round inlets and outlets are made in similar way as the mesh for the multijet, where the circular tube is split into five squares. A mesh independency check is carried out to examine whether the geometry is sufficiently spatial discretized. The original mesh is refined using the mesh adaption option in ANSYS FLUENT, by refining the areas where the velocity gradient is high. The mesh is refined with 15.9 % and 25.1 %, respectively. For all three simulations the second order spatial discretization scheme is used. The results of the refinement are presented in table 6.18, where the overall mass and energy balances are checked, along with maximum temperature and velocity, as well as the overall h-value.

Table 6.18 shows that the difference in results is small and therefore the original coarse mesh with 1,597,960 cells is used for the simulations. Along with the values in the above table different contour plots has been examined in order to see if the results are physical meaningful. As for the multijet design two contour plots for different sizes are compared. This is done between the coarse and the medium mesh, and the coarse and the fine mesh. This shows very little difference in the areas of the jets. Figure 6.21 shows the velocity difference

Parameter	**Coarse (1,597,960)**	**Medium (1,899,005)**	**Fine (2,132,077)**
$T_{max}[K]$	337.3	337.2	337.2
v_{max} [$^m/_s$]	4.58	4.60	4.59
h-value [$^W/_{m^2\,K}$]	16,438	16,310	16,150
Overall mass rate balance [$^{kg}/_s$] (%)	9.91e-7 (0.004)	-2.46-e7 (0.001)	5.75e-7 (0.003)
Overall energy balance [W] (%)	-0.51 (0.17)	-0.42 (0.14)	-1.76 (0.59)

Table 6.18: *Maximum temperature, maximum velocity and overall h-value for mesh independency check for the hybrid design.*

between coarse and medium mesh. The maximum velocity difference is high in the areas of the jets, which is due to the difficulties in modeling the jet-to-jet interaction.

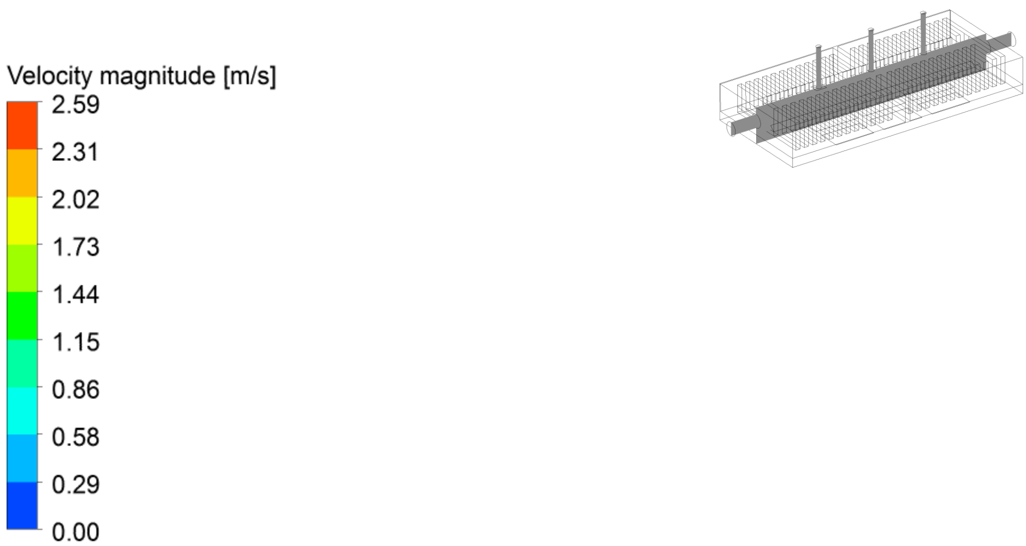

Figure 6.21: *Contour plot of difference in velocity magnitude in jets for coarse to medium mesh.*

Five different Reynolds numbers have been modeled. The boundary conditions for the five different simulations is shown in table 6.19.

Reynolds number [-]	**2000**	**4000**	**6000**	**8000**	**10,000**
Inlet mass flow rate [$^{kg}/_s$]	0.00451	0.00902	0.01353	0.01805	0.02255
Inlet turbulence intensity [%]	6.2	5.6	5.4	5.2	5.1
Outlet turbulence intensity [%]	6.6	6.0	5.7	5.5	5.3

Table 6.19: *Mass flow rate and turbulence intensities for boundary conditions in hybrid design.*

Figure 6.22 (a) shows the y^+-values along the top of the prism for a Reynolds number of 10,000. The plot is made here, because it is expected to have the highest velocities and thus the highest y^+-values here. The y^+-values peak in the areas of the jet impinging zone, and reaches approximately six were it is highest. This is more than the recommended value for y^+, but it is only a problem in a small area compared to the overall low y^+-values in the geometry. This is the simulation with the highest Reynolds number, so at lower Reynolds numbers this is not a problem. Figure 6.22 (b) shows the residual plot for one of the CFD simulations for the hybrid design, which shows an asymptotic tendency.

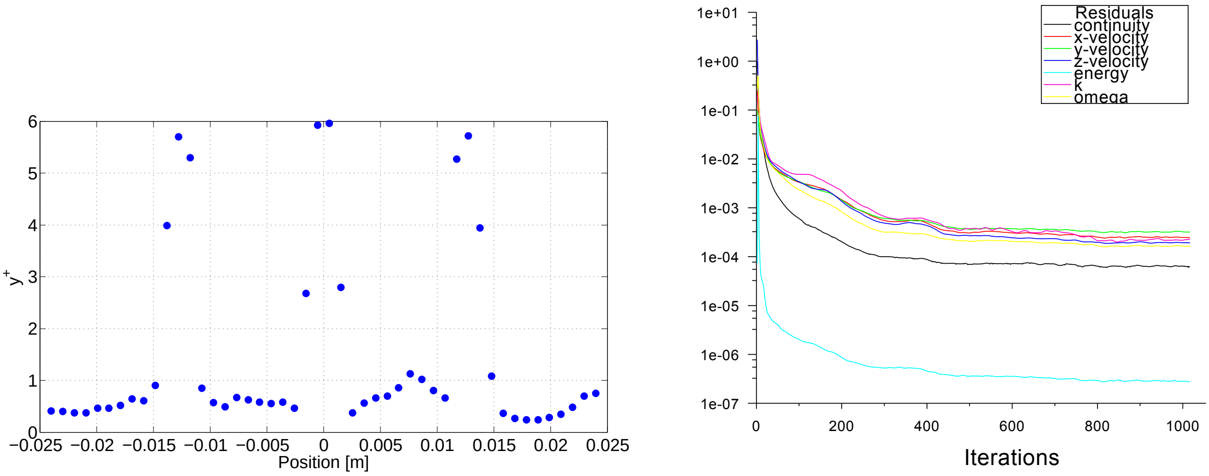

(a) (b)

Figure 6.22: *y^+-values along top of prism (a), and residual plot for the hybrid design CFD simulation (b).*

6.5.2 Results

Various results from the simulations are shown in table 6.20. At a Reynolds number of 6000 this cold plate is designed to have a velocity of 4 m/s. This is not the case for this simulation, due to the development of the flow in the inlet tubes. The maximum overall h-value is found to be approximately 16,500 $W/m^2\,K$. The pressure loss increase correspondingly to the velocity increase squared, which is expected. The pumping power presented in the table is for half of the manufactured geometry.

Reynolds number	**2000**	**4000**	**6000**	**8000**	**10,000**
T_{max} $[K]$	355.6	341.1	335.7	332.4	330.2
T_o $[K]$	319.0	311.1	308.4	307.1	306.3
$T_{surface}$ $[K]$	325.5	314.6	311.0	309.1	307.9
v_{max} $[m/s]$	1.73	3.24	4.73	6.22	7.70
h-value $[W/m^2\,K]$	3771	7213	10,238	13,299	16,438
Δp $[Pa]$	1572	5481	11,696	20,161	30,887
P_{pump} $[W]$	0.007	0.05	0.16	0.37	0.70

Table 6.20: *Parameters from CFD simulation.*

Figure 6.23 shows a contour plot of the velocity magnitude in the area of the jet impingement zone for a Reynolds number of 10,000. In the impingement zone the velocity is generally high, indicating little or no stagnating flow.

Figure 6.24 shows a contour plot of the velocity magnitude in a xy-plane 3 mm above the bottom plate, corresponding to the middle of the channel height for a Reynolds number of 10,000. The figure is shown in order to show the velocity in the channels, where only velocities below 1.8 m/s are admitted to be shown. This gives a detailed view of the velocity in the channels. The contour plot shows that especially the channels close to the

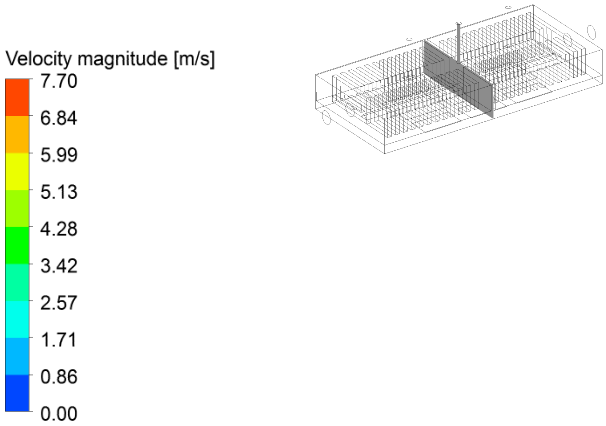

Figure 6.23: *Contour plot of velocity magnitude of jet impingement on pyramid for Re* $= 10,000$.

outlets have low velocity, whereas the channels close to the jets generally have the highest velocity in the range of 1 m/s, which results in low cooling performance in these areas. The cause of this could be the prism in the middle of the jet, since this would guide the flow to be parallel, and not normal, to the channels. Thereby little flow reaches the outer channels.

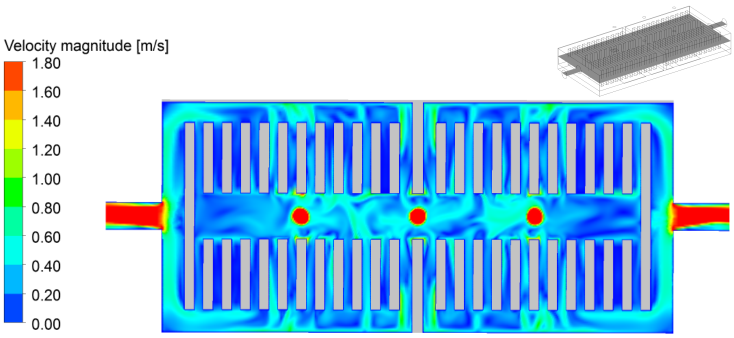

Figure 6.24: *Contour plot of velocity magnitude 3 mm above bottom plate for Re = 10,000.*

Figure 6.25 shows a 3D streamline plot of the velocity magnitude. This also indicates that little flow is present in the channels close to the outlets.

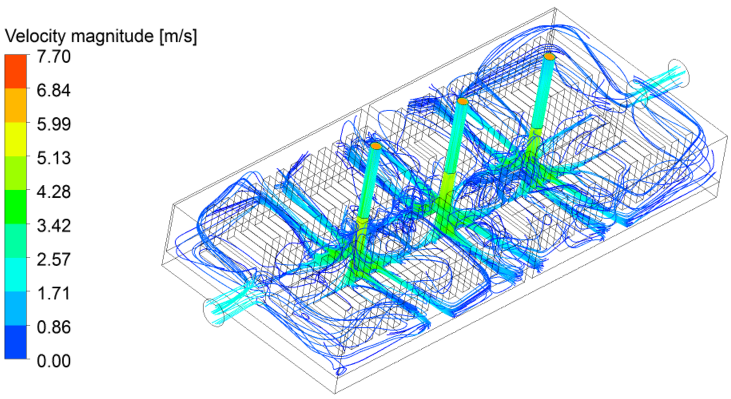

Figure 6.25: *Streamline plot of velocity magnitude.*

Figure 6.26 (a) shows a contour plot of temperature in the same plane as figure 6.23 for a Reynolds number of 10,000. It shows, that the temperature in the prism is relatively high, which is expected. From the analysis in chapter 5.5.1 it is shown, that the temperature is higher in the prism zone in the case of a smaller prism, or with no prism. The figure also shows, that the jet is not placed directly above the IGBT, which may result in a higher temperature. When using the IGBT power module in normal operation, heat is also dissipated in the diodes, which in figure 6.26 is to the right of the IGBT. Figure 6.26 (b) shows the temperature on the backside of the cold plate for the highest and lowest simulated Reynolds number.

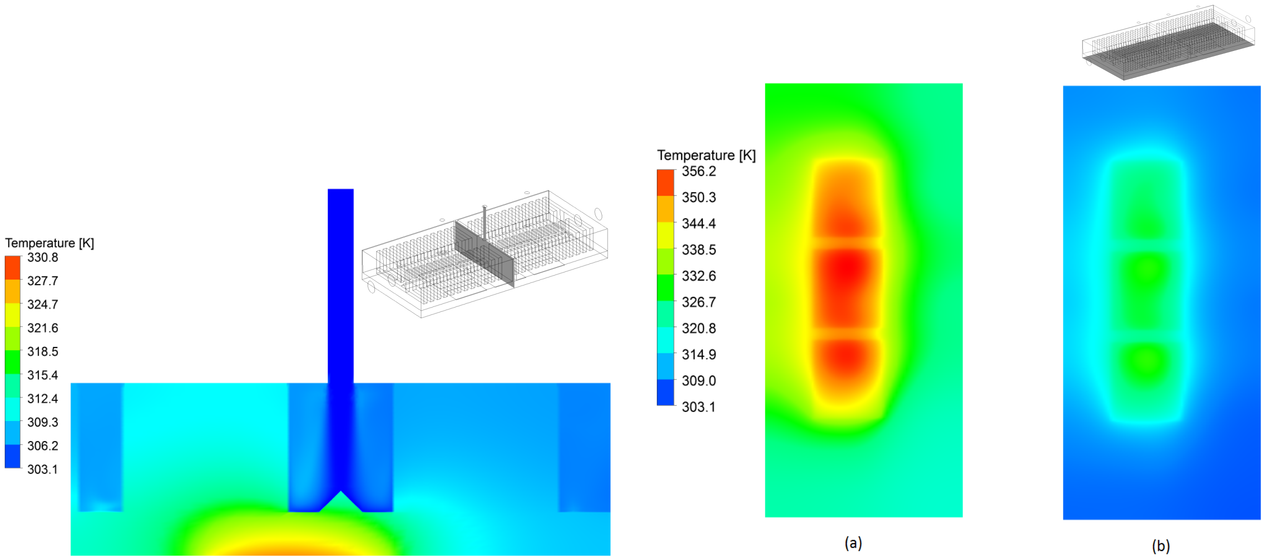

(a) (b)

Figure 6.26: (a) Contour plot of temperature in jet plane, and (b) temperature distribution on backside of cold plate for (a) Re=2000 and (b) for Re=10,000.

In table 6.21 the ratio between the maximum temperature and the mean temperature on the backside of the cold plate is shown in order to check the temperature distribution.

Reynolds number	**2000**	**4000**	**6000**	**8000**	**10,000**
T_{mean} $[K]$	333.55	321.8	317.6	315.1	313.6
T_{max}/T_{mean} [-]	1.066	1.060	1.057	1.055	1.053
σ_{T_s} $[K]$	9.92	8.53	7.80	7.33	7.00

Table 6.21: Ratio between maximum temperature and mean temperature, and the standard deviation of the surface temperature on the backside of cold plate.

6.6 Design Comparison

The five designs considered are here compared to each other. The performance criteria are the ones that benefit the IGBT power module with better efficiency and longer lifetime, which are found in chapter 4, and stated here again:

1. Uniform temperature distribution in IGBT power module for uniform thermal expansion.

2. Low junction temperature in order to enhance performance and lifetime.
3. Low system operation cost of cooling design due to automotive applications.

In the following the pumping power for multijet and hybrid design is multiplied with 2, because they represent half of the geometry to be cooled. The pressure loss remains the same, but the mass flow rate is doubled. This gives a doubling in pumping powers for the multijet and hybrid design compared to the mini channel designs. The pumping power is calculated by the following equation, assuming an isentropic pump efficiency of 100 % [Cengel and Cimbala, 2006]:

$$P_{pump} = \Delta p \cdot \dot{V} \qquad [W] \tag{6.4}$$

To find the design with the most uniform temperature distribution the ratio between the maximum temperature and mean temperature on the cold plate is found for all designs. Figure 6.27 shows this ratio versus the required pumping power for all designs. The figure indicates the best cost-effectiveness, when considering the temperature distribution. All designs show an asymptotic tendency, as the required pumping power is increased, and at some point the change in temperature distribution is not improved much with more pumping power. This is due to bad cost-effectiveness. The designs with the highest ratio is staggered fins with and without bypass, where in particular it is seen that bypassing with 2 *mm* is not advantageous. The mini channel design gives better temperature distribution, but the two best designs for uniform temperature distribution must be concluded to be the multijet design and the hybrid design. The multijet design performs slightly better at low pumping power, but at higher pump power the difference is small.

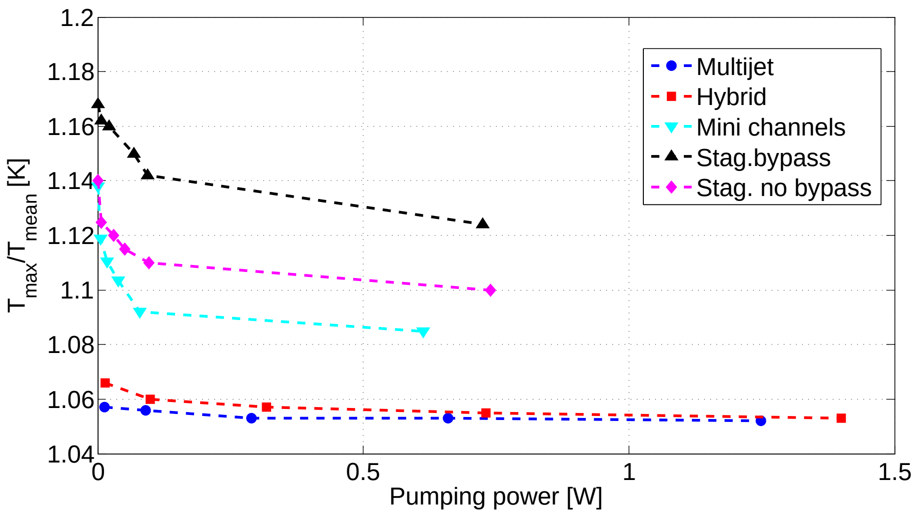

Figure 6.27: *Temperature ratio versus pumping power for the designs.*

Another measure of temperature uniformity is the standard deviation of the temperatures on the backside of the cold plate. A low standard deviation represents good temperature uniformity, as the standard deviation represents the average temperature deviation from the mean temperature. Figure 6.28 shows the standard deviation versus the required pumping power for all designs. The same overall picture is seen as in figure 6.27, but some differences are noticed; The staggered fins design without bypass performs better than mini channels at the low pumping powers. Another difference is, that the best design for temperature uniformity is the hybrid design at the highest pumping powers, and not the multijet design as found in figure 6.27.

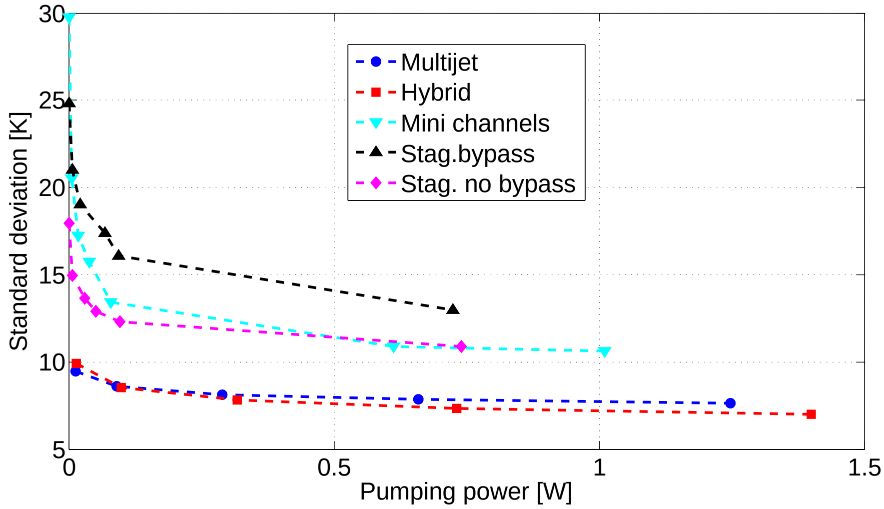

Figure 6.28: *Standard deviation versus pumping power for the designs.*

Figure 6.29 shows the maximum temperature versus the required pump power for all designs. This indicates the best cost-effectiveness, when considering the maximum temperature. All designs show an asymptotic tendency. The hybrid design performs best of all designs, and performs 5-10 K better in the range than the second best, the multijet design. The staggered fins designs does not perform well.

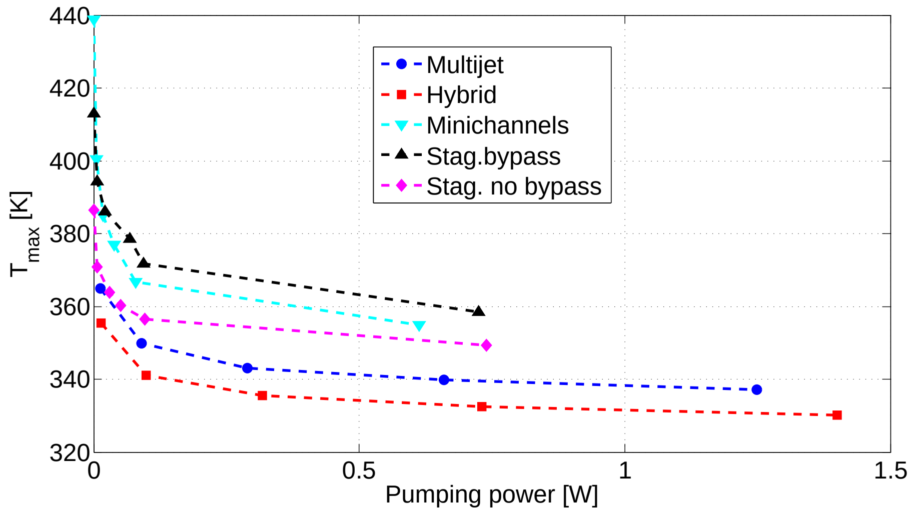

Figure 6.29: *Maximum temperature versus pumping power for designs.*

Figure 6.30 shows the overall convective heat transfer coefficient, h, versus the required pump power for all designs. This value should be as high as possible to ensure a low temperature difference between the wetted surface and the fluid, referring to equation 3.2. The highest h-value is achieved by the multijet design, reaching more than 20,000 $W/m^2\,K$. The hybrid design achieves a maximum of approximately 16,000 $W/m^2\,K$. The three other designs does not achieve comparable h-values, where the maximum h-value of 5000 $W/m^2\,K$ is achieved by the staggered fins design without bypass.

In figure 6.31 the pressure loss is shown versus the mass flow for all CFD simulations for the five designs. The mass flow is for the full scale for the hybrid and multijet design. For the same mass flow the hybrid design has

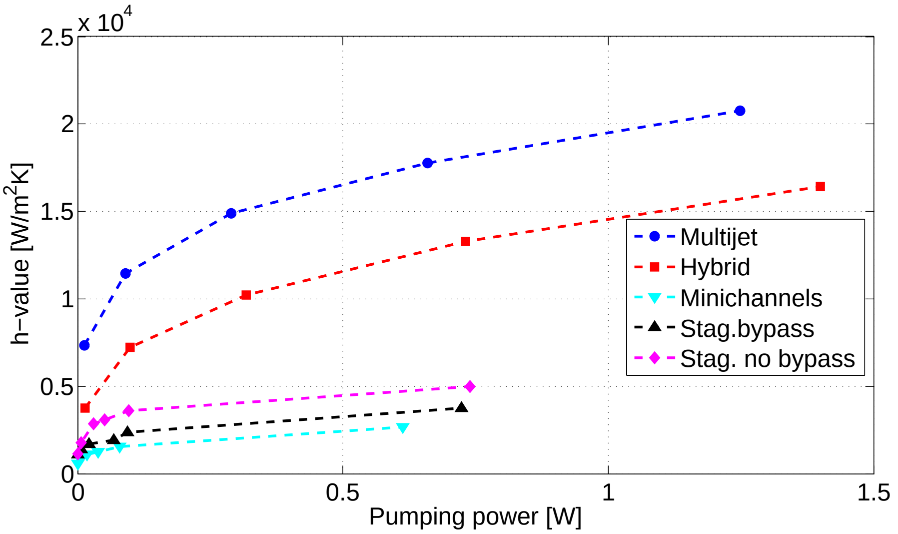

Figure 6.30: *h-value versus pumping power for designs.*

the highest pressure loss, due to the presence of both mini channels and a small inlet diameter for the jets. The other designs have lower pressure loss due to e.g. bigger inlet diameters.

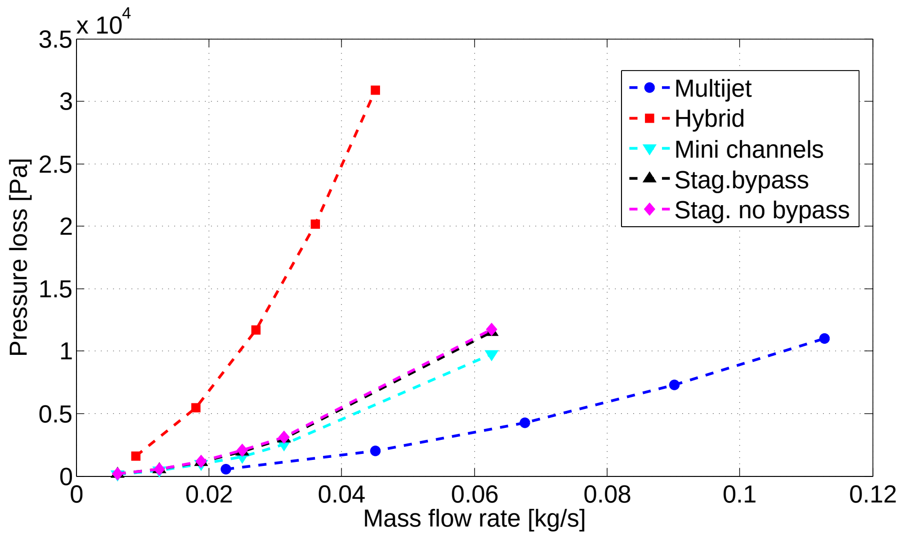

Figure 6.31: *Pressure loss versus mass flow for the 5 designs.*

In general it is seen from the results that the mini channel design and the staggered fins design, with and without a bypass, have a lower cooling performance compared to the multijet and hybrid design. This applies for both temperature uniformity, h-value, and the junction temperature at the same pumping powers. The main disadvantage for these designs are the manifold as this distributes the flow poorly in the various channels.

The advantage for the hybrid design is the high surface area together with the direct cooling on the hottest zones of the IGBT power module, as this gives a good temperature uniformity with a high h-value. The multijet design obtains high h-value and good uniformity by having a good mixing in the flow which breaks down the thermal boundary layer and thus enhances the heat transfer. The disadvantage of the hybrid design is the pressure loss. This could be minimized with a larger diameter of the jets.

6.7 Shower Power Comparison

In the following section the hybrid and multijet designs are compared to the cooling concept "Shower Power" developed by Olesen et al. [2006]. The mini channels and staggered fins designs are not compared to Shower Power due to poor performance. Shower Power uses the principle of parallel cooling consisting of multiple inlets and outlets in guided channels, as shown in figure 6.32. In this way the coolant is in contact with the heat source for a short time, and thus the temperature of the increase of the coolant is low. This contributes to a uniform temperature distribution. Olesen et al. [2006] incorporates this along with direct cooling, and thus a thermal interface material is not used. The part is made out of one-part plastic, and thus the manufacturing cost is low. Shower Power is cited by many authors as a benchmark of high convective heat transfer, an example hereof is Parida et al. [2012], Lowe [2009] and Baumann et al. [2011].

Figure 6.32: *Shower Power concept [Olesen, 2012].*

The Shower Power concept is evaluated on h-values against pumping power, as the pressure loss and flow rate as stand alone parameters do not make a detailed insight of the performance and operation cost of the cooling application. All CFD simulations made for comparison is made with the same fluid properties as for Shower Power, which uses a mixture of 50 % glycole and 50 % water at 60 $°C$ [Olesen, 2012]:

- $\rho = 1055\ ^{kg}/_{m^3}$
- $c_p = 3480\ ^{J}/_{kg\,K}$
- $k = 0.394\ ^{W}/_{m\,K}$
- $\mu = 0.00148\ ^{kg}/_{m\,s}$

In addition to this, the material used in the CFD simulations for the designs is copper with a thermal conductivity of $k = 398.3\ ^{W}/_{m\,K}$.

Figure 6.33 shows the h-value for Shower Power versus flow rate along with pumping power versus flow rate, according to Olesen [2012]. The h-value reaches approximately 8500 $^{W}/_{m^2\,K}$ at a flow rate of 6 $^{l}/_{min}$, which according to the pumping power curve corresponds to a pumping power of approximately 0.45 W.

Figure 6.34 shows the h-value for multijet design, hybrid design and Shower Power, all with the fluid properties listed above. The h-value for Shower Power is found by combining the curves in figure 6.33. The pumping

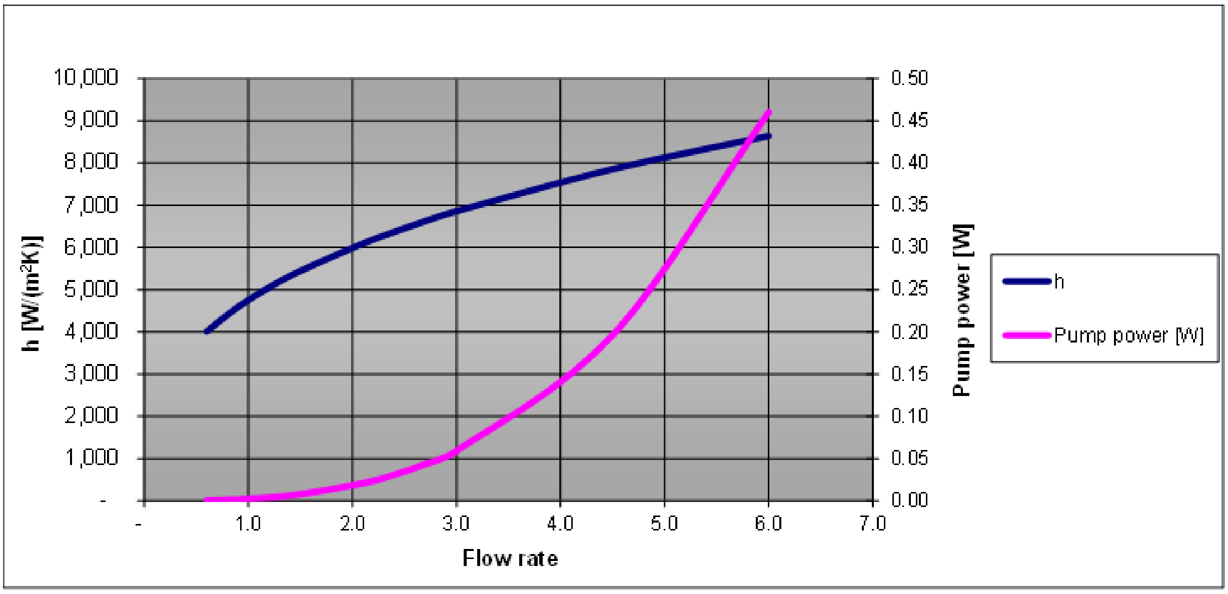

Figure 6.33: *Shower Power h-value versus flow rate [$^{l}/_{min}$] and pumping power versus flow rate [Olesen, 2012].*

power for the multijet design reaches approximately 1.2 W, whereas the hybrid design reaches 1.3 W. The maximum h-value for the multijet design is 12,600 $^{W}/_{m^2\,K}$, and the hybrid design reaches 10,800 $^{W}/_{m^2\,K}$. The h-value for Shower Power starts increasing rapidly with increasing pumping power, but quickly flattens out. The h-value of the multijet and hybrid design does not flatten out as quickly, and also have a rapid increase in h-value in the start. In the low range of pumping powers the h-values are highest for the Shower Power design. It should however be mentioned, that the performance for the multijet and hybrid design are not simulated at these specific pumping powers. If the performance for the Shower Power design is assumed to be extrapolated, with the magenta colored line in figure 6.34, it shows that the h-values will continue to be lower at higher pumping powers compared to the multijet and hybrid design.

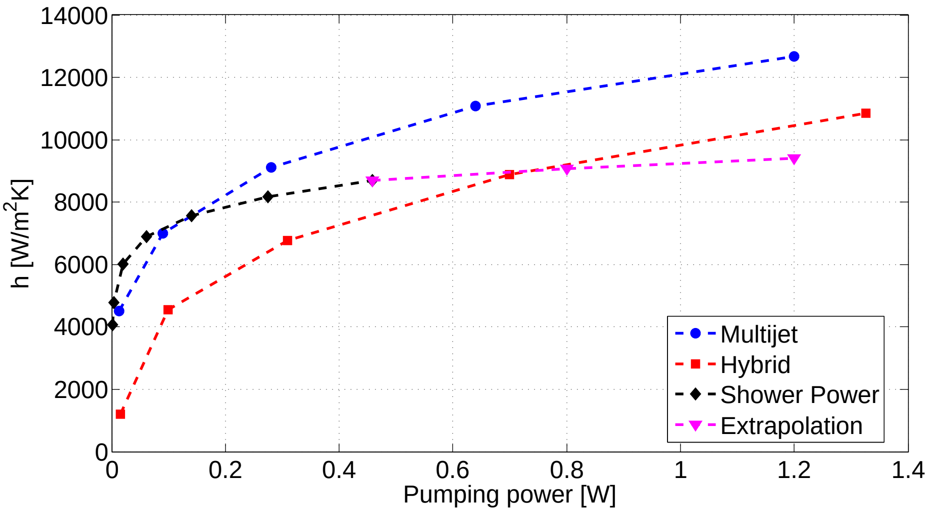

Figure 6.34: *h-value versus pumping power for Shower Power, hybrid and multijet design.*

In figure 6.35 the pressure loss for the these CFD simulations is shown. The pressure loss for the hybrid design is high at a low mass flow, while the pressure loss is lower at higher mass flows for the multijet and Shower

Power design.

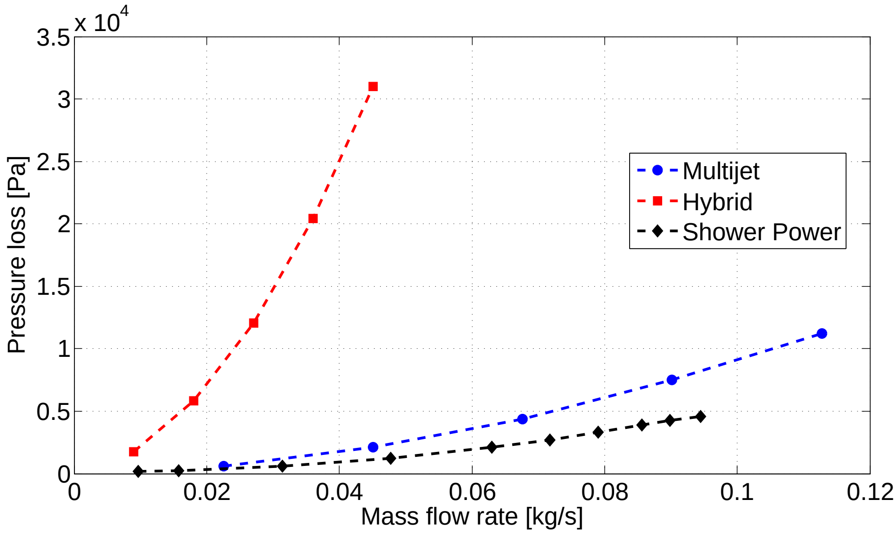

Figure 6.35: *Pressure loss versus mass flow.*

Cooling Performance Experiments

7

This chapter documents the conducted cooling performance experiment, where the hybrid and multijet designs are tested. The following sections are included in this chapter:

7.1 Purpose

In order to validate the CFD simulations and to test prototypes of the cooling designs an experiment is carried out to measure the cooling performance of each design. The aim of the experiment is to determine if the chosen cooling designs provide sufficient cooling for the IGBT power module.

7.2 Method

The methodology of the experiment is to supply flow to the cooling design in the range of the CFD simulations. In order to find the cooling performance, the inlet and outlet temperatures are measured along with the flow rate. The pressure loss of the cooling system is measured in order to validate the CFD against this. The IGBT power module is attached to the cooling design with thermal interface material in the interface. The temperature of the thermistor in the IGBT power module is measured under load.

7.3 Theory

To dissipate power from the IGBT power module a voltage and current, corresponding to 300 W, is supplied to pin one and two in figure 4.2 on page 24. The amount of power dissipated in the transistor is dependent on the gate state. In figure 7.1 (a) the relationship between the voltage and the current is shown for different gate voltages.

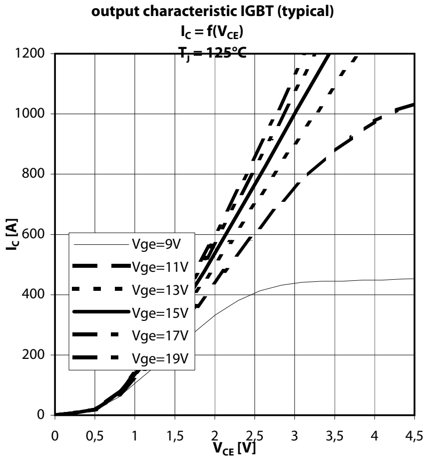

(a)

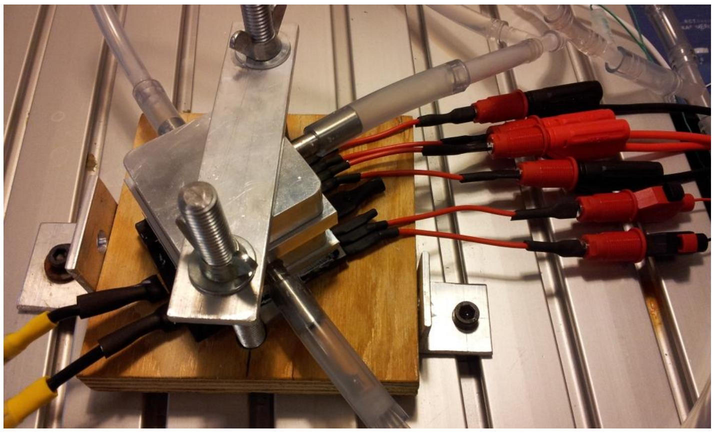

(b)

Figure 7.1: *Relationship between voltage and current at different gate voltages (left), and electric setup of IGBT power module (right).*

The gate opens at a minimum voltage of 6.5 V and with a current of 9.6 mA [Stroebel, 2012]. This is called the threshold voltage. Between 0 V and the maximum threshold voltage, $V_{GE(th)}$, the gate in the transistor acts as a variable resistance. This makes it possible to increase the resistance of the transistor and hereby increase the voltage drop over the IGBT and lower the current flow. Figure 7.1 (a) shows the tendency that the resistance decreases with a higher gate voltage. In the experiment the gate voltage is set to 6.6-6.8 V, which corresponds transistor resistance of approximately 0.75 Ω. With this resistance the transistor voltage and current is approximately 15 V and 20 A respectively, which corresponds to a dissipated power of 300 W. It was not possible to increase the dissipated power, without failure of the IGBT power module. In figure 7.1 (b) the electric setup of the IGBT power module is shown.

7.4 Equipment

The equipment used in the experiment is listed below:

- 2 pumps in series.
- Flow sensor from RS (0.2-10 $^{l}/_{min}$).
- Differential pressure transmitter from HUBA Control (0 - 0.6 bar).
- Thermocouples type K.
- NI cRIO-9074 with the following NI modules:
    - NI 9211 thermocouple input module.
    - NI 9219 analog input universal module.
    - NI 9401 digital I/O module.
- Power supplies: 20 V-2 A, 70 V-22 A, and a 45 V-140 A.
- Labtop Lenovo Thinkpad T61.

Each module in the NI cRIO-9074 chassis is found automatically by the scan engine software embedded in the NI cRIO-9074. Each module is configured to measure specific variables.

7.4.1 Calibration of Thermocouples

For the temperature measurement a total of three type K thermocouples are used with the NI 9211 module for data logging. The thermocouples have been calibrated using an electric water heater and a thermometer. The output voltage of the thermocouples is measured and associated with a temperature. In figure 7.2 the calibration curve for the three thermocouples is shown.

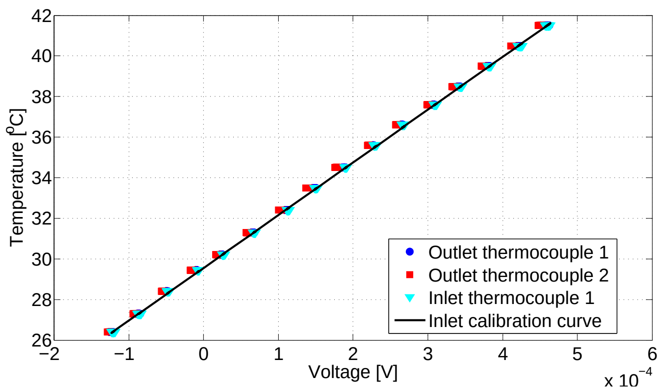

Figure 7.2: *The calibration measurements for the three thermocouples. The blue line represents the calibration curve for the inlet thermocouple.*

It is seen from figure 7.2 that the three thermocouples have very similar calibration data, which leads to similar calibration curves. This is expected, because the thermocouples are much alike. The blue line in figure 7.2 represents the calibration curve for the inlet thermocouple which is given as:

$$T = 25,988 \cdot U + 29.56 \qquad [K] \tag{7.1}$$

The calibration fits for the two other thermocouples are similar, and are not shown here.

7.4.2 Calibration of Flow Sensor

The flow sensor output is a number of pulses corresponding to a specific flow, thus the NI 9401 module is used for data logging. To find the relationship between pulses and flow rate, the pump is operated at various voltages and the flow is poured into a volumetric flask, and the time and pulses are recorded at the same time. This is done two times before the experiments, and one time after the experiment to ensure a correct calibration. The flow is varied between 0.5 and 4.5 $^{l}/_{min}$ for each of the calibration series. The flow rates versus pulse frequencies are shown in figure 7.3. The used calibration curve for the data treatment is an average of the three curves shown in figure 7.3.

The used linear fit between the measurements is hence given by:

$$\dot{V} = 0.0455 \cdot f_{pulse} - 0.0156 \qquad \left[\frac{l}{min}\right] \tag{7.2}$$

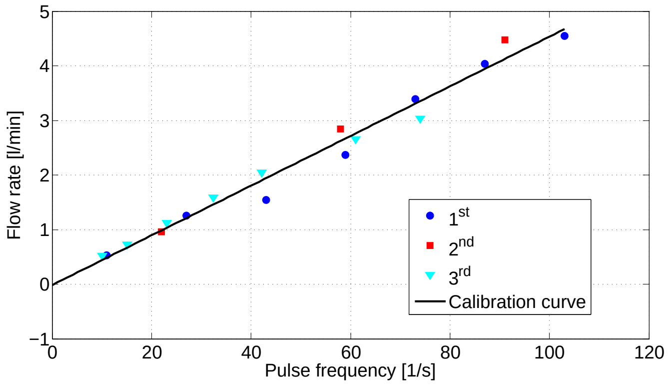

Figure 7.3: *Flow rate versus pulse frequency for flow sensor.*

7.4.3 Thermistor

The thermistor in the IGBT power module is used to measure the temperature inside the IGBT power module, using the fact that the resistance of the thermistor changes with temperature. The NI 9219 module is able to measure resistance directly and is used for the data logging. The resistance of the thermistor decreases with an increasing temperature. By measuring the resistance the temperature of the thermistor, $T_{thermistor}$, is found by the following equation [Vishay, 2009]:

$$T_{thermistor} = \frac{1}{\frac{ln(\frac{R_{thermistor}}{R_0})}{B} + \frac{1}{T_0}} \qquad [K] \tag{7.3}$$

Where the constant B is 3700 K for the thermistor used [Vishay, 2009]. R_0 is the resistance of the thermistor at T_0, which is 15 $k\Omega$ at 298.15 K for this thermistor. The thermistor characteristic is shown in figure 7.4 (a). The NI 9219 module is able to measure a maximum of 10.5 $k\Omega$ which corresponds to a temperature of approximately 33 $°C$. This means that only a thermistor temperature above approximately 33 $°C$ can be measured. This resistance is measured by the first channel, CH0. The calculation of the temperature in LabVIEW is shown in figure 7.4 (b).

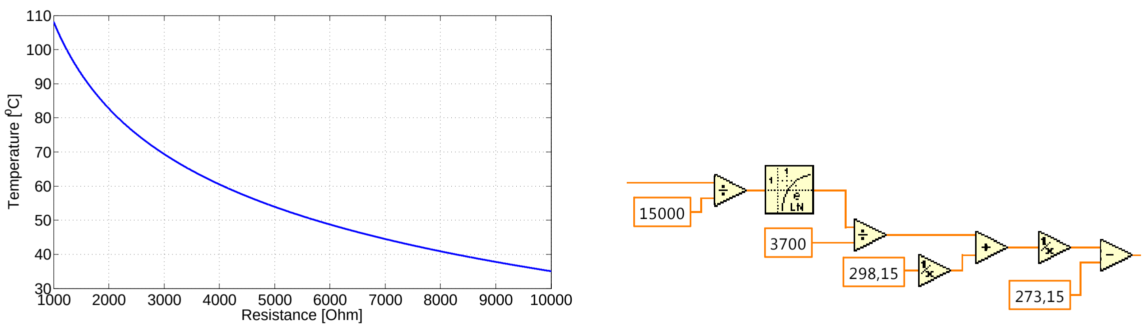

(a) (b)

Figure 7.4: *(a) Thermistor characteristics and (b) calculation of thermistor temperature in the target LabVIEW program.*

7.4.4 Differential Pressure Transducer

To measure the pressure difference over the cooling designs a differential pressure transducer, Huba Control type 692, is used. The output is a current signal between 4 and 20 *mA*, thus the NI 9219 module is used for data logging, as it is able to measure current. This current corresponds to a linear pressure difference between 0 and 0.6 *bar*. The channel CH1 is set to measure the current from the pressure transducer. The accuracy of the measurement is 0.7 % of the measurement [Huba Control, 2012]. The pressure transducer is trusted, and hence chosen not to be calibrated.

7.5 Experimental Setup

The setup of the flow system is shown in figure 7.5 (a) and (b). The same equipment setup is used for both the hybrid and multijet design. From the pump and following the flow direction, the first measurement takes place at FT1 (flow transmitter 1). The next measurement takes place at TT1 (temperature transmitter 1), which is the inlet temperature. Close to the cooling module a PDT1 (pressure differential transmitter 1) measures the differential pressure across the inlet and one outlet. The pressure in each of the outlets is assumed to be the same. Next, the outlet temperature in each outlet side is measured.

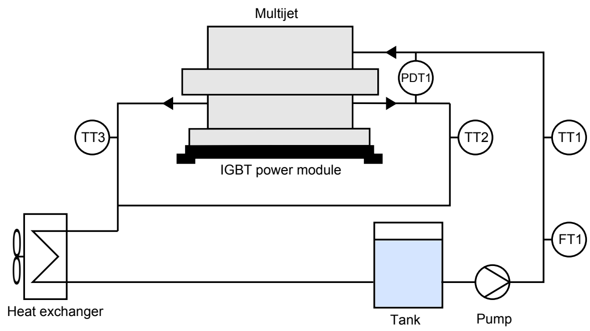

(a)

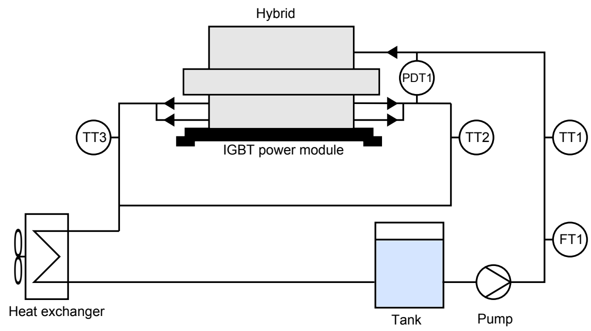

(b)

Figure 7.5: *Schematic of experimental setup for (a) multijet, and (b) hybrid design.*

The coolant is cooled in a heat exchanger before it enters a storage tank. In figure 7.6 a picture from the laboratory is shown. The cold plate in this picture is the multijet design. In this picture the heat exchangers, pressure transmitter, flow sensor, pump, storage tank, and thermocouples are seen.

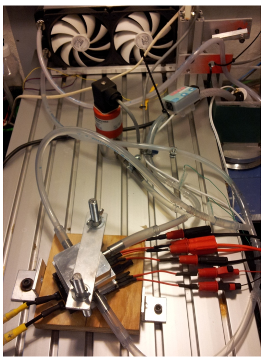

Figure 7.6: *Picture of multijet design experiment.*

7.6 Data Acquisition

The data acquisition is performed by a LabVIEW project containing a host file run on the host PC, that being the T61, and a target file running on the NI cRIO-9074. For every measured variable there is created a global variable containing the data. Furthermore a global variable is created for the stop function. The front panel of the target program is shown in figure 7.7 (a), and the front panel of the host program is shown in figure 7.7 (b).

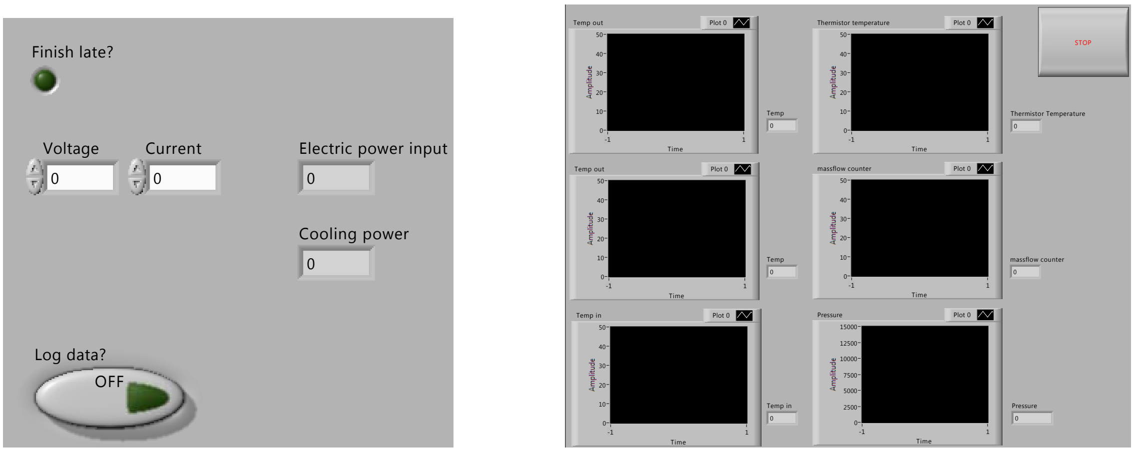

(a) (b)

Figure 7.7: Front panels of the programs used to acquire data from the experiments. Figure (a) shows the target front panel and (b) shows the host front panel.

The data logging is made by the NI cRIO-9074 and the T61 is used to monitor the measured variables. By doing this, the NI cRIO-9074 will continue logging if the connection to the T61 should be lost. The block diagram of the host program is shown in figure 7.8. The global variables are read and then shown in graphs and numeric indicators. All this happens in a while loop, which runs every 10 ms. From this program the stop function is also controlled.

The overall target program is shown in figure 7.9. In the target program all measured variables are imported from the modules. The variables are saved both as raw data and calculated data with the calibration curves. The logging is controlled by a case structure, shown in figure 7.10 (a), which is controlled by a boolean control in the host front panel.

The format of the saved numbers is defined by the string "%.;%.3f". "%.;" specifies that the decimal seperator used is a dot. "%.3f" specifies a floating point notation with a precision of three decimals. The numbers in the saved document is seperated by a tab. With these inputs it is possible to import the data directly into MATLAB for data processing. Overall a timed loop is used to control when the measurements are taken. The period between every loop is set to 1000 ms.

For all thermocouples the module is set to return the raw voltage signal. This is done in order to be able to calibrate the thermocouples after the experiment. The cooling power found from the temperature measurements, is logged along with the other data. The cooling power is calculated with equation (7.4). The calculation in LabVIEW is shown in figure 7.10 (b).

$$\dot{Q} = \dot{m} \cdot c_p \cdot (T_o - T_i) \qquad [W] \tag{7.4}$$

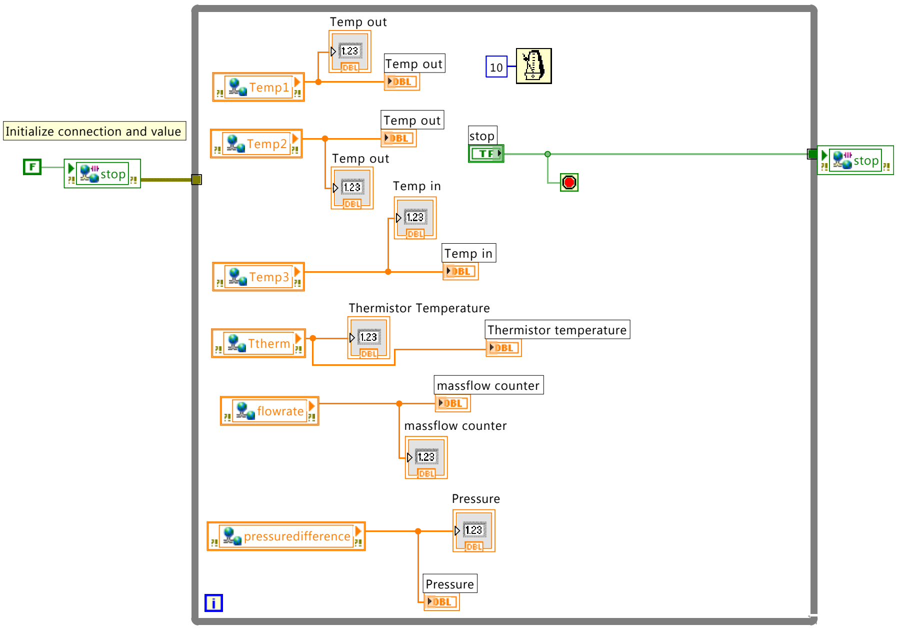

Figure 7.8: Block diagram of the host program.

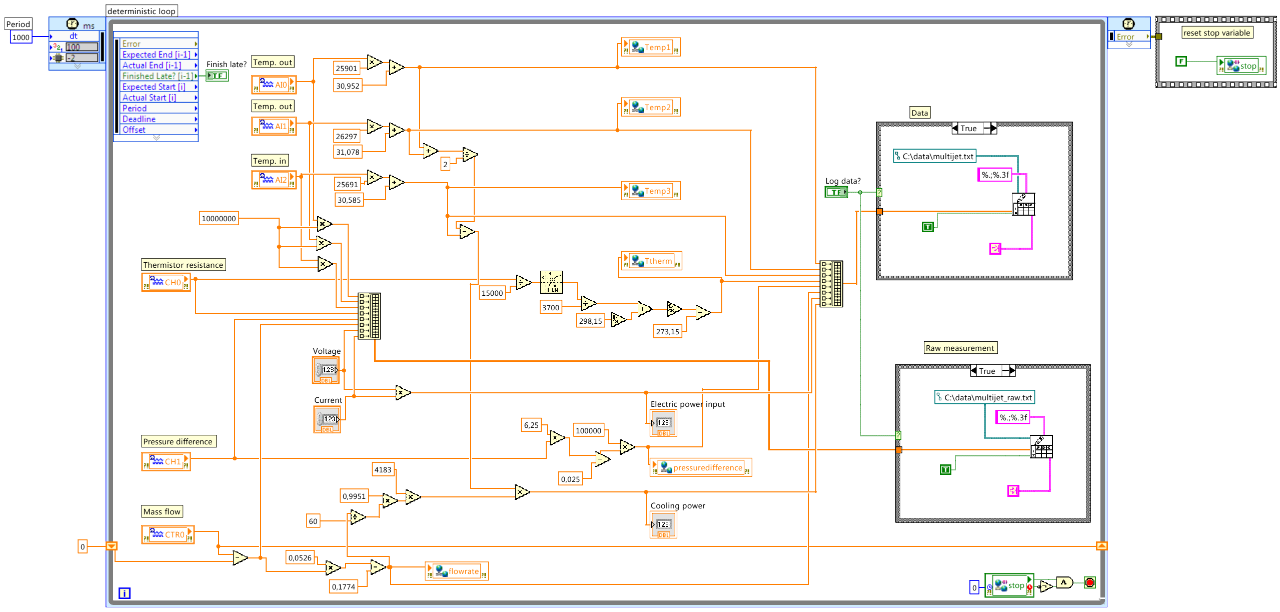

Figure 7.9: Block diagram of the target program.

To calculate the volume flow from the flow sensor every pulse from the sensor is counted. For every iteration in the timed loop a number from the counter is saved. By using a shift register the count from the previous iteration is subtracted from the current value, and the difference is used to calculate a volume flow from the calibration equation (7.2). This is possible since the time between each iteration is set to be one second and the difference will thereby correspond to a frequency. The calculation is shown in figure 7.11.

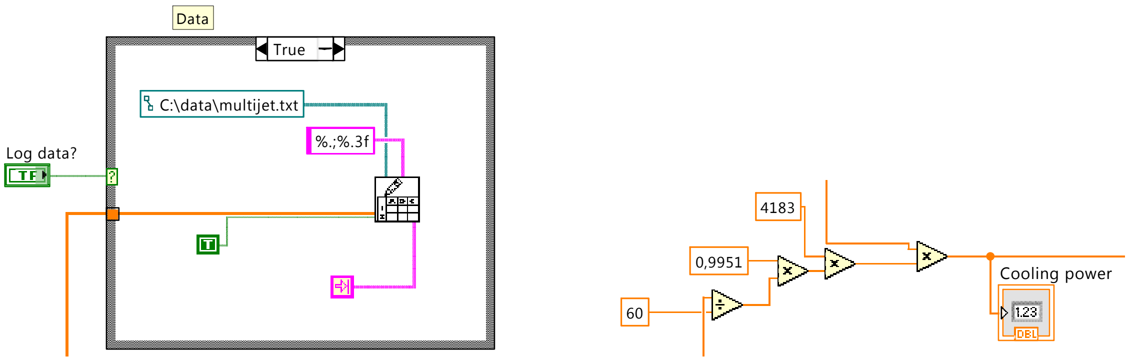

(a) (b)

Figure 7.10: *Case structure controlling the data logging (a), and calculation of cooling power (b).*

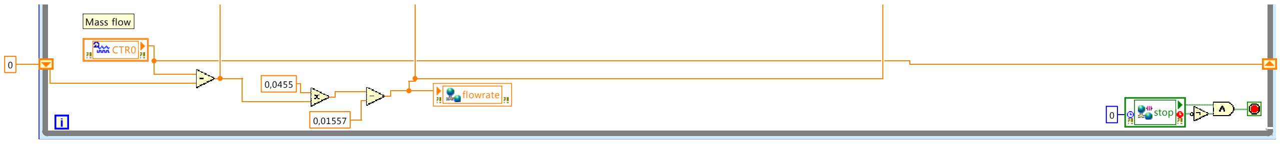

Figure 7.11: *Calculation of the volume flow.*

7.6.1 Source of Errors

The confidence interval for the mean population of the different measurements are found by equation 7.5:

$$\mu = \bar{x} \pm \frac{\sigma \cdot z}{\sqrt{n}} = \bar{x} \pm \delta \tag{7.5}$$

μ is the population mean, n is the number of samples, $\bar{x}$ is the arithmetic average, σ is the standard deviation, and z is the upper critical value, and is 1.96 for a standard normal distribution with a 95 % confidence interval [Walpole et al., 2007].

The standard deviations for the different measurements is shown in table 7.1. The standard deviations for temperatures are in general larger for the temperature differences at a low flow rate, and for the pressure measurements the standard deviations are in general seen to increase at higher flow rates. This might be caused by a low number of samples.

	Hybrid				**Multijet**		
Flow rate $[^l/_{min}]$	**0.54**	**1.04**	**1.78**	**2.21**	**1.54**	**2.77**	**4.04**
Standard deviation of $T_o - T_i$ $[K]$	0.16	0.06	0.07	0.04	0.06	0.02	0.02
Standard deviation of $T_{therm} - T_i$ $[K]$	0.68	0.07	0.09	0.1	0.46	0.22	0.07
Standard deviation of pressure $[Pa]$	133	437	350	545	249	186	416

Table 7.1: *Standard deviations for hybrid and multijet design.*

Besides the deviations in the population means there are also uncertainties presented in the measurements devices. An overview of these values is shown in table 7.2.

Device	**Uncertainty [%]**
Differential pressure transmitter	0.7
Thermocouple type K	0.75 times the temperature
Flow rate	1 (of full scale deflection)
Thermistor	2

Table 7.2: *Uncertainties in equipment used in the experiment.*

Other sources of errors in the experiment are:

- The thickness and smoothness of the thermal interface material between the IGBT power module and the cold plate may differ from the multijet design to the hybrid design.
- Electrical noise in general in the laboratory, as this could cause the measurements to differ.
- Steady state is not reached in the experiment. Instead the difference between the inlet and the thermistor temperature are used in the data treatment.
- The ambient temperature in the laboratory may have varied during the experiments.
- The temperature of the cooling water is different for all of the measurements which gives different thermodynamic properties, such as the thermal conductivity and the viscosity. This may influence the results when the design performance is to be evaluated.

7.7 Results and Discussion

Overall the designs show good cooling capabilities at the given input power. Average values for the experiments are presented in table 7.3 for the hybrid design. The pressure in the last measurement point in table 7.3 exceeded the range of the pressure transducer and is not taken into account. The inlet temperatures differs between the measurements series, so the important thing to notice is the difference between the inlet temperature and the thermistor temperature. This difference is seen to decrease with an increasing flow rate, while the pressure loss increases.

Flow rate $[{}^{l}/_{min}]$	**0.54**	**1.04**	**1.78**	**2.21**	**2.74**
T_o $[°C]$	34.5	37.6	38.6	39.0	39.4
T_i $[°C]$	29.3	34.6	36.6	37.3	38.1
$T_o - T_i$ $[°C]$	5.2	3.0	2.0	1.7	1.3
$T_{thermistor}$ $[°C]$	36.7	38.4	39.0	39.2	39.4
$T_{thermistor} - T_i$ $[°C]$	7.4	3.8	2.4	1.9	1.3
Δp $[Pa]$	5490	12,853	31,769	43,103	-
Pumping power $[W]$	0.05	0.22	0.94	1.59	-

Table 7.3: *Measurements from the experiment with the hybrid design.*

Table 7.4 shows the results for the multijet design. The tendencies are the same as for the hybrid design, but the temperature differences between the thermistor and inlet is larger for the multijet. This indicates a lower cooling performance of the multijet at similar pumping powers.

A total of three measurements is made for the multijet design corresponding to Reynolds numbers in the jet of approximately 2000, 4000 and 6000. In order to reach higher Reynolds numbers a bigger pump would be

Flow rate $[l/min]$	**1.54**	**2.77**	**4.04**
T_o $[°C]$	35.5	38.2	39.6
T_i $[°C]$	31.4	35.1	37.0
$T_o - T_i$ $[°C]$	4.1	3.0	2.6
$T_{thermistor}$ $[°C]$	43.3	41.2	41.0
$T_{thermistor} - T_i$ $[°C]$	11.9	6.1	4.0
Δp $[Pa]$	3804	10,406	21,159
Pumping power $[W]$	0.098	0.48	1.42

Table 7.4: *Measurements from the experiment with the multijet design.*

required, since the pumps are limited by the current limit from the power supply in order to reach a higher flow rate. The energy balances from the experiment is shown in table 7.5 for both the hybrid and the multijet design. The input power should always be higher than the energy absorbed by the water due to heat losses to the surroundings. This is seen to be the case for all the experiments, where the heat loss is between 61 W and 86 W.

	Hybrid					**Multijet**		
Flow rate $[l/min]$	**0.54**	**1.04**	**1.78**	**2.21**	**2.74**	**1.54**	**2.77**	**4.04**
$P_{electrical}$ $[W]$	295	297	297	297	297	285	287	288
$P_{cooling}$ $[W]$	218	218	227	236	234	200	204	202
Heat loss $[W]$	78	79	70	61	63	85	83	86
Heat loss [%]	26.4	26.6	23.6	20.5	21.2	29.8	28.9	29.9

Table 7.5: *Energy balance for the hybrid and the multijet design experiments.*

The heat loss is distributed between:

1. Natural convection from the outer surfaces of the cooling device.
2. Radiation to the surroundings.
3. Heat transfer to the wooden block which the IGBT power module is mounted to.
4. Heat loss in the electric wires, which became quite hot during the experiments.
5. Heat loss in pipes.

There might be errors in the temperature measurements, as there is a heat loss in the pipes, and thus a temperature profile in the pipes exists. This may induce problems when making point measurements. This is because the thermocouples are mounted in tee branches with somewhat different positions in the tee branches.

In the following figures a 95 % confidence interval for the results, together with the uncertainties in the measurements devices, are shown. In figure 7.12 the pressure loss for the different flow rates are shown for both designs. In both cases the pressure loss increases when the flow rate increases, and it is seen that the pressure loss is highest for the hybrid design at the same flow rate compared to the multijet design. This is probably due the smaller diameter in the inlet tubes than for the multijet design, and the presence of mini channels in the design.

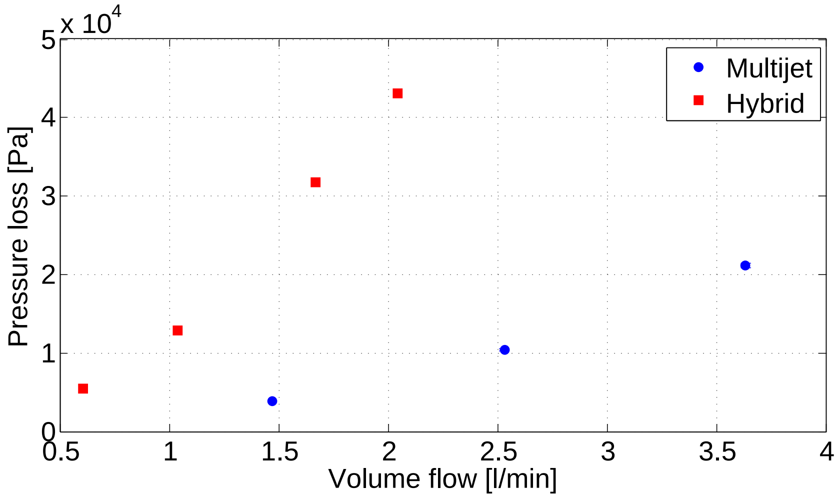

Figure 7.12: *Pressure loss measured in experiment as a function of flow rate for both designs.*

Figure 7.13 shows the difference between the outlet and inlet temperature drops when the flow rate increases. The errorbars in this figure are relatively large, but the limits also include the combined sum of the uncertainties for both the inlet and outlet temperature.

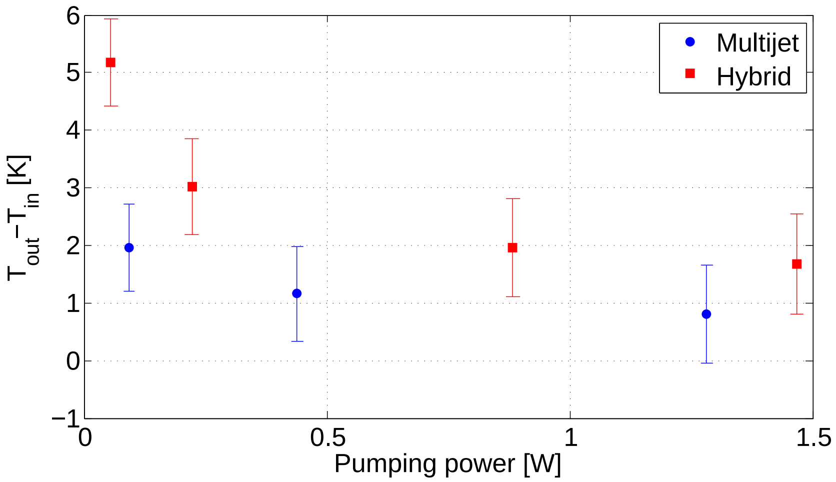

Figure 7.13: *Difference between the outlet and inlet temperature as a function of pumping power.*

Figure 7.14 shows the difference between the thermistor temperature and the inlet temperature. Since the cooling fan on the experimental setup is to small to keep the inlet temperature constant, this difference is shown instead. Hence, this should be a measure of the decreasing thermistor temperature with increasing flow rate. It is seen in the figure that the difference as expected decreases with an increasing flow rate as well. The hybrid design is in this case seen to be superior with a lower temperature difference compared to the multijet design at the same size of pumping power.

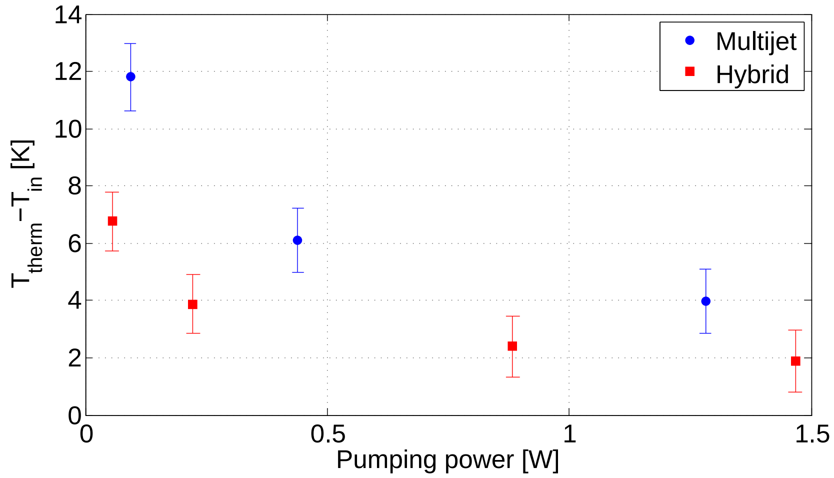

Figure 7.14: *Difference between thermistor temperature and inlet temperature versus pumping power.*

7.8 Experiment Conclusion

The cooling ability of the designs are seen to be successful in this experiment. In the experiment the heat exchanger is to small to reach steady state in the measurements. If the experiment is to be made again, steady state should be ensured.

In the experiment the hybrid design is seen to have a better cooling performance compared to the multijet design with regards to low junction temperature. Even though the electric input power was 10-12 *W* higher in the experiments with the hybrid design, the differences between the thermistor and inlet temperature are still seen to be the lowest. One of the reasons for this is the bottom plate for the multijet design, which is 4 *mm* compared to the 2 *mm* bottom plate of the hybrid design. This yields a higher thermal resistance for the multijet design for the base plate. This influences the thermistor temperature, but it is a demand from the workshop that the base plate of the multijet design is 4 *mm* thick due to the ability to have tight seal with an O-ring. The thermistor temperature is not the same as the junction temperature, as the junction temperature will be significantly higher than the thermistor temperature due to the thermal resistance from the thermistor to the junction.

With regards to the pressure loss the hybrid design has higher values compared to the multijet design. But as this is not a good stand alone parameter for evaluating the performance of the design, the pumping power is evaluated, and the pumping power is shown to be in the same range for both designs. Thus comparing the designs with regards to junction temperature, the hybrid design is recommended due to the best cost-effectiveness, based on this experiment.

Validation of CFD Through Experiments

8

In this chapter it is investigated if the CFD simulations can be validated through the experiments. Firstly the pressure losses are compared, and secondly the temperatures are compared. In the end of the chapter the validity is discussed. The following sections are included:

8.1 Validation of Pressure Loss

The pressure loss in the CFD simulations is found between the inlet of the jets and the outlet, as shown in figure 8.1 (a). When comparing the CFD simulations with the experiment, some assumptions are made. The pressure loss of the cooling designs in the experiments are found by measuring the pressure loss with the design mounted, and then subtracting the pressure loss of flow through the tee branch seen in figure 8.1 (b). This is done because of the uncertainties of estimating the pressure loss in the pipes between the pressure measurement and the cooling device.

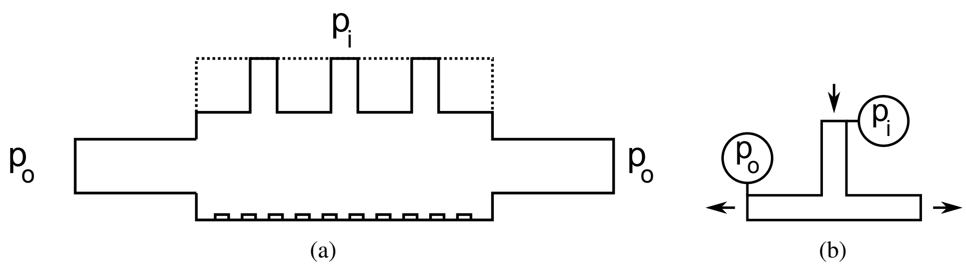

Figure 8.1: *Pressure loss calculated by CFD (a), and pressure loss measurement without design mounted using a tee branch (b).*

In table 8.1 the results for the hybrid design are shown, and in table 8.2 the results for the multijet design are shown. Comparing the hybrid and the multijet design, it is clear that the hybrid design induce higher pressure loss.

The pressure loss found by CFD does not include the inlet manifold and the piping for the inlet, as seen in figure 8.2 (a). The pressure loss in the inlet manifold is estimated in an analytical manner. In the following the Colebrook equation is used for the friction factor calculations for turbulent flow [Cengel and Cimbala, 2006]:

Flow rate [$^{l}/_{min}$]	Δp **with tee branch** [Pa]	Δp **with design mounted** [Pa]	Δp **of design** [Pa]
0.55	313	5490	5177
1.04	1175	12,853	11,678
1.87	1818	31,769	29,951
2.23	2378	43,103	40,725

Table 8.1: *Pressure loss of hybrid design found by experiment.*

Flow rate [$^{l}/_{min}$]	Δp **with tee branch** [Pa]	Δp **with design mounted** [Pa]	Δp **of design** [Pa]
1.4	910	3295	2385
2.74	3251	10,406	7,155
4.13	5712	21,159	15,447

Table 8.2: *Pressure loss of multijet design found by experiment.*

$$\frac{1}{\sqrt{f}} = -2.0 \cdot log\left(\frac{\varepsilon/D}{3.7} + \frac{2.51}{Re \cdot \sqrt{f}}\right) \tag{8.1}$$

The pressure loss in pipes (major loss) is calculated by equation (3.17).

The minor losses, which include fittings, bends, tees, enlargements, contractions etc., are characterized by [Cengel and Cimbala, 2006]:

$$\Delta p = K_L \cdot \rho \cdot \frac{V^2}{2} \tag{8.2}$$

The pressure loss considered is the inlet tube, the sharp-edged inlet to the box, and slightly rounded inlets to the jets. Along with this the piping for connecting the outlets for the hybrid design is also considered. The loss coefficient for the minor losses induce some uncertainties, especially for the jet, due to the estimation of the slightly rounded inlet, as shown in figure 8.2 (b) and (c).

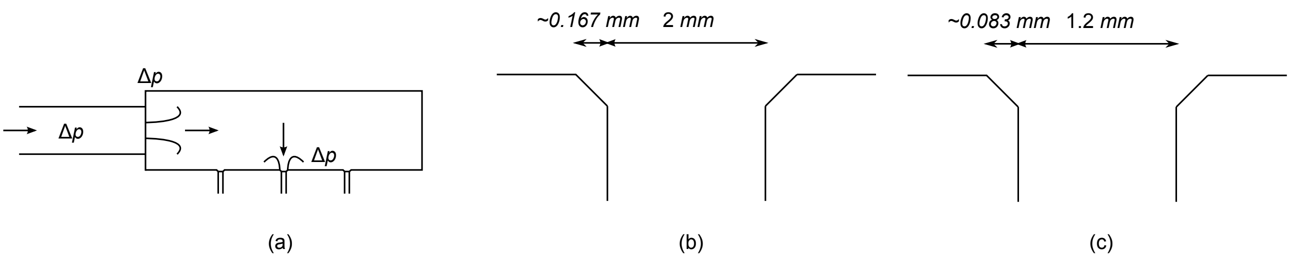

Figure 8.2: *Pressure loss estimation in (a) inlet manifold for (b) multijet design and (c) hybrid design.*

In table 8.3 the calculated pressure losses for the multijet design are shown. The pressure loss found in the experiment compared to the pressure loss in the CFD matches quite accurately, as seen in the last column in table 8.3.

The left hand side of figure 8.3 shows the values found in table 8.3. For the measured pressure loss the 0.7 % uncertainty of the differential pressure transducer is shown with an errorbar along with the standard deviation of the measurement found in section 7.6.1. The deviation between CFD and the measured pressure loss is

Flow rate [$^l/_{min}$]	Δp **analytical part** [Pa]	Δp **CFD** [Pa]	Δp **experiment - analytic** [Pa]	Δp **error** [Pa]
1.4	1606	709	779	70 (9 %)
2.74	5003	2065	2152	87 (4 %)
4.13	11,329	4305	4118	-187 (4.5 %)

Table 8.3: *Pressure loss of multijet design comparing CFD and experiment.*

noticable, but accounting for simulation uncertainties and pressure loss calculation uncertainties, the result is satisfactory.

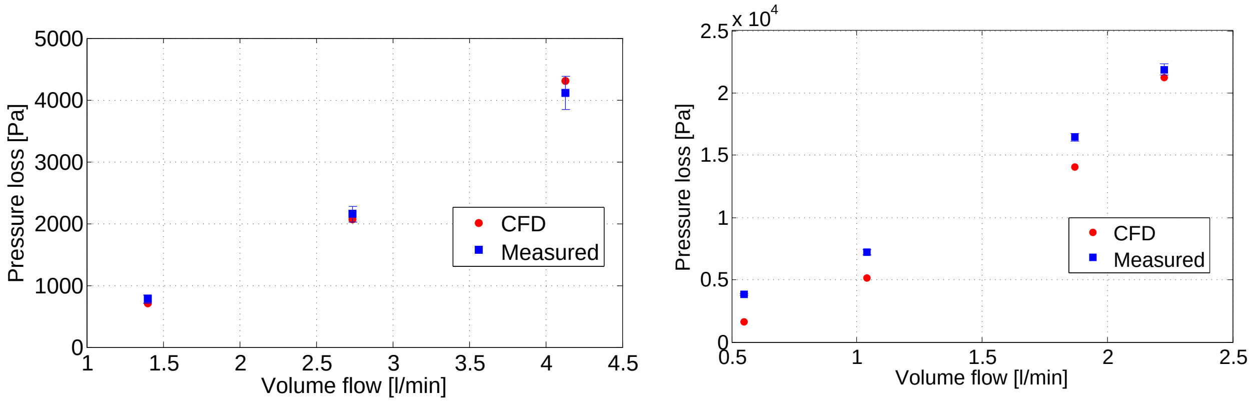

(a) (b)

Figure 8.3: *Pressure loss in multijet from experiment and CFD (left), and pressure loss in hybrid design from experiment and CFD results (right).*

In table 8.4 the pressure losses for the hybrid design is found. The pressure losses found in the experiment matches the CFD badly at the low flow rates, where the error at a flow rate of 0.55 $^l/_{min}$ is 58 % compared to the CFD, whereas it at a flow rate of 2.23 $^l/_{min}$ is 3 % compared to the CFD. The error at the low flow rates may be contributed by the analytical pressure loss calculation in the manifold, where it for the hybrid design is difficult to estimate a pressure loss due to somewhat arbitary flow bends of the tubes, and the assumption of $^1/_4$ flow rate in each of the four outlets.

Flow rate [$^l/_{min}$]	Δp **analytical part** [Pa]	Δp **CFD** [Pa]	Δp **design - inlet** [Pa]	Δp **error** [Pa]
0.55	1366	1604	3811	2207 (58 %)
1.04	4459	5143	7219	2076 (29 %)
1.87	13,513	14,054	16,438	2384 (14.5 %)
2.23	18,838	21,244	21,887	643 (3 %)

Table 8.4: *Pressure loss of hybrid design comparing CFD and experiment.*

In figure 8.3 (b) the values found in table 8.4 is shown. For the measured pressure loss the 0.7 % uncertainty of the differential pressure transducer is shown with an errorbar along with the standard deviation of the measurement found in section 7.6.1. The measured pressure loss lies over the CFD predicted pressure loss, but at the measurement with the highest flow rate the CFD lies within the errorbar of the measured pressure loss.

8.2 Validation of Temperature

For validation of the temperatures between the CFD and the experiment, several uncertainties are encountered. The IGBT power module is not part of the CFD geometry, and thus it is difficult finding the CFD based temperature compared to the thermistor temperature in the experiment. The thermal resistance in the power module between the IGBTs and the thermistor is not found, due to a discontinuity in the 2D heat diffusion issue, as shown in figure 8.4. Thus the resistance from the IGBT to the thermistor is not found. In addition to this, the heat losses to the surroundings are not included in the CFD simulations, thus the energy absorbed in the water differs from the experiment to the CFD simulations.

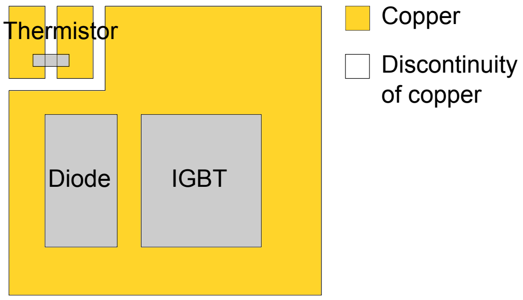

Figure 8.4: *Discontinuity of copper in IGBT power module.*

Because the IGBT power module is not a part of the geometry in the CFD, the temperature found in the same point as where the thermistor is located would not be the same between the experiment and the CFD. The thermistor temperature found in the experiment and the thermistor temperature found by using CFD should have the same temperature difference with regards to the inlet temperature at all volume flows tested. This difference, between the thermistor and inlet water temperature, will somewhat incorporate the uncertainties about natural convection, radiation etc., as these should have the same size. Figure 8.5 shows the position of the temperature evaluation on the CFD geometry. This corresponds to the same point in the IGBT power module, besides the presence of the materials in the IGBT power module shown in figure 4.4 on page 25.

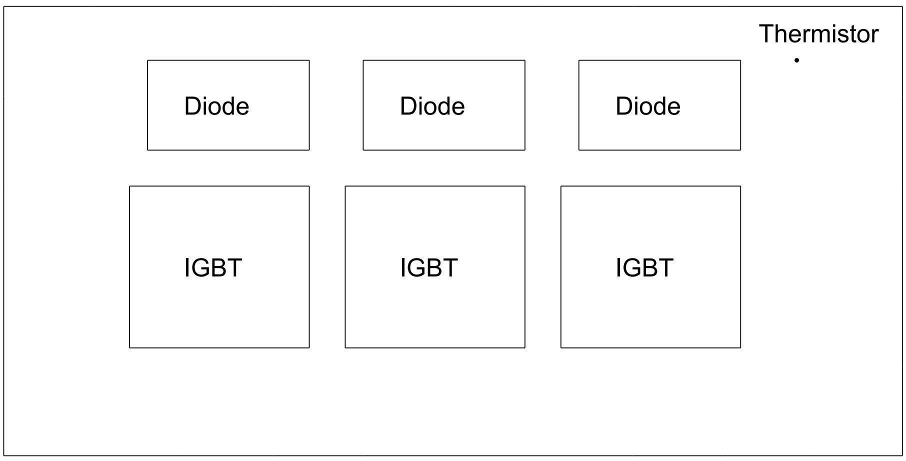

Figure 8.5: *Position of temperature evaluation on CFD geometry.*

Figure 8.6 shows the difference between the thermistor temperature and the inlet temperature for the hybrid design for both the experiment and the CFD. The difference between the experiment temperature differences and the CFD temperature differences should be the same for all volume flows, but this is not the case at the low volume flow, but the difference between experiment and CFD decreases as the volume flow increases, and at the measurement with the highest volume flow the CFD lies within the error bar of the experiment. The change in temperature difference correlates to the heat loss seen in table 7.5, where the tendency of high heat loss seems to correspond to a high difference between the CFD simulation and the experiment. If the heat loss is constant, the temperature differences between the CFD simulation and the experiment are more likely to be the same.

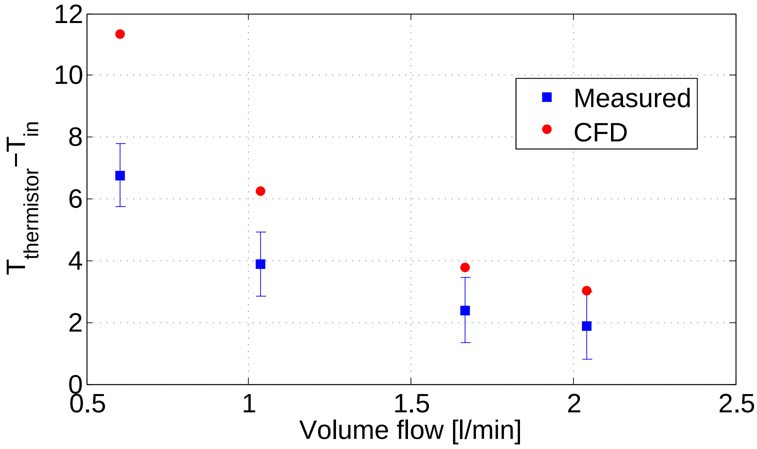

Figure 8.6: *Difference in thermistor temperature and inlet temperature for hybrid design for both experiment and CFD.*

Figure 8.7 shows the difference between the thermistor temperature and the inlet temperature for the multijet design for both the experiment and CFD. As for the hybrid design, the difference between experiment and CFD temperatures should be the same for all volume flows. From the figure the magnitude of the difference is similar for all volume flows, considering the errorbar of the measured value. The heat losses in this experiment are seen in table 7.5 to be constant, which helps having similar temperature differences between the CFD simulations and the experiment.

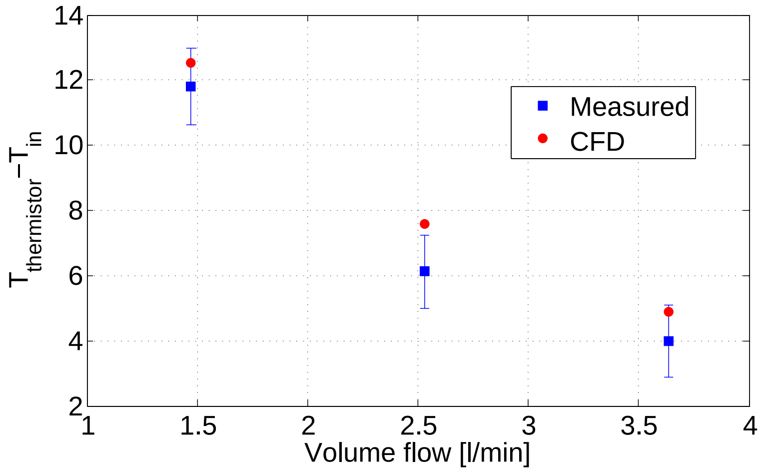

Figure 8.7: *Difference in thermistor temperature and inlet temperature for multijet design for both experiment and CFD.*

8.3 Discussion of Validity

Based on the two previous sections the validation of the CFD compared to the experiment is documented. The pressure loss difference of the hybrid design when comparing the experiment to the CFD shows a constant difference, except for the last measurement point. This difference may be contributed to the uncertainties of the analytic calculation of the pressure loss in the manifold and outlet tubes, which are not considered for the CFD.

The temperature difference for the hybrid design comparing the experiment to the CFD shows in figure 8.6 a difference that changes with volume flow. This is a problem towards validating the CFD at the low flow ranges, while at higher flow rates the use of CFD for the hybrid design can be validated. The use of CFD in the whole flow rate range is however still assumed to be reasonable, when taking the heat loss from the experiment into account.

The pressure difference of the multijet design in figure 8.3 (a) shows good correlation between the experiment and the CFD. All of the CFD evaluated pressure losses lie within the error bars of the measured pressure loss. Also the temperature differences for the multijet design comparing the experiment to the CFD shows an almost constant difference between the experiment and CFD. This validates the CFD at all the volume flows investigated.

Due to the concluded validity of the CFD simulations, it is considered reasonable to do CFD simulations with other inputs than now validated. Hence, it is considered reasonable to trust the CFD simulations when using glycol as coolant, as done when the cold plates are compared with Shower Power in chapter 6.7.

9 Conclusion

This report addresses the cooling problems of high heat flux electronics, where it in chapter 1 is found that high junction temperature and non uniform temperature distribution affects power electronics negatively. The important drawbacks are risk of higher failure rate and lower efficiency. Thus a cooling application giving low junction temperature and good temperature distribution is essential. It is decided to investigate single phase cooling on a Danfoss IGBT power module in order to reach two designs proposals.

The design concepts are in chapter 3 chosen to consist of jet impingement and/or mini channels. Jet impingement cooling is found to have several advantages including high local heat transfer and a relative low pressure loss. An optimal jet-to-target spacing of $5 \cdot D$ and an optimal jet-to-jet spacing of $8 \cdot D$ is found. Micro/mini channels are found to give high overall heat transfer, but with drawbacks of high pressure loss and risk of non uniform temperature in the direction of the flow. A discretized analytical model is developed in order to investigate the heat transfer in mini channels, and was found to have good temperature distribution as long as the flow rate is high. This was found to be in good agreement with a CFD analysis of the specific problem.

In chapter 4 the Danfoss power module, used in e.g. the Toyota Prius, is presented, where it is found that the required heat flux removal is in the order of 111.1 $^{W}/_{cm^2}$. For the specific IGBT power module a mismatch of thermal expansion coefficients of the various materials give problems with life time when dealing with non uniform temperature distribution.

Five design proposals is found in chapter 5. They are:

- Mini channels with bypass.
- Staggered fins with bypass.
- Staggered fins without bypass.
- Multijet on a rough surface.
- Hybrid between jet impingement and mini channels.

The multijet and hybrid design are chosen to be manufactured and tested for heat transfer performance, and all five designs are simulated using CFD. For mesh generation both ANSYS GAMBIT and ANSYS Meshing is used, where both structured and unstructured meshes are made. The results show by comparison that the multijet and hybrid designs are superior to the mini channels and staggered fins design, where the highest convective heat transfer coefficient is found to be in the vicinity of 20,000 $^{W}/_{m^2\,K}$ for the multijet design. The hybrid and multijet design show good temperature distribution. The manufactured designs are compared against Shower Power, which shows that the hybrid and multijet design gives higher h-values than Shower Power at high pumping power values, where the gradient of the curve with h-values against pumping power decays faster for Shower Power than for the multijet and hybrid designs.

In chapter 7 the cooling performance experiment is documented, where it is succeeded to cool an electrical input power of approximately 300 W. Flow rate and temperature are measured for energy balance, and the differential pressure loss, between inlet and outlet, of the designs is measured. The measurements show good coherence with expectations. 60-85 W is lost to the surroundings in the experiments. The best cooling design is concluded by the experiment to be the hybrid design due to lowest thermistor to inlet temperature difference.

Comparing the experiment and the CFD simulations, it is seen that the CFD simulations with the multijet design predicts the cooling performance and the pressure loss with good coherence. The CFD simulations with the hybrid design shows the same tendencies as the experiment.

In table 9.1 a rating of the performance for each of the designs is made. The ratings are relative with regards to each other, and a one star is given for a poor performance while four stars are given for an excellent performance. Thus, the more stars the better, and for the pressure loss this indicates that many stars give a low pressure loss.

Design	T_{max}	**Temperature uniformity**	***h*-value**	**Pressure loss**	**Mass flow**
Mini channels	⋆	⋆⋆	⋆	⋆⋆⋆	⋆⋆
Staggered fins (bypass)	⋆	⋆	⋆	⋆⋆⋆	⋆⋆
Staggered fins (no bypass)	⋆⋆	⋆⋆	⋆	⋆⋆⋆	⋆⋆
Multijet	⋆⋆⋆	⋆⋆⋆⋆	⋆⋆⋆⋆	⋆⋆⋆	⋆⋆
Hybrid	⋆⋆⋆⋆	⋆⋆⋆⋆	⋆⋆⋆	⋆	⋆⋆⋆⋆
Shower Power	-	⋆⋆⋆⋆	⋆⋆⋆	⋆⋆⋆⋆	⋆⋆

Table 9.1: *Rated performance for various cold plate designs.*

From this table it is shown that the rated performance is best for the hybrid design with regards to the maximum temperature. The multijet performs slightly poorer, primarily due to the thicker base plate of the cold plate. For the other designs the performance is only given one-two stars, while for the Shower Power design this performance is unknown. The temperature uniformity is rated as excellent for the hybrid, multijet, and Shower Power, while it is lower for the three other designs due to the poor flow distribution in the manifold. The h-value is rated highest for the multijet design, while the hybrid and Shower Power is right behind with three stars.

The results are made for the same range of pumping power for the cold plates designed in this project, hence the pressure and mass flow ratings has to be taken into account at the same time. If the pressure loss is high, as for the hybrid design, then the mass flow rate is correspondingly lower. Hence the hybrid design gets four stars in the mass flow category. For the Shower Power module the pumping power range is lower, hence making it possible the rate this design differently, and giving it six stars combined for pressure loss and mass flow rate.

Based on the above considerations the hybrid design is chosen as the best design made in this project. This design gives the lowest maximum temperature, while having a high temperature uniformity, and the pumping power range to achieve this is in the same as the multijet design. If the hybrid design has to be made commercial available the manufacturing cost has to be minimized, as this is in this area where Shower Power design has its big advantage and is superior the hybrid design.

10 Further Work

The manufactured designs are prototypes and are constrained by the departments workshop. For commercialization the designs must be cheaper and easier to manufacture. This may be possible due to a considerable amount of the design that could be manufactured in hard plastic, possibly melamine priced 1.6 $^{\$}/_{kg}$ [Strathearn, 2012], where as the price for aluminium is 2 $^{\$}/_{kg}$ and copper is 8 $^{\$}/_{kg}$ [Metalprices, 2012]. Due to the density of melamine of 1574 $^{kg}/_{m^3}$ compared to the density of copper of 8933 $^{kg}/_{m^3}$, and the density of aluminium of 2702 $^{kg}/_{m^3}$, the weight of the designs when using plastic would be lower [Cengel, 2006].

The inlet box and the jet plates along with the sides of the multijet design could be made of plastic, as they are not directly a part of the heat transferring material. For further improvement of the designs, the heat transferring material could be copper, as this lowers the thermal resistance and thus lower the junction temperature due to higher conductivity of copper than aluminium. For commercialization a life time test of the design should be investigated, due to possible problems with a high impulse caused by the jets on the target plate.

For further investigation of the designs, particle image velocimetry (PIV) on the jets is interesting for validation of the CFD. It may be made for the multijet design, as the sides may be manufactured in perplex, making it possible to focus a laser in the fluid and to capture the particle movements by camera. Along with PIV, planar laser induced fluorescence (PLIF) is interesting for investigating the convective heat transfer coefficient. This method is used in the article in part II of this report. A transient CFD analysis is also interesting in order to e.g. investigate the stagnation zone for the jets.

The experiment was conducted with a heat input of 300 W, which for further work should be increased in order to test the cooling performance of the designs.

The multijet design is scalable for larger or smaller cooling modules as long as the jet-to-jet spacing of $8 \cdot D$ and jet-to-target spacing of $5 \cdot D$ is conserved. To investigate the scalability of the designs this could be modeled or experimentally tested.

Further work could also include investigation of two phase cooling due to several advantages of this. Due to the evaporation temperature, at constant pressure, the temperature will be constant everywhere boiling occurs, thus providing a uniform temperature in the fluid used for cooling. two phase cooling has a big potential for high h-value, as shown in table 3.2, and this could contribute to reduction in the cooling area.

Bibliography

Accuratus, **2002**. Accuratus. *Aluminum Oxide, Material Characteristics*. URL: `http://accuratus.com/alumox.html`, 2002. Accessed: 24.04.2012.

ANSYS, Inc, **2009**. ANSYS, Inc. *ANSYS FLUENT 12.0 - Theory Guide*, 2009.

Barrau, **2011**. Jérôme Barrau. *Numerical study of a hybrid jet impingement/micro-channel cooling scheme*. Applied Thermal Engineering, 33, 9, 2011.

Baumann, Lutz, and Wondrak, **2011**. M. Baumann, J. Lutz, and W. Wondrak. *Liquid Cooling methods for power electronics in an automotive environment*. IEEE Xplore, 2011.

Berlman, **1971**. I. B. Berlman. *Handbook of fluorescence spectra of aromatic molecules*. Academic Press, 1971.

Cengel, **2006**. Yunus A. Cengel. *Heat and Mass Transfer*. McGrawHill, 2006.

Cengel and Cimbala, **2006**. Yunus A. Cengel and John M. Cimbala. *Fluid Mechanics*. ISBN: 978-0-07-111566-7, International edition. McGraw-Hill, 2006.

Amarvir Chilka and Ashish Kulkarni, **2010**. Amarvir Chilka and Ashish Kulkarni. *Modeling Turbulent Flows in Fluent*. URL: `http://www.fluent.com/software/university/blog/turbulent.pdf`, 2010. Accessed: 07.12.2010.

Colgan, Furman, LaBianca, Magerlein, Polastre, Marston, and Schmidt, **2007**. E. G. Colgan, B. Furman, M. Gaynes N. LaBianca, J. H. Magerlein, R. Polastre, R. Benzema K. Marston, and R. Schmidt. *High Performance and Subambient Silicon Microchannel Cooling*. Journal of Heat Transfer, 129, 1046–1051, 2007.

Coolen, Kieft, Rindt, and Steenhoven, **1999**. M. C. J. Coolen, R. N. Kieft, C. C. M. Rindt, and A. A. van Steenhoven. *Application of 2-D LIF temperature measurements in water using a Nd:YAG laser*. Experiments in Fluids, 27, 420–426, 1999.

Danfoss, **2012**. Danfoss. *Cooling and Reliability Presentation*, 2012.

ERCOFTAC, **2000**. ERCOFTAC. *Best Practice Guidelines*. European Research Community On Flow, Turbulence And Combustion (ERCOFTAC), 2000.

Fluent Inc., **2005**. Fluent Inc. *Overview of Turbulence Modeling*, 2005. Fluent User Services Center.

Hanson, Seitzman, and Paul, **1990**. R. K. Hanson, J. M. Seitzman, and P. H. Paul. *Planar Laser-Fluorescence Imaging of Combustion Gases*. Applied Physics, 50, 441–454, 1990.

Holst, **2012**. Jørgen Holst. *Conversations with Jørgen Holst, Specialist, Thermal Design, Danfoss*, 2012.

Huba Control, **2012**. Huba Control. *Relative and differential pressure transmitter type 692*. Huba Control, 2012.

Idelchik, **1996**. I. E. Idelchik. *Handbook of Hydraulic resistance*. Begell House, 3rd edition, 1996.

Jun, Danling, Ping, and Hong, **2004**. Zheng Jun, Zeng Danling, Wang Ping, and Gao Hong. *An experimental study of heat transfer enhancement with a pulsating flow*. Heat transfer - Asian Research, 33, 279–286, 2004.

Kakac, Shah, and Aung, **1987**. S Kakac, R K Shah, and W Aung. *Handbook of Single-phase Convective Heat Transfer*. John Wiley & Sons, 1987.

Kandlikar and Bapat, **2007**. Satish G. Kandlikar and Akhilesh V. Bapat. *Evaluation of Jet Impingement, Spray and Microchannel Chip Cooling Options For High Heat Flux Removal*. Heat Transfer Engineering, 28, 911–913, 2007.

Kandlikar and Grande, **2002**. Satish G. Kandlikar and William J. Grande. *Evolution of microchannel flow passages - thermohydraulic performance and fabrication technology*. ASME International Mechanical Engineering Congress & Exposition, 2002.

Kandlikar and Hayner, **2009**. Satish G. Kandlikar and Clifford N. Hayner. *Liquid Cooled Cold Plates for Industrial High-Power Electronic Devices - Thermal Design and Manufacturing Considerations*. Heat Transfer Engineering, 30, 918–930, 2009.

Lavieille, Lemoine, Lavergne, and Lebouché, **2001**. P. Lavieille, F. Lemoine, G. Lavergne, and M. Lebouché. *Evaporating and combusting droplet temperature measurements using two-color laser-induced fluorescence*. Experiments in Fluids, 31, 45–55, 2001.

Lee, Garimella, and Liu, **2005**. Poh-Seng Lee, Suresh V. Garimella, and Dong Liu. *Investigation of heat transfer in rectangular microchannels*. International Journal of Heat and Mass Transfer, 48, 1688–1704, 2005.

Liu, Yang, Gan, and Luo, **2008**. Sheng Liu, Juanghui Yang, Zhiyin Gan, and Xiaobing Luo. *Structural optimization of a microjet based cooling system for high power LEDs*. International Journal of Thermal Sciences, 47, 1086–1095, 2008.

Long, Webber, and Chang, **1978**. M. B. Long, B. F. Webber, and R. K. Chang. *Instantaneous two-dimensional concentration measurements in a jet flow by Mie scattering*. Applied Physics Letter, 34, 22, 1978.

Lowe, **2009**. Kirk Townsend Lowe. *Direct Cooled Ceramic Substrate for Thermal Control of Automotive Power Electronics*. PhD thesis, 2009.

Martin, **1977**. Holger Martin. *Heat and Mass Transfer between Impinging Gas Jets and Solid Surfaces*, 1977.

Metalprices, **2012**. Metalprices. *Metal Prices on the Internet*. URL: `http://www.metalprices.com/`, 2012. Available: 20.04.2012.

Mudawar, 2005. Issam Mudawar. *Experimental and numerical investigation of single-phase heat transfer using a hybrid jet-impingement/micro-channel cooling scheme*. International Journal of Heat and Mass Transfer, 45, 2549–2565, 2005.

Olesen, 2012. Klaus Olesen. *Conversations with Klaus Olesen, Specialist, Thermal Design, Danfoss*, 2012.

Olesen, Bredtmann, and Eisele, 2006. Klaus Olesen, Rüdiger Bredtmann, and Ronald Eisele. *Shower Power New Cooling Concept for Automotive Applications*. Automotive Power Electronics, 2006.

Pantankar, 1980. Suhas V. Pantankar. *Numerical Heat Transfer and Fluid Flow*. ISBN: 0-89116-522-3, 1. edition. Hemisphere Publishing Corporation, 1980.

Parida, Ekkad, and Ngo, 2012. P. Parida, S. Ekkad, and K. Ngo. *Impingement-based high performance cooling configurations for automotive power converters*. International Journal of Heat and Mass Transfer, 55, 834–847, 2012.

Remsburg, 2007. Ralph Remsburg. *Nonlinear Fin Patterns Keep Cold Plates Cooler*. Power Electronics Technology, 2007.

Remsburg, 2001. Ralph Remsburg. *Thermal Design of Eletronic Equipment*. CRC Press, 2001.

Rohsenow, Harnett, and Cho, 1998. Warren M. Rohsenow, James P. Harnett, and Young I. Cho. *Handbook of Heat Transfer*. McGraw-Hill, 1998.

Shah and London, 1978. R. K. Shah and A. L. London. *Advances in Heat Transfer - Laminar Flow Forced Convection in Ducts*. Academic Press, 1978.

Solovitz and Mainka, 2011. Stephen A. Solovitz and Jeffrey Mainka. *Manifold Design for Micro-Channel Cooling With Uniform Flow Distribution*. Journal of Fluids Engineering, 133, 2011.

ST Microelectronics, 2002. ST Microelectronics. *D2PAK Reliability Data*, ST Microelectronics Reliability Report, 2002.

Stephan and Preusser, 1979. K. Stephan and P. Preusser. *Wärmeübergang und maximale wärmestromdichte beim behältersieden binärer und ternärer flüssigkeitsgemische*. Chem. Ing. Tech., 51, 37, 1979.

Helena Strathearn, 2012. Helena Strathearn. *Melamine pricing*. Reed Business Information Limited, URL: `http://www.icispricing.com/il$_$shared/Samples/SubPage127.asp`, 2012.

Stroebel, 2012. H Stroebel. *Technical Information for IGBT module*, Danfoss, 2012.

Sung and Mudawar, 2008. Myung Ki Sung and Issam Mudawar. *Single-phase and two-phase heat transfer characteristics of low temperature hybrid micro-channel/micro-jet impingement cooling module*. International Journal of Heat and Mass Transfer, 51, 3882–3895, 2008.

Terpetschnig, Povrozin, and Eichorst, 2012. Ewald Terpetschnig, Yevgen Povrozin, and John Eichorst. *Polarization Standards*. ISS, Inc, 2012. http://www.iss.com.

Inc. Toyota Motor Sales, U.S.A. Inc. Toyota Motor Sales, U.S.A. *Toyota Prius 2012 Performance and Specifications*. http://www.toyota.com/prius-hybrid/specs.html.

Tuckerman and Pease, 1981. D. B. Tuckerman and R. F. W. Pease. *High-Performance Heat Sinking for VLSI*. IEEE Electron Device Letters, 2, 126–129, 1981.

Versteeg and Malalasekera, 2007. H. K. Versteeg and W. Malalasekera. *An introduction to Computational Fluid Dynamics*. Pearson, 2007.

Vishay, 2009. Vishay. *SMD 0805 Glass Protected NTC Thermistors*, 2009.

Walpole, Myers, Myers, and Ye, 2007. Ronald E. Walpole, Raymond H. Myers, Sharon L. Myers, and Keying Ye. *Probability and Statistics for Engineers and Scientists*. ISBN: 0-13-204767-5, 1st edition. Pearson, 2007.

Webb, 1995. B.W. Webb. *Single-phase liquid jet impingement heat transfer*. Academic Press, Inc., 1995.

Jim Wilson, 2006. Jim Wilson. *Thermal Conductivity of Solders*. URL: `http://www.electronics-cooling.com/2006/08/thermal-conductivity-of-solders/`, 2006. Accessed: 24.04.2012.

Yin, 2010. Chungen Yin. *Numerical Fluid Dynamics*. Slideshow used for teaching about CFD at AAU, 2010.

Zhou, Zhang, Catano, Wen, Michna, and Peles, 2010. Rongliang Zhou, Tiejun Zhang, Juan Catano, John T. Wen, Gregory J. Michna, and Yoav Peles. *The steady-state modeling and optimization of a refrigeration system for high heat flux removal*. Applied Thermal Engineering, 30, 2347–2356, 2010.

Zorian and Gizopoulos, 2005. Yervant Zorian and Dimitris Gizopoulos. *Low-Power Electronics Design, chapter 46 - Chip Cooling: Why? How?* ISBN: 978-0-8493-1941-9, 1. Edition. CRC Press, 2005.

Zuckerman and Lior, 2006. N. Zuckerman and N. Lior. *Jet Impingement Heat Transfer: Physics, Correlations, and Numerical Modeling*. Advances in heat transfer, 39, 2006.

Pictures of Manufactured Designs

A

In this appendix the manufactured designs is shown. The manufactured multijet design is shown in figure A.1. In this picture the inlet manifold (lower left corner), perforated inlet plate, and the bottom base plate with squared fins are shown.

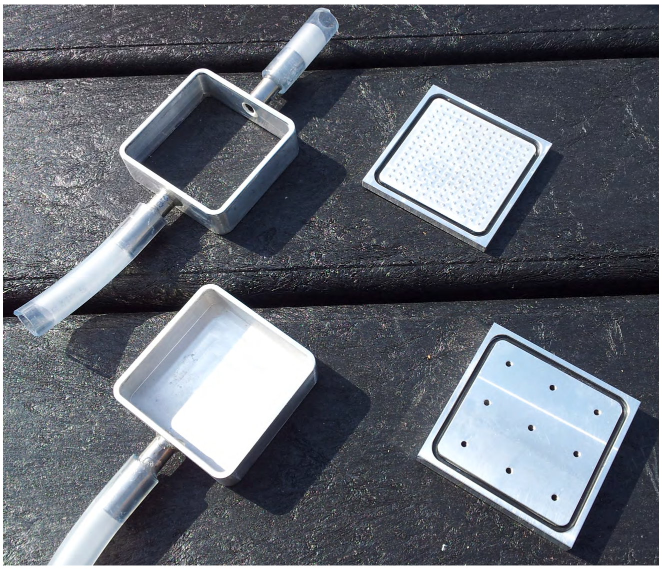

Figure A.1: *Multi jet design manufactured.*

In figure A.2 a zoomed in picture of the base plate with 0.5 *mm* high fins for the multi jet design is shown.

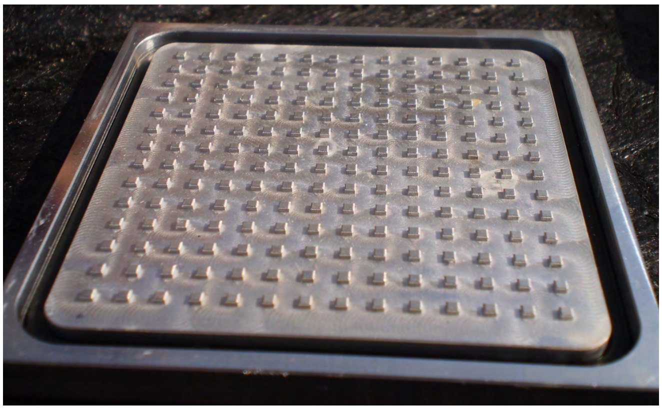

Figure A.2: *Zoom on base plate with 0.5 mm high fins.*

In figure A.3 the hybrid design is shown. On the left side the perforated inlet plate with six inlets is shown, and on the right hand side the cold plate with mini channels is seen. In these manufactured designs the O-rings used for making a tight seal are also shown.

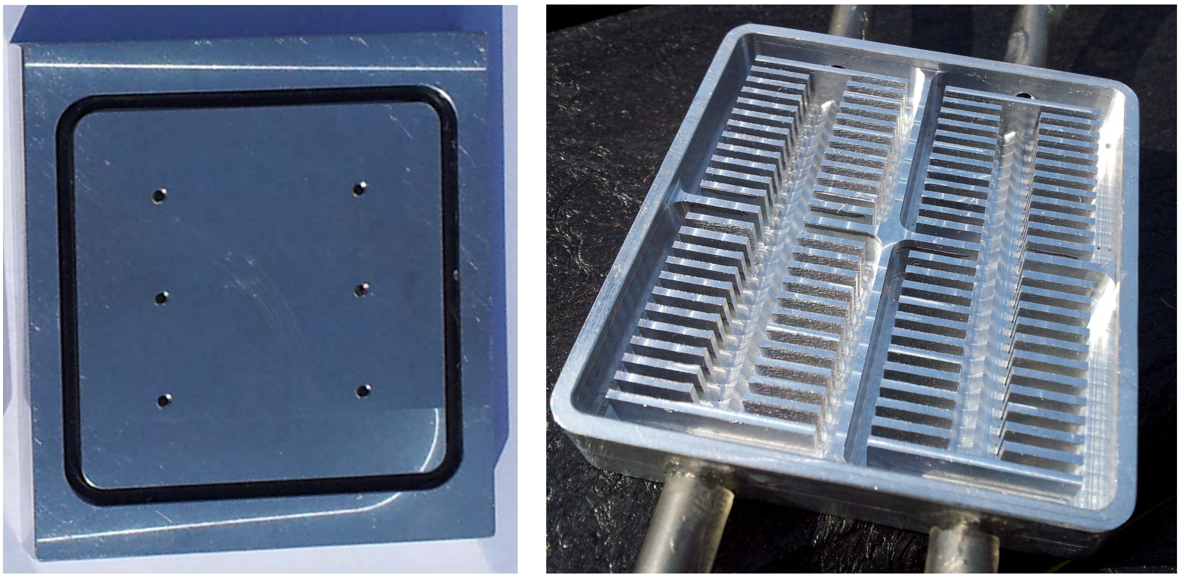

(a) (b)

Figure A.3: *Hybrid design manufactured.*

Thermal Resistance Analysis

B

In order to find the temperature difference from the IGBTs and the cold plate, 1D thermal resistance analysis is applied in this appendix. It is not needed to apply more dimensions to the analysis due to very thin material layers. Thus the thermal resistance is higher in the directions parallel to the IGBTs than the normal direction to the IGBTs. In figure B.1 a schematic of the material layers of the IGBT is shown with its dimensions.

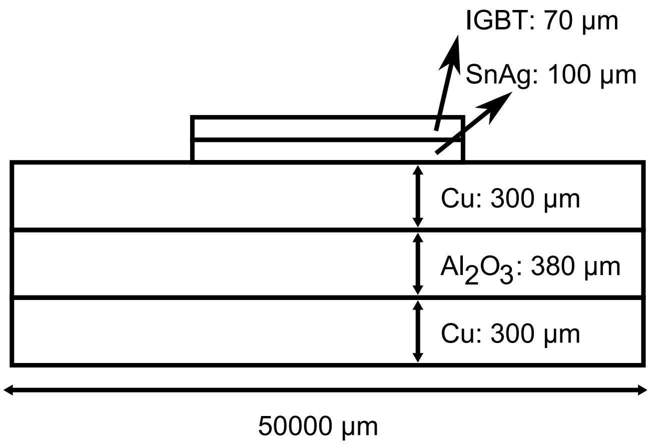

Figure B.1: *Schematic of material layers in IGBT power module [Olesen, 2012].*

The thermal resistance is generally calculated by [Cengel, 2006]:

$$R = \frac{L}{k \cdot A} \qquad \left[\frac{K}{W}\right] \tag{B.1}$$

where L is the thickness of the layer, k is the thermal conductivity and A is the area of the layer. The temperature difference across the layer is calculated by [Cengel, 2006]:

$$\Delta T = P \cdot R \qquad [K] \tag{B.2}$$

where P is the thermal power transfered. Figure B.2 shows a representation of the thermal resistance network for figure B.1.

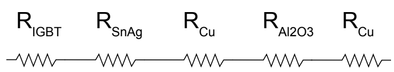

Figure B.2: *Representation of the thermal resistance network of the IGBT power module.*

The resistance is calculated by using the following parameters [Olesen, 2012]:

- IGBT: $L = 70\ \mu m$ and $A = 9 \cdot 10^{-5}\ m^2$
- SnAg: $L = 100\ \mu m$ and $A = 9 \cdot 10^{-5}\ m^2$

- Cu: Two times $L = 300\ \mu m$ and $A = 25 \cdot 10^{-4}\ m^2$
- Al_2O_3: $L = 380\ \mu m$ and $A = 25 \cdot 10^{-5}\ m^2$

The thermal conductivity of each material at room temperature is found from EES, [Accuratus, 2002], and [Wilson, 2006]:

- IGBT: $k = 149\ ^{W}/_{m\,K}$
- SnAg: $k = 78\ ^{W}/_{m\,K}$
- Cu: $k = 400\ ^{W}/_{m\,K}$
- Al_2O_3: $k = 35\ ^{W}/_{m\,K}$

The different resistances are in series, hence the total resistance is:

$$R_{total} = R_{IGBT} + R_{SnAg} + R_{Cu} + R_{Al_2O_3} + R_{Cu} \qquad \left[\frac{K}{W}\right] \tag{B.3}$$

The total resistance is calculated to be:

$$R_{total} = 0.0164 \qquad [^{K}/_{W}] \tag{B.4}$$

The diode is assumed to have the same thermal resistance as the IGBT, but with half of the active area. For a heat dissipation of 900 W, the temperature difference from the junction and to the cold plate is 14.7 K with the above resistance analysis. However, to this value the effect of having a thermal interface material (TIM) needs to be included if this is applied to the cold plate. The common used TIM is Dow Corning 340 with a thermal conductivity of 0.54 $^{W}/_{m\,K}$. The thickness of the TIM is assumed to be 50 μm [Olesen, 2012], but this value is quite uncertain. TIM should ideally only be applied in areas of air gaps between the two materials where heat transfer occurs, as the areas which is in direct contact have a better heat transfer.

If it is assumed that the area of the TIM is the same area of the copper plate, and that it has an uniform thickness of 50 μm, the temperature difference between the junction and the cold plate will then be approximately 48 K. Hence, it should be stressed that the TIM should be applied in the small air gasps.

Due to the large uncertainty in estimating the thermal contact resistance, the thermal resistance analysis and the CFD analysis are not coupled.

CFD Theory

C

In this chapter various key aspects of computational fluid dynamics (CFD) are presented. CFD is a numerical analysis tool for systems where fluid flow, heat transfer, and chemical reactions are involved.

C.1 Introduction to CFD

In general a CFD analysis consists of three main elements: pre-processing, solver, and post-processing [Versteeg and Malalasekera, 2007]. An overview of this is shown in figure C.1.

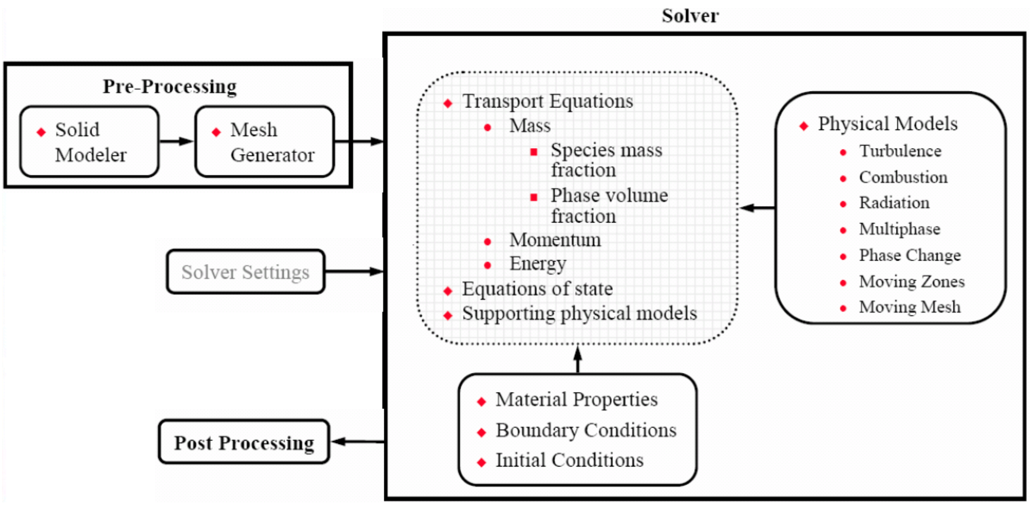

Figure C.1: *Overview of CFD Modeling [Yin, 2010].*

In the pre-processing step the geometry is defined, and the grid is generated. The grid consists of small non-overlapping sub-domains. After this the fluid properties is defined, and the appropriate boundary conditions has to be set up. In the solver step the finite volume method is applied, which in outline consists of [Versteeg and Malalasekera, 2007]:

- Definition of all governing differential equations over all the control volumes.
- Integration of the differential equations.
- Conversion of the integral equations into algebraic equations by discretization.
- Solution of algebraic equations by an iterative method.

When convergence is obtained by having negligible sized residuals and correct energy and mass balance, an important step is to investigate whether the solution is grid independent, or if the mesh should be refined

[ERCOFTAC, 2000]. In the post-processing step the results are examined. This can be shown in a variety of ways by e.g. contour or vector plots of the temperature and pressure distribution.

C.2 Governing Equations used for CFD

In each cell the governing equations for fluid flow and heat transfer is solved. Each of these equations are presented in this section. The mass of a fluid is conserved, and in figure C.2 the mass flow in and out of each side of the differential volume is shown. These mass flows pr. area are approximated by a Taylor expansion.

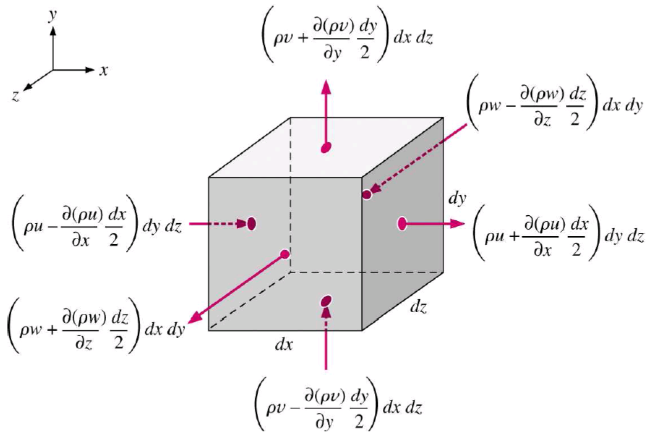

Figure C.2: *Mass flows in differential control volume [Cengel and Cimbala, 2006].*

From this the continuity equation is shown to be [Versteeg and Malalasekera, 2007]:

$$\frac{\partial \rho}{\partial t} + \frac{\partial(\rho u)}{\partial x} + \frac{\partial(\rho v)}{\partial y} + \frac{\partial(\rho w)}{\partial z} = 0 \tag{C.1}$$

Newton's second law states that the rate of change in momentum on a fluid is equal to the sum of the forces acting on it. The different forces acting on a fluid particle is defined as [Versteeg and Malalasekera, 2007]:

- **Surface forces**
  - Pressure forces
  - Viscous forces
  - Gravity forces
- **Body forces**
  - Centrifugal forces
  - Coriolis forces
  - Electromagnetic forces

When writing momentum equations the body forces are often written as a source term. In a Newtonian fluid the viscous stresses are proportional to the rate of deformation. The following Navier-Stokes equations describes the change in momentum in a fluid, and is hence used to find the velocity components u, v, and w [Versteeg and Malalasekera, 2007]:

$$\frac{\partial(\rho u)}{\partial t} + \nabla(\rho u \mathbf{u}) = \nabla(\mu \, grad \, u) + S_{Mx} - \frac{\partial p}{\partial x} \tag{C.2}$$

$$\frac{\partial(\rho v)}{\partial t} + \nabla(\rho v \mathbf{u}) = \nabla(\mu \, grad \, v) + S_{My} - \frac{\partial p}{\partial y} \tag{C.3}$$

$$\frac{\partial(\rho w)}{\partial t} + \nabla(\rho w \mathbf{u}) = \nabla(\mu \, grad \, w) + S_{Mz} - \frac{\partial p}{\partial z} \tag{C.4}$$

The first law of thermodynamics states that the change in energy is the same as the sum of rate of work done on, and the rate of heat addition to, a fluid particle. The energy equation is derived from this principle, and is given as [Versteeg and Malalasekera, 2007]:

$$\underbrace{\frac{\partial(\rho i)}{\partial t}}_{Transient} + \underbrace{\nabla(\rho i \mathbf{u})}_{Convective} = \underbrace{\nabla(k \, grad \, T)}_{Diffusion} + \underbrace{\Phi}_{Dissipation} \underbrace{- p \, \nabla \, \mathbf{u} + S_i}_{Source} \tag{C.5}$$

The type of each term is shown in equation (C.5). The dissipation term represents the internal energy created due to the deformation work done on the particle.

In the five above partial differential equations (continuity, 3 times momentum, and energy) the four thermodynamic variables ρ, p, i, and T are among the unknowns. To solve the system of equations it has to be mathematical closed. To ensure this the equations of state is used, which are stated as:

$$p = \rho \cdot R \cdot T \tag{C.6}$$

$$i = C_v \cdot T \tag{C.7}$$

When the flow is compressible and the pressure-velocity coupling is used the continuity equation is used to calculate the density, and the energy equation calculates the temperature. The pressure is then obtained from equation (C.6). When the flow is incompressible the continuity equation is used as a constraint. The default solver in ANSYS FLUENT is the iterative Semi-Implicit Method for Pressure-Linked Equations (SIMPLE) algorithm. In this algorithm the pressure field is guessed and used to solve the momentum equations, and also to solve a pressure correction equation, which is made from the continuity equation. When the pressure correction equation is solved, the pressure is used to update the velocity and pressure field. To start the algorithm initial guesses must be made. The process is iterated until the velocity and the pressure fields have converged [Versteeg and Malalasekera, 2007].

C.3 The Finite Volume Method

With a variable ϕ, the governing equations can be written in general as [Versteeg and Malalasekera, 2007]:

$$\underbrace{\frac{\partial(\rho \phi)}{\partial t}}_{Transient} + \underbrace{\nabla(\rho \phi \mathbf{u})}_{Convective} = \underbrace{\nabla(\Gamma \, grad \, \phi)}_{Diffusion} + \underbrace{S_\phi}_{Source} \tag{C.8}$$

The first step in the finite volume method (FVM) is the integration over the control volume, which for equation (C.8) gives:

$$\int_{CV} \frac{\partial(\rho\phi)}{\partial t} \mathrm{d}V + \int_{CV} \nabla(\rho\phi\mathbf{u})\mathrm{d}V = \int_{CV} \nabla(\Gamma\, grad\ \phi)\mathrm{d}V + \int_{CV} S_\phi \mathrm{d}V \tag{C.9}$$

The next step is to apply Gauss' divergence theorem, which in general states the following for a vector $\vec{a}$ [Versteeg and Malalasekera, 2007]:

$$\int_{CV} \nabla(\vec{a})dV = \int_A \vec{n}\cdot\mathbf{a}\ \mathrm{d}A \tag{C.10}$$

This can be applied to equation (C.9) which in its steady state form then is:

$$\int_A \vec{n}\cdot(\rho\phi\vec{u})\mathrm{d}A = \int_A \vec{n}\cdot(\Gamma\, grad\ \phi)\mathrm{d}A + \int_{CV} S_\phi \mathrm{d}V \tag{C.11}$$

The product of $\vec{n}\cdot(\rho\phi\vec{u})$ is the flux component of ϕ due to the fluid flow along the normal vector $\vec{n}$ to the surface element dA. The next step in the FVM is to discretize the integral equation. An example of a steady 1-D convection-diffusion problem is given to illustrate this. This example is based on Pantankar [1980] and Versteeg and Malalasekera [2007].

When sources are omitted the differential equation for such a problem is:

$$\frac{d}{dx}(\rho u\phi) = \frac{d}{dx}\left(\Gamma\frac{d\phi}{dx}\right) \tag{C.12}$$

The grid points are shown in figure C.3. The attention is focused on the grid point P with its two neighboring points E and W.

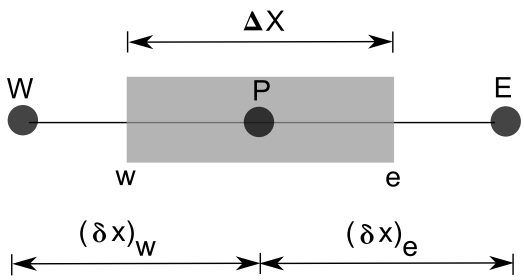

Figure C.3: *A control volume around the node P [Pantankar, 1980].*

In equation (C.12) ϕ is a property in the flow field u, which is the velocity in the x-direction. When equation (C.12) is integrated over its control volume the following equation applies:

$$(\rho uA\phi)_e - (\rho uA\phi)_w = \left(\Gamma A\frac{\mathrm{d}\phi}{\mathrm{d}x}\right)_e - \left(\Gamma A\frac{\mathrm{d}\phi}{\mathrm{d}x}\right)_w \tag{C.13}$$

To obtain the discretized equations the terms must be approximated. Two new variables are introduced to help with this:

$$F = \rho u \qquad \text{and} \qquad D = \frac{\Gamma}{\delta x} \tag{C.14}$$

The cell face values for these variables are:

$$F_w = (\rho u)_w \qquad \text{and} \qquad F_e = (\rho u)_e \tag{C.15}$$

$$D_w = \frac{\Gamma_w}{\delta x_w} \qquad \text{and} \qquad D_e = \frac{\Gamma_e}{\delta x_e} \tag{C.16}$$

An assumption is that $A_e = A_w = A$. Equation (C.13) can now be written as:

$$F_e \left(\frac{\phi_P + \phi_E}{2} \right) - F_w \left(\frac{\phi_W + \phi_P}{2} \right) = D_e(\phi_E - \phi_P) - D_W(\phi_P - \phi_W) \tag{C.17}$$

In the above example central difference is used (2nd order discretization) for the estimation of the property ϕ on the west and east side of the node P. If the 1st order upwind scheme is used in ANSYS FLUENT, only the upstream side is used. With higher discretization schemes the accuracy improves, but it may be more difficult to obtain convergence [Yin, 2010].

C.4 Mesh Design

If nothing else is mentioned, this section about mesh design is based on ERCOFTAC [2000]. When creating the mesh over the geometry of interest an adequate resolution is needed. It is however sometimes a compromise as the computational time increases with an increased number of cells. Besides the grid density, the quality of the mesh also depends on different criteria such as the aspect ratio, skewness, warped cells and included angle of adjacent cells. O-grids and C-grids can help to improve quality for a block-structured mesh. For unstructured mesh it is an advantage to have prism layers, which is structured sub-mesh, close to the domain boundary. In figure C.4 (b) different cell types used in mesh generation is shown.

The skewness, S, is a number between 0 and 1, and is calculated by the following equation [Cengel and Cimbala, 2006]:

$$S = MAX \left[\frac{\theta_{max} - \theta_e}{180 - \theta_e}, \frac{\theta_e - \theta_{min}}{\theta_e} \right] \qquad [-] \tag{C.18}$$

θ_{max} is the maximum angle in the cell, θ_{min} is the minimum angle in the cell, and θ_e is the angle for the equiangular cell, and this applies to both a square and a triangular cell. These angles are shown in figure C.4 (a). When S is equal to 1, the skewness is at its highest, while for a orthogonal cell the skewness is 0, which gives the highest quality.

According to ERCOFTAC [2000] the following guidelines should be kept in mind when creating the mesh:

- The mesh domain must incorporate all relevant features of the flow and the geometry.
- Omit geometrical features if it e.g. have dimensions smaller than the local grid size.
- Use grid refinement in areas where local detail is wanted.
- Highly skewed cells should be avoided, see equation (C.18). Preferably, the angles should be 90°, and not less than 40° or more than 140° for hexahedral cells. If the mesh has tetrahedral mesh, the 4 angles should preferably be the same size.

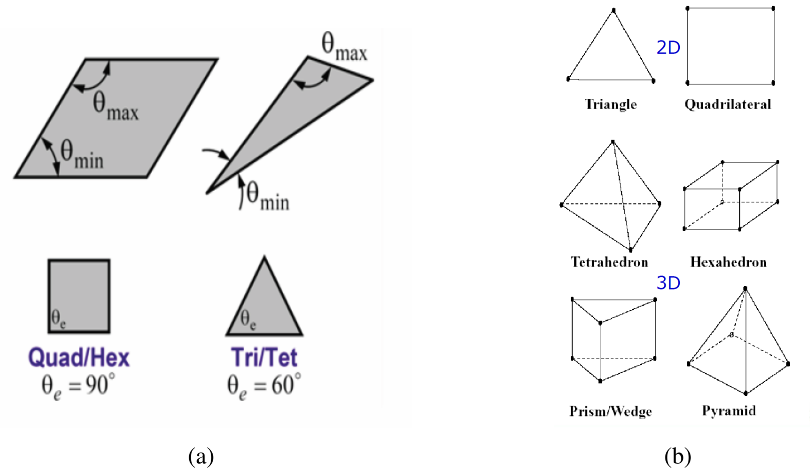

Figure C.4: *(a) showing different cell types and figure (b) angles used for evaluating skewness of a cell [Yin, 2010].*

- It is a strong requirement that the cells near the boundary should be orthogonal. In addition to this, tetrahedral elements should also be avoided in the boundary layer, due to the dependency of hexahedral cells for the wall functions.
- High aspect ratios in the order of 20 to 100 should be avoided in the important regions of the flow field. However, near the walls it can be beneficial to have a high aspect ration in the boundary layer.
- If the code being used can make grid adaption, the user should be aware, that the grid quality with regards to the skewness and aspect ration might not be improved when using the grid adaption.
- Non-matching cell faces and arbitrary mesh coupling should be avoided, especially in regions with high flow gradients.
- A grid independency study need to be made. At least three different sized meshes should be used to check if mesh independence has been obtained.

C.5 Turbulence

When a flow is turbulent, the velocity field will fluctuate, and eddies of different length and time scale will appear in the flow. In general there are three methods for modeling the turbulence with CFD [Versteeg and Malalasekera, 2007]:

- Reynolds-averaged Navier-Stokes equations (RANS)
- Large eddy simulation (LES)
- Direct numerical simulation (DNS)

The RANS equations are focused on the mean flow properties and its turbulent fluctuations. The Navier-Stokes equations are time-averaged, and by doing this, extra terms occur for the turbulence. These extra terms are modeled by different turbulence models such as e.g. $k-\varepsilon$ or $k-\omega$ models. LES tracks the behavior of larger eddies, while it rejects the smaller eddies, which however are included as a sub-grid scale model. DNS computes the mean flow with all the turbulent velocity fluctuations, as it resolves the Kolmogorov length scale with time step sufficiently small to resolve the fastest fluctuations. This method is very costly in terms of computer power, and is therefore seldom used.

In the $k-\varepsilon$ model k is the turbulent kinetic energy, and ε is the rate at which turbulent energy dissipates into smaller eddies. When using this turbulence model, an important thing to consider is the mesh design, which has to fit to the used wall function. A dimensionless number y^+ can be used to estimate if the resolution of the near wall mesh is fine enough [ANSYS, Inc, 2009]:

$$y^+ = \frac{y u_\tau}{\nu} \qquad [-] \tag{C.19}$$

y is the distance to the nearest wall $[m]$, ν is the kinematic viscosity of the fluid $[{}^{m^2}/_{s}]$, and u_τ is the friction velocity given by:

$$u_\tau = \sqrt{\frac{\tau_w}{\rho}} \qquad \left[\frac{m}{s}\right] \tag{C.20}$$

τ_w is the wall shear stress $[Pa]$. In figure C.5 the suitable y^+ for the different wall functions is shown. It is also shown in which part of the boundary layer the different wall functions operate.

Enhanced Wall Treatment (EWT)	$y_p^+ \approx 1$, Can go upto $y_p^+ \leq 5$ First cell in Laminar Sublayer	Low Re flows, better drag, pressure - drop prediction
Standard Wall Functions (SWF)	$y_p^+ \geq 30-300$ First cell in Log Layer	High Re flows, little gain by resolving sublayer
Non-Equilibrium Wall Functions	Limits same as SWF, Accounts for ∇p effects	For mildly separating, reattaching flows,

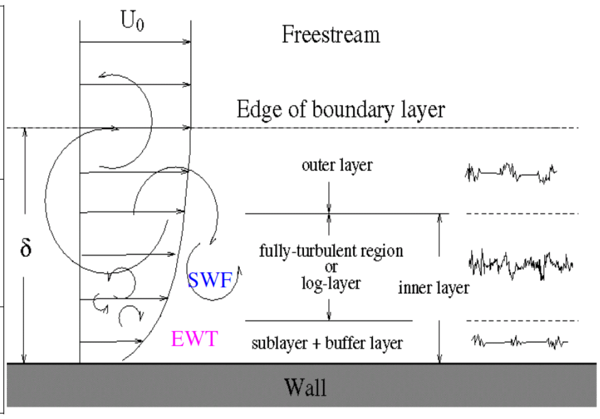

***Figure C.5:** Mesh requirements for wall functions [Chilka and Kulkarni, 2010].*

When using the enhanced wall treatment y^+ should preferably be around 1, but can go up to 5. The important thing is that the first cell is in the laminar sublayer. For the standard wall function y^+ should be between 30 and 300 where the first cell is in the log layer. This is also the same for the non-equilibrium wall function. From this it is concluded that care should be taken to ensure that y^+ is not between 5 and 30 when using a wall function.

Another turbulence model that can be used is the $k-\omega$ model, where ω is the frequency of large eddies, and defined as $\omega = {}^{\varepsilon}/_{k}$ [Versteeg and Malalasekera, 2007]. The $k-\omega$ model performs well close to wall boundaries, but it can be sensible to free stream analysis. A special case of the model is the $k-\omega$ shear stress transport (SST) version. Here the properties close to the wall is from the $k-\omega$ model, while it gradually blends into the $k-\varepsilon$ model away from the wall, and as a result the accuracy is increased [ERCOFTAC, 2000]. This blending is shown in figure C.6, where the result of the blending is seen in the right side of the figure.

It is important to set the turbulent boundary conditions, where a general guideline for the turbulent intensity is given by the following equation [Chilka and Kulkarni, 2010]:

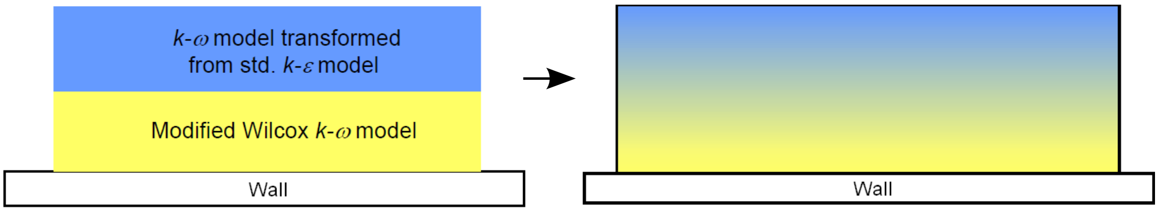

Figure C.6: *Wall modeling for the $k-\omega$ SST turbulence model [Fluent Inc., 2005].*

$$I = 0.16 \cdot Re^{-1/8} \qquad [-] \tag{C.21}$$

An important part when making CFD simulation is to be able to validate the model. This can be done by an experiment with e.g. particle image velocimetry or planar laser induced fluorescence. The following quote must be kept in mind [Versteeg and Malalasekera, 2007]: "Anyone wishing to use CFD in a serious way must realize that it is no substitute for experimentation, but a very powerful additional problem solving tool."

C.6 Study of Hexahedral and Tetrahedral Mesh

An investigation of the output of a CFD analysis dependent on a hexahedral mesh versus a tetrahedral mesh is made to see the difference between these types of mesh. A hybrid mesh with both hexahedral cells and tetrahedral cells is also made. ERCOFTAC [2000] states that a tetrahedral mesh should preferable not be used at walls, because of the weakness when using wall functions, thus a hexahedral wall meshes should be used. In table C.1 the maximum temperature in a simulation similar to the CFD analysis in section 3.4.2 is shown together with the type of mesh and spatial discretization scheme used. The CFD analysis and the geometry in question is further described in section 3.4.2. The input to the CFD analysis is:

- $\dot{q} = 240,000\ ^{W}/_{m^2}$
- $T_i = 303.15\ K$
- $\dot{m} = 0.000141\ ^{kg}/_{s}$

As seen in table C.1 all cases of tetrahedral mesh in general under predicts the maximum temperature compared to the case of hexahedral and hybrid mesh. Between the case of hexahedral and hybrid mesh the temperatures is rather similar with a second and third order discretization scheme.

In figure C.7 a contour plot of the temperature through a plane in z = 3 *mm* is shown for each of the three types of mesh.

It is seen that the best resolution of the temperature contour is obtained from the hexahedral mesh, while it gets more coarse for the two other types of mesh.

From this mesh study the most important conclusion is that a hybrid solution, with hexahedral mesh close to the wall and tetrahedral above it, can give reasonable accurate results. The criteria for using a hybrid solution is to have a grid independent mesh where higher discretization schemes is used. It is an advantage to allow hybrid mesh as the time spend on generating the mesh can be shorter than if a pure hexahedral mesh is to be made.

The hybrid prism layer mesh with both hexahedral and tetrahedral mesh is seen in figure C.8.

Scheme and size	First order	Second order	Third order
Tetrahedral, 25,512 cells	316.40 K	319.79 K	319.55 K
Tetrahedral, 55,040 cells	316.72 K	320.39 K	320.02 K
Tetrahedral, 121,861 cells	316.49 K	320.50 K	320.12 K
Hexahedral, 35,360 cells	320.77 K	321.27 K	321.33 K
Hexahedral, 97,500 cells	321.15 K	321.48 K	321.58 K
Hexahedral, 206,400 cells	321.07 K	321.37 K	321.42 K
Hybrid, 19,545 cells	319.5 K	321.13 K	321.17 K
Hybrid, 24,974 cells	319.89 K	321.18 K	321.18 K
Hybrid, 70,723 cells	319.47 K	320.86 K	320.84 K

Table C.1: *Maximum temperature for various mesh and schemes.*

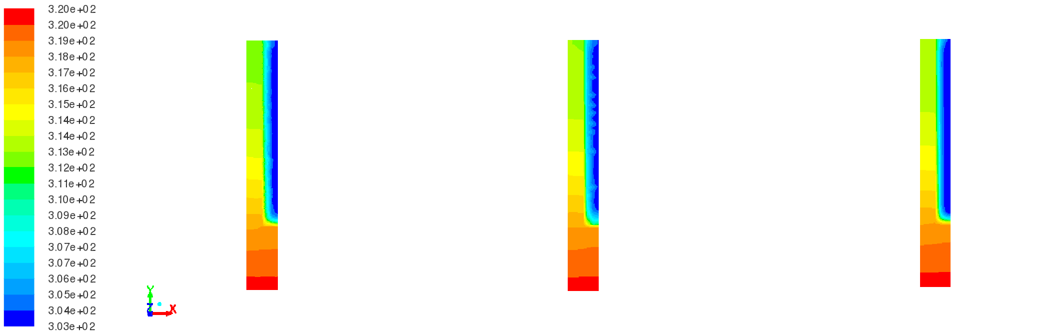

(a) *Tetrahedral mesh.* (b) *Combination of hexahedral and tetrahedral mesh.* (c) *Hexahedral mesh.*

Figure C.7: *Temperature contour plot 3 mm downstream of channel.*

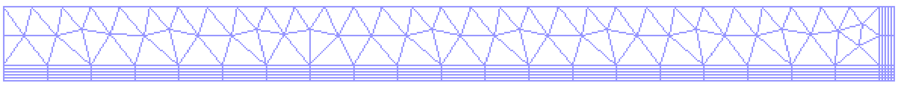

Figure C.8: *Hybrid mesh seen from the side.*

It is further be concluded that if a pure tetrahedral mesh is to be used, mesh independency has to be ensured, and in addition to that, a higher order discretization is absolutely necessary if such a mesh is to be used.

Discussion of Length of Jet Tubes

D

This chapter discusses the length of jet tubes, and it is concluded, that short jet tubes does not influence the result significantly. It is hereby possible to minimize the amount of material upon commercialization of the cold plates.

In this appendix the effect of varying the length of the jet tubes is investigated. Having a long straight tube will ensure fully developed flow, but will also introduce a larger pressure drop. Two dimensional CFD simulations of the situation is made with three different lengths of the inlet tube. The domain with its dimensions used for simulation is shown in figure 5.14 on page 35. The inlet is at the top in this figure, and hence the direction for the incoming flow is in the negative y-direction. Two outlets are located in the bottom of each side. The simulations are carried out with a mesh independent quadrilateral mesh.

The three different lengths of inlet tube is 0.1 mm, 0.5 mm, and 15 mm, respectively. The diameter for each of these tubes is 1 mm. When the length of the inlet tube is 0.1 mm and 0.5 mm an additional width of 5 mm is added to the domain over the narrow passage. The velocity in the inlet is 1.4 $^{m}/_{s}$. For the two cases with a length of the tube of 0.1 mm and 0.5 mm, the velocity at the inlet is scaled to give the same mass flow as in the case with a tube of 15 mm. In figure D.1 the velocity magnitude is seen in a contour plot for a length of the inlet tube of 15 mm and 0.5 mm. The velocity magnitudes are seen to be rather similar inside the chamber.

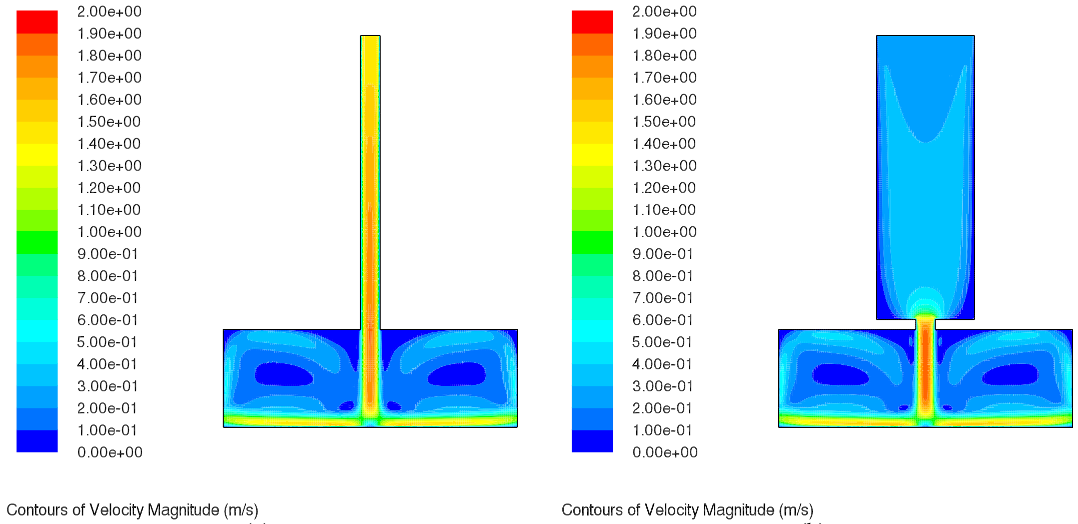

(a) (b)

Figure D.1: *Figure (a) showing the velocity magnitude with a inlet length of 15 mm for the pipe, and figure (b) showing the velocity magnitude for a pipe with a length of 0.5 mm.*

It is interesting to see the change in width of the jet, when the length of the pipe becomes very short. A closer look at the velocity magnitude at a cross section along the x-direction at constant value of $y = 1\ mm$ shows the difference for the three cases, and this is shown in figure D.2 (b). Also the velocity magnitude at a cross section along the y-direction with a constant value of $x = 7.5\ mm$ is shown in figure D.2 (a).

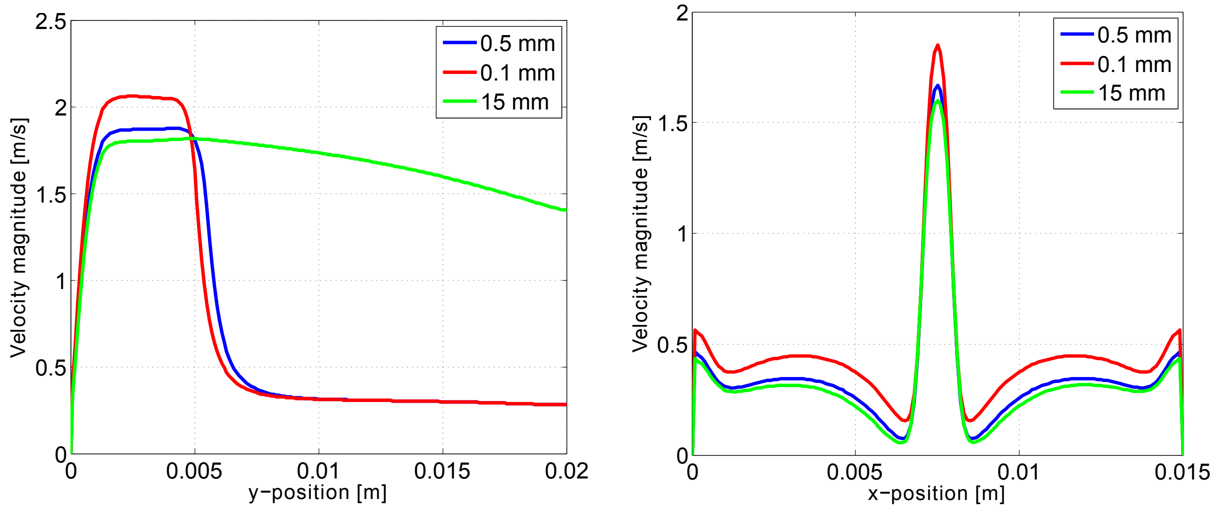

(a) (b)

Figure D.2: *Figure (a) showing the velocity magnitude at constant value of x = 7.5 mm for the three cases, and figure (b) showing the velocity magnitude at a constant value of y = 1 mm for the three cases.*

From figure D.2 it is seen that the velocities are higher with shorter lengths of the inlet tube. This applies both in the middle of the jet, but also on each side of the jet. When looking at the velocity magnitude in figure D.2 (a), it is seen that velocity magnitude rises fast before the inlet starts at $y = 5\ mm$ for the two short inlet tubes, while the velocity magnitude rises steady through all of the long inlet tube, as the flow is developing.

Since the velocities are higher when the length of the throat is shortest for both the cases in figure D.2, and the pressure drop in general is smaller a short tube compared to a long tube, it is concluded that a short tube is preferable in the designs. The length of the tubes is however limited to a minimum length due to the fact that there has to be enough space on each side of the perforated plate to fit O-rings.

Manifold for Mini Channels

E

This chapter discusses the problem with the manifold design for mini channels and staggered fins.

Idelchik [1996] provides tools to determine if the manifold design should be U- or Z-type. For this analysis the variable K_{coll} is used:

$$K_{coll} = \frac{\Delta p_{coll}}{\rho \cdot v_i^2/2} = f \cdot \frac{L}{D} \tag{E.1}$$

If the resistance coefficient, K_{coll} is less than 1, and the resistance of the outlet and inlet collector are equal, then the U-shaped design will provide a more uniform flow distribution than the Z-shaped design. If K_{coll} is greater than 1, the Z-shaped will give the most uniform distribution. K_{coll} is found to be 0.25. This means that a U-shaped design should give the best flow distribution. Hence, if the designs should be redesigned, a U-shaped manifold is recommended.

If a Z-shaped manifold is used Idelchik [1996] recommends, that it should be considered to have an outlet manifold of variable cross sectional area if the parameter A_4 is above 0.3. A_4 is a characteristic number for Z-shaped manifold design, and is given by:

$$A_4 = \frac{\bar{f}}{\sqrt{0.6 + (f_s/f_s^*)^2 + K_{sec} + K_{app}}} \tag{E.2}$$

This is found to be 3.6, so a variable cross sectional manifold area will give the best pressure distribution. The empirical constant $\bar{f}$ is defined as $n \cdot f_s/F_i$, which is the number of branches times the inlet area of the branch divided by the area of the manifold. f_s^* is the outlet area of the branch, K_{sec} is the loss coefficient of the branch section, and K_{app} is the loss coefficient of a possible application in the branch. Since there is no applications in the mini channel design, this is set to zero. Solovitz and Mainka [2011] states that a Z-shaped manifold with variable inlet and outlet cross section is advantageous, shown in figure E.1.

By the above considerations a U-shaped manifold should be made. Idelchik [1996] states that in some cases a more uniform distribution of flow in a U-shaped header may be achieved, by contracting the cross section of the inlet header in the direction towards its inlet, while keeping the cross section of the outlet constant.

This discussion shows, that further investigation of the manifold design is necessary in order to provide a uniform flow distribution to the channels. This could be investigated by applying CFD simulations to these design ideas. As a concluding remark, the manifold used in the present designs could have been larger in order to decelerate the inlet jet.

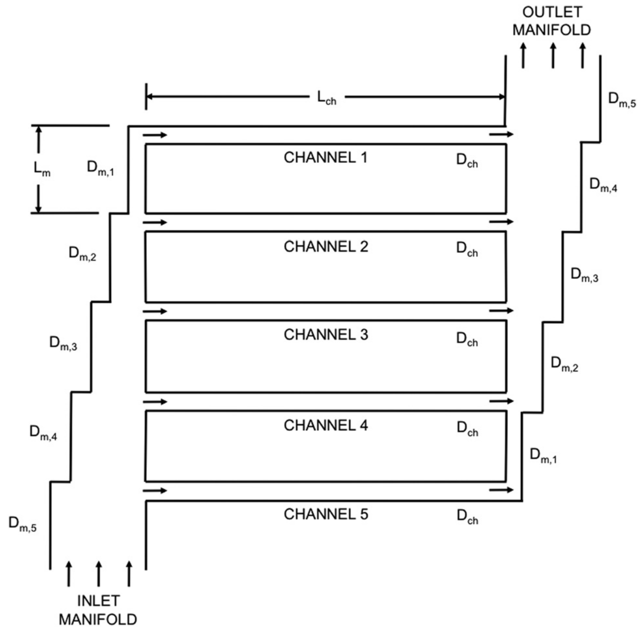

Figure E.1: *Variable cross section for the inlet and outlet for a Z-shaped manifold [Solovitz and Mainka, 2011].*

Investigation of Heat Transfer in Mini Channels using Planar Laser Induced Fluorescence

II

Investigation of Heat Transfer in Mini Channels using Planar Laser Induced Fluorescence

M R Bøgild, J L Poulsen, E Z Rath, and H Sørensen

Department of Energy, Aalborg University, Pontoppidanstræde 101, 9000 Aalborg, Denmark

E-mail: `jonas.lundsted@gmail.com`

Abstract. In this paper an experimental investigation of the heat transfer in mini channels with a hydraulic diameter of 889 μm is conducted. The method used is planar laser induced fluorescence (PLIF), which uses the principle of laser excitation of rhodamine B in water. The goal of this study is to validate the applicability of PLIF to determine the convective heat transfer coefficient in mini channels against conventional correlations of the convective heat transfer coefficient. The applicability of the conventional theory in micro and mini channels has been discussed by several researchers, but to the authors knowledge the applicability of PLIF to validate this has not yet been investigated thoroughly. The experiment shows good agreement to the conventional correlation, and the resolution of the temperature gradient at the wall is found sufficiently accurate in certain areas. However, PLIF is not found satisfactory over the whole domain, and the limitations and errors are analysed.

1. Introduction

Investigation of the micro scale heat transfer is a relevant topic due to the question of the applicability of conventional heat transfer correlations. The published results of the various studies diverse from one another. The convective heat transfer coefficient has either fallen below [1] or above [2, 3] the value expected for conventional length scale channels. Others have reported little, or no diversity from conventional length scales [4]. In the present study the goal is to use the non-intrusive method of planer laser induced fluorescence (PLIF) for determination of local temperatures in mini channels with a hydraulic diameter of 889 μm. With this method it should be possible to find the temperature gradient at the wall, which can be used to find the convective heat transfer coefficient [5]:

$$h = \frac{-k_{fluid}\,(\partial T/\partial y)_{y=0}}{T_{wall} - T_\infty} \qquad \left[\frac{W}{m^2K}\right] \tag{1}$$

h is the convective heat transfer coefficient, k_{fluid} is the conductive heat transfer coefficient of the fluid, $(\partial T/\partial y)_{y=0}$ is the temperature gradient at the wall, T_{wall} is the temperature at the wall and T_∞ is the temperature of the water sufficiently far from the wall. The above equation is valid because the fluid adjacent to the wall is motionless as a consequence of the no-slip condition, and hence the conductive heat transfer per area is equal to the convective heat transfer per area. By using PLIF to find the temperature gradient it may be possible to validate the above statements. The goal of the present paper is to investigate the applicability of PLIF to determine the convective heat transfer coefficient.

Figure 1 (a) shows the dimensions of the mini channels used for the experiment. The length of the module is the same as the width. For this specific case the cross sectional aspect ratio of the channels is 8, and the length of each of the 19 channels is 20 mm. The hydraulic diameter is 889 μm. Figure 1 (b) shows the experimental setup with laser, camera, and flow box containing the mini channels.

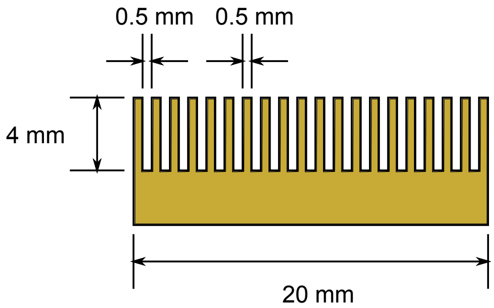

(a)


(b)

Figure 1. *Figure (a) showing channel dimensions, and figure (b) showing experimental setup.*

In the present paper an experiment is conducted with a flow of 0.5 l/min, corresponding to a Reynolds number of 260, and the heat input power is 100 W.

2. Conventional Nusselt Number Approximation

The conventional heat transfer theory does in many cases not apply to a specific problem, often because the specific problem is too complex. Thus, the problem needs to be simplified, or to be divided into parts where different theory applies. The theory of flow in mini channels corresponds to the theory of either forced convection in ducts, or forced convection between two parallel plates due to a high aspect ratio. The Nusselt number depends on these assumptions. The flow in mini channels is in this case kept in the laminar regime, which develops through the channel. Several different cases of flow are described by the conventional theory, where both the hydrodynamical and thermal boundary layer can be assumed to be either fully developed or developing. These assumptions can then be combined in a variety of ways.

The Nusselt number theory is often divided into two cases; the walls have constant temperature or the heat flux is constant through the channel. None of the two cases apply perfectly, but the case of constant heat flux is the best compromise between the two cases.

Since the hydrodynamical boundary layer is developing until $L_H = 0.05ReD_h$ for laminar flow, a Reynolds number of more than 450 leads to a developing flow throughout the full channel length. The correlation of Stephan and Preusser [6] describes simultaneously developing flow with constant wall heat flux in circular geometry, and do not account for aspect ratio effects. However, the correlation is implemented using the hydraulic diameter for a rectangular channel:

$$Nu = 4.364 + \frac{0.086 \cdot \left(Re \cdot Pr \cdot \frac{D_h}{L}\right)^{1.33}}{1 + 0.1 \cdot Pr \cdot \left(Re \cdot \frac{D_h}{L}\right)^{0.83}} \qquad [-] \qquad (2)$$

This correlation is valid in the range of $0.7 < Pr < 7$ or $RePrD_h/L < 33$ for $Pr > 7$. Keeping the temperature above 20 $°C$, the Prandtl number is below 7. When dealing with Reynolds number under 450, the end of the channel has a hydrodynamically developed boundary layer, where a correlation by Shah and London [7] for parallel plate ducts is applicable.

Knowing the Nusselt number, the convective heat transfer coefficient is calculated by [5]:

$$h = \frac{Nu \cdot k_{fluid}}{D_h} \qquad \left[\frac{W}{m^2 K}\right] \tag{3}$$

3. Experiment

The fundamental principle of PLIF is to have a fluorescent dye in a fluid which get excited by light from a laser at a proper wavelength, and then re-emits the light at a longer wavelength during spontaneous transition from the excited state down to the ground state [8, 9]. The wavelength is longer because of energy losses in the excited state. Because of thermal quenching the luminescent intensity is reduced with increasing temperature [10]. In this experiment rhodamine B is used as the fluorescent dye as a continuous Argon-Ion laser with a 20° lens illuminates the flow with green light with a wavelength of 532 nm, where the absorption intensity in rhodamine B is high. This can be seen in figure 2 (a).

The fluorescence intensity for rhodamine B vary with about 2 $\%/K$ [11], which makes it suitable for temperature measurements. For rhodamine B the energy is re-emitted close the wavelength of orange light in the vicinity of 590 nm. The fluorescence is captured by a 1024x768 pixel charged coupled device (CCD) SVS-VISTEK 204F camera with a 590 nm filter and 60 mm Nikon lens. The fluorescence intensity, I, can be described by the following equation [9]:

$$I = I_0 \; A \; \phi \; \epsilon \; C \; \frac{\lambda_e}{\lambda_f} \qquad [-] \tag{4}$$

I_0 is the excitation intensity, A is the fraction of collected light, ϕ is the quantum yield, ϵ is the molar absorptivity, and C is the concentration of rhodamine B. λ_e and λ_f is the wave length of the excitation light and the fluorescence light, respectively.

A schematic drawing of the experimental setup is shown in figure 2 (b). The power input is applied from an electric heater through a copper rod. The laser sheet is applied from one side of the setup and the CCD camera is set to take pictures perpendicular to the laser sheet.

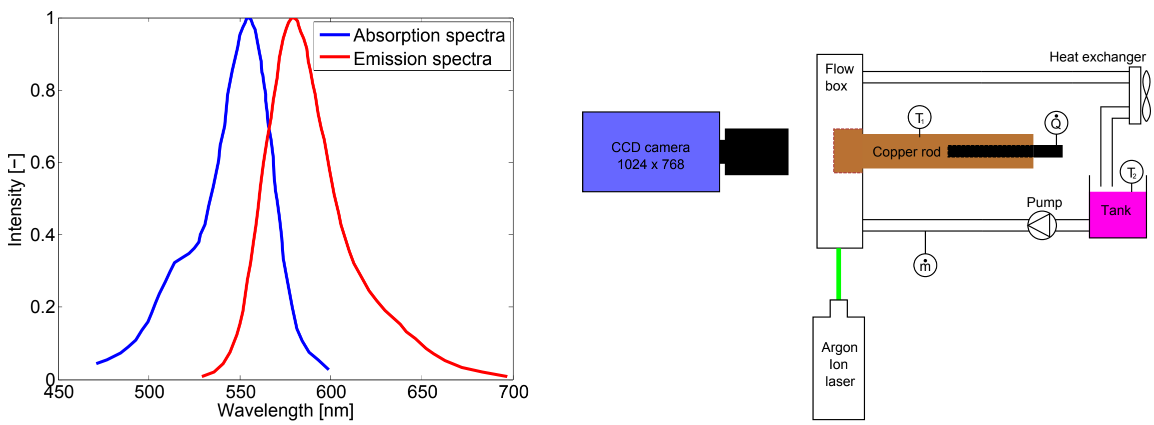

(a) (b)

Figure 2. *Figure (a) showing absorption and emission spectra of rhodamine B based on [12], and figure (b) showing schematic drawing of experimental setup.*

The correlation between the temperature and fluorescence intensity is evaluated to be linear [11]. To find this relationship the system is calibrated at steady state over a temperature range of 30-55 $^{\circ}C$. The CCD camera generates greyscale values corresponding to the different temperature values, hence making it possible to make the PLIF measurements.

The determination of the conventional Nusselt number is dependent on the Reynolds number, which is based on a flow measurement from a flow sensor, which is a FT-210 sensor from Gams with an accuracy of $\pm$ 3 %. The temperature in the copper rod is measured in order to approximate the fin temperature, as they are assumed equal, and the position is shown as T_1 in figure 2 (b). After the temperature experiments the calibration is again carried out with matching temperatures, in order to check for photobleach, described in the error analysis. At each measurement a total of 50 pictures is saved in TIFF-format with an exposure time of 1.7 s. The laser power is 1.2 W throughout the experiments.

To process the data a MATLAB algorithm is made for the present study. The 50 pictures from each measurement is averaged in order to reduce noise. A linear least squares fit is made between the greyscale values and the temperature. Each measured calibration temperature in each pixel is compared with the temperature calculated from the 1st order polynomial. If the deviation is more than 10 % the points are removed, and a new 1st order polynomial between the remaining points is made. The MATLAB image toolbox is used for faster data processing. The pixel size may be reduced for faster data processing, but it may also introduce an error in the resolution of the thermal boundary layer. Instead, only a section of the image is processed, speeding up calculation time.

The inlet area of the channels is distorted by reflections, and should not be considered. It is considered difficult to align a laser sheet accurately to a channel, because of laser spreading, and thus shadow effects occur. Hence, due to symmetry, only half of the channel width is considered, and may as well be enough for temperature gradient analysis. The fluid pixel intensities are averaged by the surrounding 5 pixels at the wall, and averaged with its surrounding 8 pixels elsewhere. This is in principle a low-pass filter, and reduces the pixel-to-pixel noise.

Figure 3 (a) shows a temperature plot of the averaged 50 calibration images at a temperature of 40.2 $^{\circ}C$ based on the entire first calibration series. Consequently, the temperatures should be 40.2 $^{\circ}C$ in the mini channels as each pixel is calibrated to fit this value. In figure 3 (a) the full sized image of the mini channels is shown from above, and the inlet of the water is from the right side of the image.

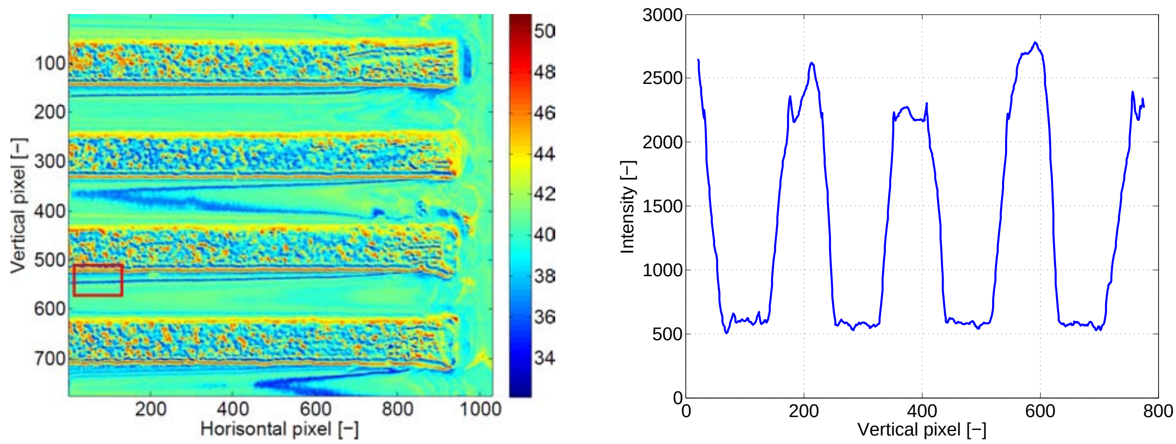

(a) (b)

Figure 3. *Figure (a) showing temperature contour in the investigation area at calibrated temperature of 40.2 $^{\circ}C$, and figure (b) showing intensity at a horisontal pixel value of 70.*

It can be seen in figure 3 (a) that the temperature is relatively uniform in the mini channels, while the intensity varies significantly inside the wall. The temperature of the wall is forced to fit the measured copper rod temperature. An important thing is to consider where the boundary between the water and the wall is located, as the experimentally measured h-values highly depend on this assumption. In figure 3 (a) it is shown that some areas of the mini channels should be disregarded due to poor quality. The selected area of interest is determined to be from 5 to 120 for the horisontal pixels.

To determine which vertical pixels to investigate a plot of the intensities along a constant pixel value of 70 is shown in figure 3 (b). In this figure the high spikes of intensity are in the channels, while the lower spikes are inside the wall. The curve from the vertical pixels with a value of 500 to 625 is seen to the have the smoothest curve. The vertical pixels from 509 to 578 are selected for the area of interest, as only half of the mini channel is considered. The selected area of interest is the red square in figure 3 (a). This area is a small portion of the whole image, which is mainly because of less calculation time, but also because of unwanted disturbances in other areas. However, in the area of interest there is optical disturbances, represented by a line of lower temperature.

4. Results

Temperature results are shown in figure 4 (a) and (b). The area of investigation is 115 horisontal pixels and 69 vertical pixels resulting in 611 μm x 366 μm, showing half of the channel width. It is assumed that the temperature profile of the channel in the region of interest is symmetric along the center of the channel. Figure 4 (a) shows the temperature of the wall and fluid. The wall is set to a constant temperature of 57.8 $°C$, which is the copper rod temperature. A temperature decrease occur perpendicular to the wall, as shown in figure 4 (b). The temperature decrease follows a parabolic tendency until 35-39 vertical pixels and is again parabolic after these points. The discontinuity is because of optical disturbances, which result in a line of lower temperature throughout the image in figure 4 (a).

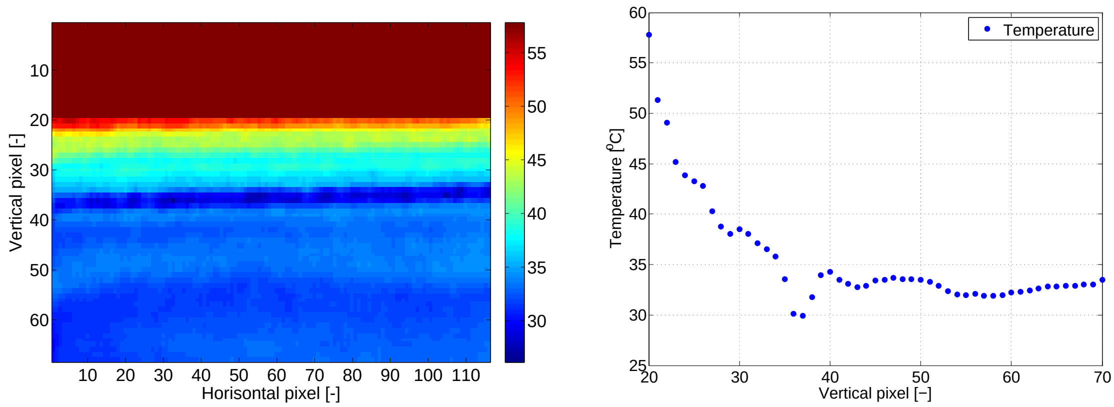

(a) (b)

Figure 4. *Figure (a) showing temperature contour in the selected area of interest, and figure (b) showing the vertical temperature profile at a horisontal pixel value of 70.*

Determination of the convective heat transfer coefficient, and hence the Nusselt number is carried out by evaluating the temperature gradient close to the wall using equation (1). Due to the no-slip condition, the fluid particle adjacent to the wall must be the same as the wall temperature. The PLIF experiment gives no information about the wall temperature, but the temperature is measured 25 mm from the top of the fin, and from thermal resistance theory the fin temperature must be less than the measured temperature. Due to uncertainties of the thermal resistance analysis, the two perpendicular pixels adjacent to the wall is used for estimation of the temperature gradient. The pixel length is estimated to be 5.31 μm. The h-values calculated from the PLIF experiment is shown in figure 5. The mean h-value is 9,299 W/m^2K equivalent to a Nusselt number of 13.89. The calculated measured h-values are validated by the Stephan and Preusser Nusselt number approximation in the same region of interest, shown in figure 5. The mean conventional based h-value is 9,335 W/m^2K equivalent to a Nusselt number of 13.95.

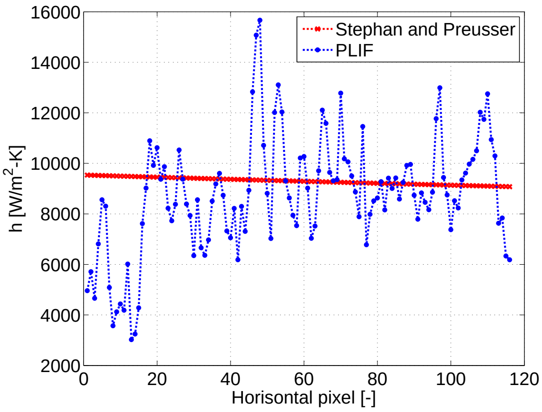

Figure 5. *Comparison of convective heat transfer coefficient based on conventional correlations and PLIF.*

5. Error Analysis

Errors and uncertainties encountered using PLIF are described by Coolen et al. [9] and Golnabi [13]. The main uncertainty is the calibration. The mapping of intensity to temperature is highly dependent on the curve fit from the calibration. It is important to reach steady state conditions, as a uniform temperature is needed. The temperature deviation in the tank water (T_2 in figure 2 (b)) is found sufficiently small, hence steady state is assumed.

An important factor influencing the emitted intensity is photobleaching of the dye. Photobleaching covers degradation of the dye as it is exposed to high power laser light, and results in a lower temperature due to less quantum yield [9], following equation (4).

A calibration between the temperature and the intensity is made before and after the experiments. The relative difference between the averaged calibration image for each of the calibration temperatures varies between 10.4 and 17.0 % for the fluid zone. Because of this difference an average between the two calibration sets is used for the making the 1st order polynomial fit between the temperatures and the intensity. A reason for the size of the relative difference could be that the temperature varied with ± 0.1 $°C$ during the experiment making the calibration temperature diverge slighty from each other, but also that rhodamine B could be deposited in the setup during the experiment, or that photobleaching occurs. A method to avoid photobleaching could be to implement a mechanical shutter in front of the laser, as the time the dye is exposed to the laser between the experiments then could be reduced. Another method is to use a larger volume of water and dye, which also reduces the laser exposure time pr. rhodamine B molecule. The relative difference between the first and second calibration measurement at a temperature of 30.2 $°C$ for the selected area of interest is shown in figure 6, where it can be seen that the relative difference is largest in the range of 0-20 vertical pixels, which is the wall. In the vicinity of the vertical pixel 36 the relative difference also increases due to optical disturbances, shown in figure 4 (a). For the rest of the selected area of investigation the relative difference seems to be more constant. The overall relative difference between these two calibration images is 16.2 % for the fluid zone.

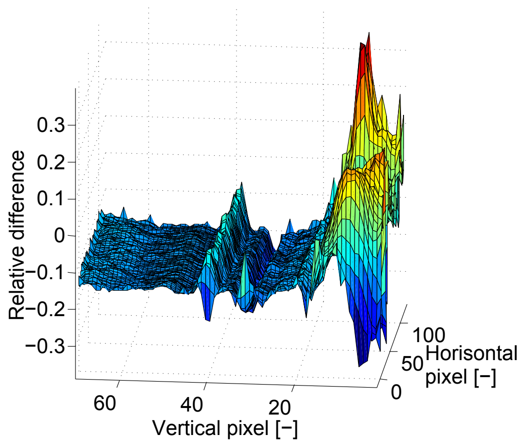

Figure 6. *Relative difference between first and second set of calibration images at a temperature of 30.2 °C.*

In figure 7 (a) a histogram of pixel (25,70) in figure 4 (a) is shown. The normal distribution of this histogram is also shown, and the sample mean is 1724. The standard deviation of 50 values in this pixel is found to be 74.3 which supports the choice of averaging over 50 pictures. With a 95 % confidence interval the deviation from the mean is calculated to be ± 20.6, or 1.2 %. In figure 7 (b) the calibration points in pixel (25,70) is shown with a linear fit resulting in a relative deviation of maximum 2 %. The assumption of a linear fit between intensity and temperature where tested at several pixels, and in the present work it is seen to match in the given temperature ranges.

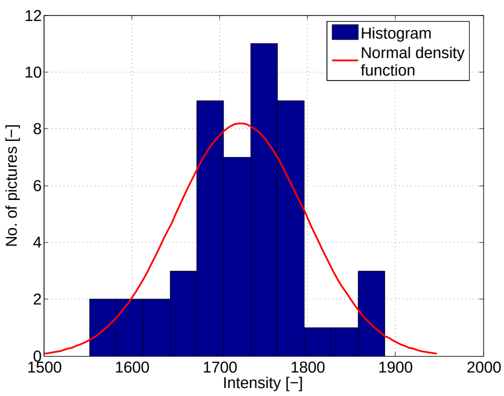

(a)

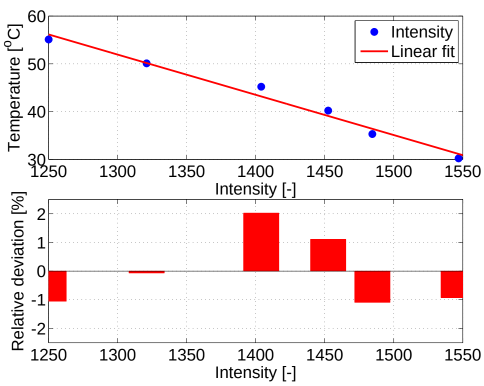

(b)

Figure 7. *Figure (a) showing histogram of pixel intensity for the 50 pictures in the temperature measurement with the histogram's normal distribution, and figure (b) showing calibration fit and accuracy.*

A source of error when using one-color PLIF is shadowgraph, described by Coolen et al. [9]. Shadowgraph occurs in areas of high temperature gradient due to local density variation causing a difference in the refractive index. Shadowgraph is significant when the temperature gradient in the direction of the laser light is more than 1 $°C/mm$. It is not seen to be the case in the present study, due to a temperature difference in and out of the channel of approximately 0.05 $°C/mm$, which is in the direction of the laser light. Also, the focus point of the CCD camera can induce errors, as it is hard to adjust this due to small length scales.

One of the main assumptions in the present paper is the determination of the wall boundary, as it may fall within a fraction of a pixel. If the wall boundary is misplaced it will introduce an error in the calculation of the convective heat transfer coefficient.

6. Conclusion

Heat transfer in mini channels with a hydraulic diameter of 889 μm is investigated experimentally using PLIF. With a Reynolds number of 260 the experimentally evaluated h-value is compared to a conventional correlation from Stephan and Preusser [6]. The applicability of PLIF is compared to the conventional correlation, and no significant difference is seen. The average resulting h-value for the investigated area is shown to be 9,299 W/m^2K for the experiment and 9,335 W/m^2K for the conventional correlation. The resolution of the temperature gradient is thus concluded to be sufficient, as in the present paper it is found advantageous not to downscale the picture resolution. However, a local heat transfer coefficient is not resolved precisely due to fluctuations. Besides this, the applicability of PLIF over the whole geometry is not found satisfactory, as optical disturbances are found. The laser needs to be aligned properly in order to avoid shadows, as this have a great importance on the accuracy of the experiment. It is found important to accurately determine the wall position in the image, as the two pixels adjacent to the wall is used to calculate the h-value.

References

[1] Gao P, Person S L and Favre-Marinet M 2002 *Int. J. of Thermal Sciences* **41** 1017–1027

[2] Adams T M and Abdel-Khalik S I 1998 *Int. J. Heat Mass Transfer* **41** 851–857

[3] Rahman M M 2000 *Int. Comm. Heat Mass Transfer* **27** 495–506

[4] Qu W and Mudawar I 2002 *Int. J. Heat Mass Transfer* **45** 2549–2565

[5] Cengel Y A 2006 *Heat and Mass Transfer - A Practical Approach* 3rd ed (McGraw Hill)

[6] Stephan K and Preusser P 1979 *Chem. Ing. Tech.* **51** 37

[7] Shah R K and London A L 1978 *Advances in Heat Transfer - Laminar Flow Forced Convection in Ducts* (Academic Press)

[8] Dantec 2001 Flowmanager add-on: Plif-module Installation and Users guide publication no.: 9040U3651

[9] Coolen M C J, Kieft R N, Rindt C C M and van Steenhoven A A 1999 *Experiments in Fluids* **27** 420–426

[10] Liu T and Sullivan J 2005 *Pressure and Temperature Sensitive Paints* 1st ed (Springer)

[11] Sakakibara J, Hishida K and Maeda M 1993 *Experiments in Fluids* **16** 82–96

[12] Terpetschnig E, Povrozin Y and Eichorst J 2012 Polarization standards ISS, Inc http://www.iss.com

[13] Golnabi H 2006 *Optics & Laser Technology* **38** 152–161

Theory of Planar Laser Induced Fluorescence

F

This chapter describes in details the theory of PLIF along with the MATLAB data processing.

F.1 Principles of PLIF

Planar laser induced fluorescence (PLIF) is a technique pioneered in the late 1970s by Long et al. [1978] and is still developing. PLIF is a non-intrusive measurement technique, meaning that the flow is not interrupted by measurement apparatus. The basic technique is to use a temperature sensitive fluorescence dye and excite it by laser light. It is used to measure either temperature or concentration in a flow field if one of the two parameters is held constant [Hanson et al., 1990]. In the following the focus is on temperature measurement and thus the dye concentration is held constant. The fluorescence is a process of radiation emitted by a molecule or atom as it spontaneously decays from a high electron energy level to a lower. The higher energy level is induced by a laser exciting the electron of a molecule or atom. The fluorescence occur at a longer wave length than the laser wave length due to energy loss in the excited state [Hanson et al., 1990]. The fluorescence intensity may be described by the following equation [Berlman, 1971]:

$$I = I_0 \cdot A \cdot \phi \cdot \varepsilon \cdot C \cdot \frac{\lambda_e}{\lambda_f} \tag{F.1}$$

where I_0 is the laser intensity, A is the fraction of the available light collected, ϕ is the quantum yield, ε is the molar absorptivity, C is the concentration of the fluorescent dye. The wave length ratio λ_e/λ_f accounts for the energy loss in the excited state. The temperature sensitivity of the dye turns out to influence the quantum yield, which results in a temperature dependent fluorescent intensity. This is due to temperature quenching effects of the dye, which results in a decreasing quantum yield for an increasing temperature [Coolen et al., 1999].

The fluorescent dye could for instance be illuminated by an Argon Ion laser with a wave length of 532 *nm*, which is in the green light spectra. Rhodamine B is then suitable as the fluorescent dye, which is shown in figure F.1 as the peak intensity for the emission spectra of Rhodamine B is in the vicinity of 600 *nm*, which is the orange light spectra. Using an appropriate filter, only the emitted fluorescence is captured by a charged coupled device (CCD) camera. The 2D image is used as an array of intensities where the pixels in the image is used as collection points.

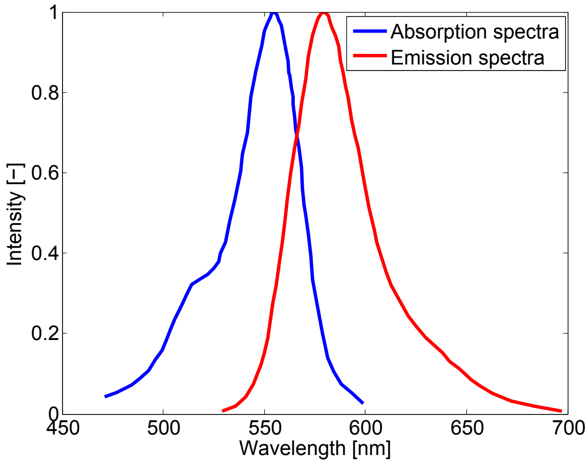

Figure F.1: *Absorption and emission spectra of rhodamine B [Terpetschnig et al., 2012].*

F.2 Data Treatment

In figure F.2 a flowchart of the calculations carried out in MATLAB is shown. The algorithm starts by loading in the different images, both the calibration images and the experiment picture, and these images are then send through a filter after an average of 50 images has been taken. The low pass filter smooths out the data by either taking the average of the surrounding five pixels if it is at a wall boundary, or an average of the surrounding eight pixels if the location is in the channel. If the location is inside the wall the intensity is set to zero.

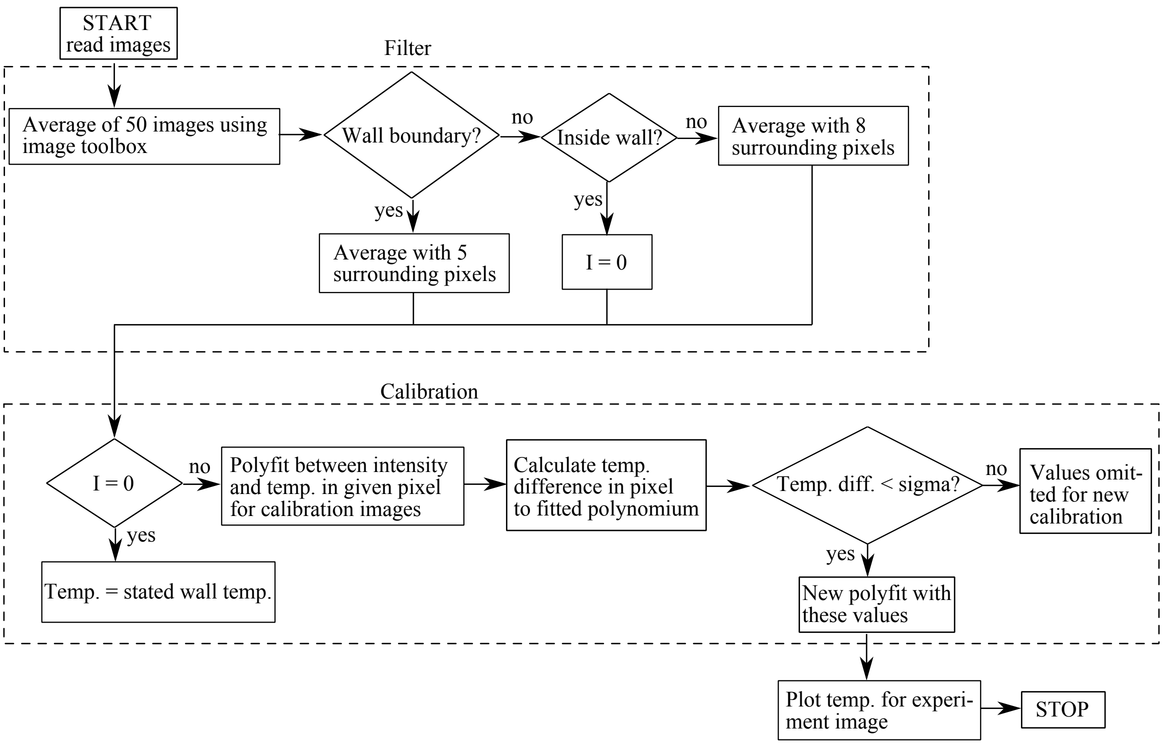

Figure F.2: *Flowchart over data treatment of PLIF experiment.*

The next main part of the algorithm is the calibration phase. The first thing implemented is that the wall temperature is set to a given value if the intensity is zero as this indicates the location is inside a wall. By doing this, a clear indication of where the wall is, is shown in the final result. The correlation between the temperature and fluorescence intensity is assumed to be linear in a certain range, hence a least squares fit is made in each pixel between the temperature from each calibration image and the intensity which is represented by a greyscale value. After making the polynomium of the calibration data the temperature difference between the fitted linear polynomium and the temperature in the pixel in each image is compared. If the deviation is more than 10 % the points are removed from the next fitted polynomium made. The last phase is to make the temperature plot of the filtered experiment image.

F.3 Validation of Data Treatment

It is important to validate how accurate the different filters are in the algorithm for the data treatment. To validate this a fictive calibration data set is made in MATLAB by generating 8-bit TIFF images which are converted to 16-bit images. Each of the generated greyscale calibration images is set to correspond to a given temperature as seen in table F.1.

Intensity	**Temperature** [$^\circ C$]
3277	10
2621	15
1966	20
1311	25
655	30

Table F.1: *Artificial greyscale values and their corresponding temperatures used for validation.*

In addition to this a test TIFF picture is made with rectangular varying greyscale values in a matrix, hence the transition between the different temperature zones is studied. In figure F.3 the greyscale image before the data treatment is seen on the left, and on the right side the temperature plot of the same image is seen after the data treatment.

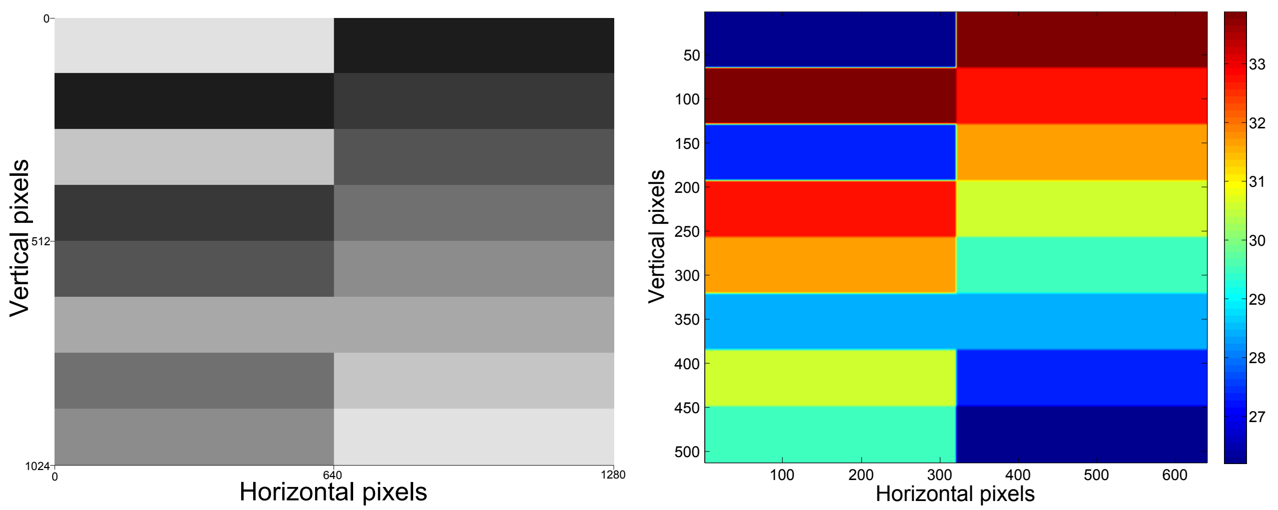

(a) *Greyscale validation image before data treatment.*

(b) *Image after data treatment. Temperature contour is shown on the right.*

Figure F.3: *Validation of data treatment algorithm.*

Figure F.3 shows that a low intensity, shown by the black rectangles yields a high temperature, while the higher greyscale values shown in the white rectangles yields a lower temperature. The pixel size of the image is reduced by a factor of four to speed up calculation time. The validation shows that the correct values are obtained if the values are compared to the calibration data, and if the assumption with linear relationship is true. However, the transition between the different temperature zones needs to be studied further, a close up in the transition zone is therefore shown in figure F.4.

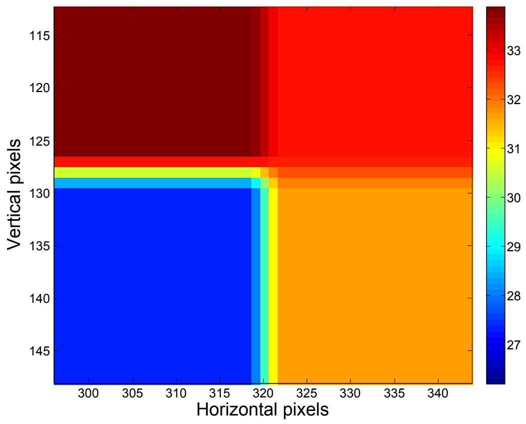

Figure F.4: *Close up of transition zone between different temperature zones.*

If these transition zones are compared to the greyscale image it clearly shows the effect of taking an average over the surrounding pixels. The pixels in the transition between pixels with different values will be an average, however, it is still worthwhile having this filter as it helps smoothing out errors in the pixels, e.g. air bubbles and reflections. The effect of the filter is further studied in figure F.5. A spiral matrix in MATLAB adds a value of 1 in a pattern from the inside and out. A very smooth transition of the greyscale values is seen on the left side in figure F.5, while a less smooth transition is seen on the right side of this figure.

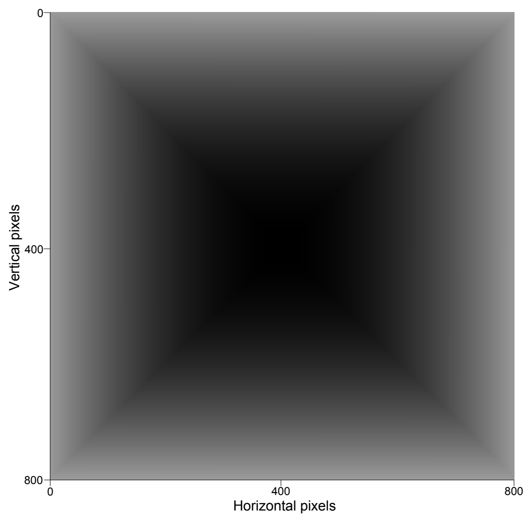

(a) *Greyscale values of a spiral matrix.*

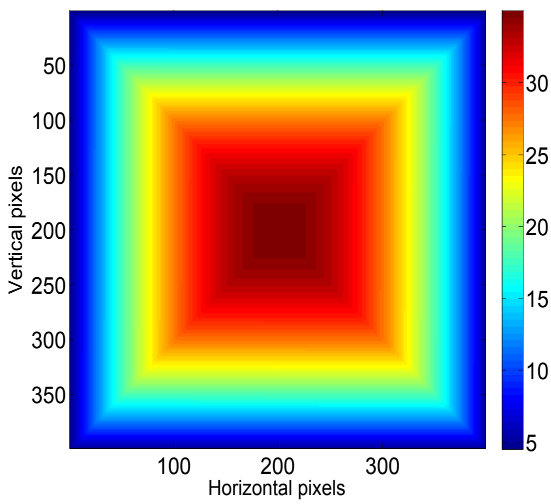

(b) *Calibrated image.*

Figure F.5: *Validation of algorithm on spiral image.*

The last part of the calibration phase is to look at the polynomium fit between the calibration temperature and intensity. The first polynomium fit made is between all the calibration data. Based on this polynomium, a second polynomium is made between all the points which diverges less then a certain percentage deviation, e.g. 5 % in this case. This is seen in figure F.6, where two data points are removed as they diverge to much.

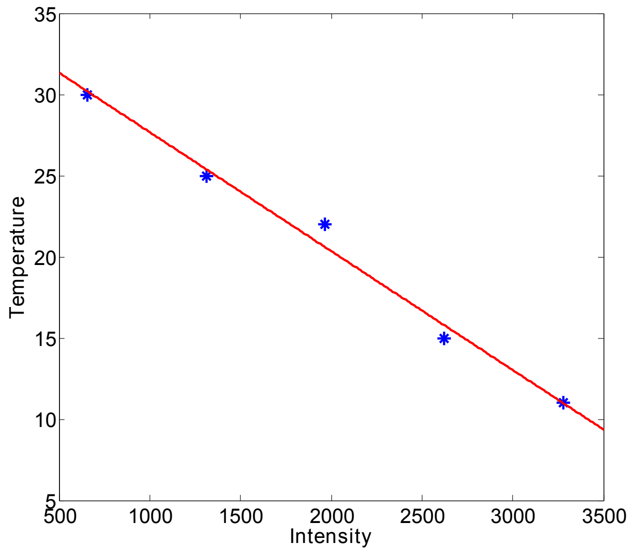

(a) *Polynomium before temperature check with five points.* (b) *Polynomium after temperature check with three points.*

Figure F.6: *Improved calculation after temperature check*

This adjustment of the polynomium depends on the first set of calibration data. If a lot of these calibration data points are wrong, the chances are that the second polynomium is also wrong. A demand when doing this adjustment, is that the calibration data must be linear, otherwise to many data points will be removed and a wrong polynomium fit is made. An important thing when making the calibration data set is to make enough calibration points to minimize the number of "outliers", as this improves the accuracy, and the advantage of having the adjustment of the polynomium fit is larger. If the calibration between intensity and temperatures in a given pixel is influenced a lot by either air bubbles or shadow between the different calibrations it can have a bad effect on the fitted polynomium. It is therefore very important to have images of a high quality when making PLIF experiments.

F.4 Limitations of PLIF

PLIF has limitations and sources of error. The following describes the most important ones:

- Calibration
- Photobleaching
- Laser power stability
- Self-absorption
- Shadowgraph effects

Coolen et al. [1999] describes the error encounted in their work. The major error is the calibration function error, when the intensities are converted to temperatures. An important factor influencing the intensity is photobleaching. This is caused by the degradation of the dye as it is exposed to high power laser light. This may be avoided by limiting the time the laser is used, or to have a large amount of coolant.

The laser output may vary with time, and as the fluorescence intensity is highly dependent on the laser intensity, this provokes an error proportional to the instability of the laser.

Self-absorption is a term that involves absorption of the re-emitted fluorescence from the dye. The self-absorption is temperature dependent, as it is a function of the quantum yield.

Shadowgraph effects is a local variation of the intensity. This is due to a variation of the refractive index inside the fluid. This variation is caused by a variation in density, and because the density is temperature dependent, the refractive index is temperature dependent. Coolen et al. [1999] concludes that the shadowgraph effects are very sensitive to temperature gradients. Hence the fluorescence intensity is not only temperature dependent, but also temperature gradient dependent. Coolen et al. [1999] states, that the most important restriction of PLIF is the shadowgraph effects. As a rule of thumb the temperature error will remain below 1 $^{\circ}C$ if the temperature gradient is kept under 1 $^{\circ}C/mm$. Coolen et al. [1999] proposes the use of a correction equation in order to handle the shadowgraph effects, but concludes that it is not sufficient, and shadowgraph effects still occur.

Lavieille et al. [2001] solves the shadowgraph problem by using a so-called two-color/single-dye technique. Instead of using one camera and one spectral filter, Lavieille et al. [2001] use two cameras and two spectral bands. This technique removes the dependency on dye concentration and laser intensity, and hence also shadowgraph effects. The first spectral filter has a spectral width of 525-535 *nm* and the second spectral band is >590 *nm*.